Personalised Signal Processing for Cortical and Cardiac Applications

by

Simanto Saha

B.Sc. (Electrical and Electronic Engineering),
United International University, Bangladesh, 2014

Thesis submitted for the degree of

Master of Philosophy

in

Electrical and Electronic Engineering
University of Adelaide

2020

Supervisors:

Associate Professor Mathias Baumert, School of Electrical and Electronic Engineering

Professor Prashanthan Sanders, Adelaide Medical School

Associate Professor Dominik Linz, Adelaide Medical School

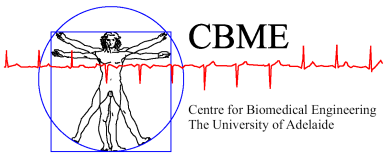

To my Mum, Dad, Satyam, Udita and Ullash.

Contents

Abstract

Biomedical signals reflect alterations in human physiological parameters in both healthy and pathological conditions. Their inherent variability over time and across individuals reduces the reproducibility of results and utility of biomedical signals. Personalisation of signal processing schemes by including parameters associated with the sources of inter-session and inter-subject variability can promote the usability of biomedical signals for larger cohorts. This thesis explores strategies for personalising signal processing techniques for the assessment of cortical and cardiac electrophysiological phenomena.

A sensorimotor rhythm-based brain-computer interface (BCI) exploits changes in electroencephalogram (EEG) during motor imagery tasks and can establish a direct communication link between the brain and a computer, which may augment motor performance. Dealing with the variability inherent in EEG signals is not trivial and yet to be understood comprehensively to deliver BCI technology for practical use. A wavelet-based signal processing method has been applied to model inter-subject associative source activations, leading to a more generalised BCI design.

Intracardiac electrograms (EGM) are important for mapping electrical activation across the heart. Multiple variables, including bipolar vector orientation relative to the wave propagation vector, inter-electrode spacing, impact EGM recording. In this thesis, intracardiac EGM recorded with a customised array of electrodes were analysed to assess the impact of bipolar vector orientation and inter-electrode spacing on atrial fibrillation mapping. A novel spatial filtering method has been proposed to reduce the measurement uncertainty due to bipolar vector orientation. Besides, an independent component analysis-based filtering has been proposed as a potential preprocessing method for eliminating ventricular far-field artefact.

Statement of Originality

I certify that this work contains no material which has been accepted for the award of any other degree or diploma in my name, in any university or other tertiary institution and, to the best of my knowledge and belief, contains no material previously published or written by another person, except where due reference has been made in the text. In addition, I certify that no part of this work will, in the future, be used in a submission in my name, for any other degree or diploma in any university or other tertiary institution without the prior approval of the University of Adelaide and where applicable, any partner institution responsible for the joint-award of this degree.

I give permission for the digital version of my thesis to be made available on the web, via the University's digital research repository, the Library Search and also through web search engines, unless permission has been granted by the University to restrict access for a period of time.

Simanto Saha

Acknowledgments

I would like to convey my deepest gratitude to my principal supervisor **Associate Professor Mathias Baumert** for his generous support and guidance throughout my candidature. First, I am indebted to him for believing in my research aptitude, with an offer of a graduate position in his group. His continuous guidance helped me a lot to cope up with a multidisciplinary project (in collaboration with the Adelaide Medical School). Without the influence of his knowledge on cardiac signal processing, it would be impossible for me to understand the non-trivial clinical problem of atrial fibrillation and the issues related to intracardiac bipolar electrogram measurement. Specifically, his significant contribution had made it possible to define a plausible strategy to quantify the impact of bipolar vector orientation on atrial fibrillation mapping.

I am also very thankful to my co-supervisors **Professor Prashanthan Sanders** and **Associate Professor Dominik Linz** for providing me access to Royal Adelaide Hospital and South Australian Health and Medical Research Institute (SAHMRI) facilities. They helped me to get the raw dataset, which was required to successfully complete the analysis. Discussions were very insightful to interpret the clinical aspect of the proposed methods related to atrial fibrillation mapping. I would also like to thank Rayed Kutieleh and the Abbott Medical team for their assistance in raw data extraction. I am also grateful to the members of the Centre for Heart Rhythm Disorders for welcoming me.

I would like to thank my colleagues and friends Simon and Filip, for keeping me always psychologically up until the completion of my degree. We started our graduate studies at around the same time, and they had to tolerate all my jibber-jabber. Simon helped me with all mysterious but simple software-related issues.

Finally, I am and will always indebted to my Mum and Dad for their unconditional love and mental support to continue my higher studies. Also, I am very grateful to my elder brother (Dadabhai) and sister (Didibhai) for being physically present with my parents during their needs and taking care of their health so that I can concentrate on my research. A special thanks goes to my brother-in-law (Dadababu) for everything he did for me.

Honours and Awards

Scholarships

- **Leo J Mahar Scholarship** by the University of Adelaide, 2018 - 2020.
- **Full Fee Scholarship** by the University of Adelaide, 2018 - 2020.
- **25% Tuition Fee Waiver** by United International University, 2010 - 2014.
- **Merit Scholarships** by United International University, 2010 - 2014.

Travel Grants

- **Research Travel Scholarship** by the University of Adelaide, 2019.
- **IEEE EMBS Student Travel Award** by IEEE, 2019.
- **Travel Allowance** by the School of EEE (the University of Adelaide), 2019.

Publications and Talks

Journal Articles

- **Saha, S.** and M. Baumert, "Intra- and inter-subject variability in EEG-based sensorimotor brain computer interface: a review", Frontiers in Computational Neuroscience, vol. 13, 2020.
- **Saha, S.**, M.S. Hossain, K. Ahmed, R. Mostafa, L. Hadjileontiadis, A. Khandoker and M. Baumert, "Wavelet entropy-based inter-subject associative cortical source localization for sensorimotor BCI", Frontiers in Neuroinformatics, vol. 13, 2019.
- **Saha, S.**, K. Ahmed, R. Mostafa, L. Hadjileontiadis and A. Khandoker, "Evidence of variabilities in EEG dynamics during motor imagery-based multiclass brain–computer interface," IEEE Transactions on Neural Systems and Rehabilitation Engineering, vol. 26, no. 2, pp. 371-382, Feb. 2018.
- **Saha, S.**, K. Ahmed, R. Mostafa, A. Khandoker and L. Hadjileontiadis, "Enhanced inter-subject brain computer interface with associative sensorimotor oscillations", Healthcare Technology Letters, vol. 4, no. 1, pp. 39-43, 2017.

Conference Papers

- **Saha, S.**, D. Linz, P. Sanders and M. Baumert, "Beamforming-inspired spatial filtering technique for intracardiac electrograms," 2019 41st Annual International Conference of the IEEE Engineering in Medicine and Biology Society (EMBC), Berlin, Germany, 2019, pp. 4254-4257.
- **Saha, S.**, S. Hartmann, D. Linz, P. Sanders and M. Baumert, "A ventricular far-field artefact filtering technique for atrial electrograms," 2019 Computing in Cardiology (CinC), Singapore, Singapore, 2019, pp. 1-4.
- **Saha, S.**, K. Ahmed and R. Mostafa, "Wavelet coherence based channel selection for classifying single trial motor imagery," 2016 9th International Conference on Electrical and Computer Engineering (ICECE), Dhaka, Bangladesh, 2016, pp. 467-470.

- **Saha, S.**, K. Ahmed and R. Mostafa, "Unifying sensorimotor dynamics in multi-class brain computer interface," 2016 5th International Conference on Informatics, Electronics and Vision (ICIEV), Dhaka, 2016, pp. 530-535.
- **Saha, S.** and K. Ahmed, "Efficient event related oscillatory pattern classification for EEG based BCI utilizing spatial brain dynamics," 8th International Conference on Electrical and Computer Engineering, Dhaka, 2014, pp. 707-710.

Talks

- Oral presentation at the 41st Annual International Conference of the IEEE Engineering in Medicine and Biology Society (EMBC), Berlin, Germany, 2019.
- Oral presentation at the 9th International Conference on Electrical and Computer Engineering (ICECE), Dhaka, Bangladesh, 2016.
- Oral presentation at the 8th International Conference on Electrical and Computer Engineering (ICECE), Dhaka, Bangladesh, 2014.

List of Figures

List of Tables

Chapter 1

Introduction

BIOMEDICAL engineering is the field of study that integrates knowledge of engineering, science and biology for healthcare purposes. It covers a broad spectrum of applications including the development of artificial organs, robot-assisted surgical procedures, artificial prosthetics, targeted drug delivery and diagnostic tools. As a result, collaboration amongst diverse disciplines such as medicine, science and engineering is essential to successfully translate a potential application for practical use. Biomedical signal processing is a subdiscipline of biomedical engineering that utilises signal processing algorithms to assess physiological changes over time.

Biomedical signals reflect fluctuations of human physiological parameters in healthy and pathological conditions. Recent advances in both invasive and noninvasive signal acquisition techniques have inspired the inclusion of diverse signal processing algorithms in the design of rehabilitative and therapeutic interventions (Baumert *et al.* 2016a). Applications include investigation of sensorimotor cortical dynamics (Saha *et al.* 2017b, Saha *et al.* 2019a) and disturbances in cardiac conduction pathway during atrial fibrillation (Baumert *et al.* 2016b).

One of the key challenges in biomedical signal processing is the inherent inter-session and inter-subject variability in recorded signals. The time-variant human physiological parameters as well as experimental setup-related factors induce nonstationarity in biomedical signals and often weaken the reproducibility of results (Anter and Josephson 2016, Saha *et al.* 2017b). Personalisation of a signal processing method by including parameters associated with the sources of inter-session and inter-subject variability can promote the usability of a proposed method for larger cohorts. This thesis explores the personalised application of signal processing techniques for the assessment of cortical and cardiac electro-physiological phenomena.

1.1 Sensorimotor Cortical Signal Processing

Brain computer interfaces (BCI) for the rehabilitation of motor impairments exploit sensorimotor rhythm (SMR)-related cortical activities in electroencephalogram (EEG) (Dobkin 2007). The cognitive and neurological processes underpinning the SMR often vary over time and across subjects and affect EEG-based BCI performance (Blankertz *et al.* 2009, Vidaurre and Blankertz 2010, Hammer *et al.* 2012, Jeunet *et al.* 2015, Sannelli *et al.* 2019, Ahn and Jun 2015, Reichert *et al.* 2015, Zhang *et al.* 2015a, Vasilyev *et al.* 2017). Such inherent variability causes covariate shift in data distributions that make the transferability of model parameters amongst sessions/subjects onerous. A covariate shift occurs when distributions of training and test datasets differ significantly although their conditional distributions may remain unchanged (Krusienski *et al.* 2011). Transfer learning includes signal processing and machine learning-based methods to compensate for inter-subject and inter-session variability manifested in EEG-derived feature distributions as a covariate shift for BCI (Jayaram *et al.* 2016). Chapter 2 reviews the cognitive and neurological aspects of sensorimotor cortical dynamics that affect BCI performance. Chapter 3 introduces a time-frequency analysis method for the assessment of inter-subject SMR dynamics.

1.2 Cardiac Signal Processing for AF Ablation

Intracardiac catheter ablation (CA) is a widely used clinical procedure to terminate atrial fibrillation (AF)-related electrical sources and to restore sinus rhythm. Electrograms (EGM) are recorded using catheter-based electrodes before CA for the identification of ablation targets (Baumert *et al.* 2016b). Usually, bipolar EGM are constructed from unipolar EGM to quantify the arrythmogenic substrates.

Multiple variables, including bipolar vector orientation relative to the wave propagation vector, inter-electrode spacing, electrode size and tissue contact, impact bipolar EGM and EGM-derived measures (Anter and Josephson 2016). In addition, preprocessing, i.e., filtering of undesired signal contents plays a critical role in arrythmogenic substrate characterisation. Chapter 4 demonstrates the impact of bipolar vector orientation and inter-electrode spacing on EGM.

Once EGM are already recorded using a catheter with certain specifications, bipolar vector orientation could be integrated into a mapping tool when specially-designed

multi-electrode catheters are available. Chapter 5 proposes a novel spatial filtering technique to reduce measurement variability due to random bipolar vector orientation. Also, preprocessing (filtering) techniques are crucial for AF-related target identification. For example, ventricular far-field artefact contaminates local atrial EGM. Chapter 6 delineates a ventricular artefact reduction (VAR) technique based on wavelet transform and independent component analysis (ICA).

Chapter 2

Sensorimotor Brain Computer Interface: A Literature Review

BRAIN computer interfaces (BCI) for the rehabilitation of motor impairments exploit sensorimotor rhythms (SMR) in the electroencephalogram (EEG). However, the neurophysiological processes underpinning the SMR often vary over time and across subjects. Inherent intra- and inter-subject variability causes covariate shift in data distributions that impede the transferability of model parameters amongst sessions/subjects. Transfer learning includes machine learning-based methods to compensate for inter-subject and inter-session (intra-subject) variability manifested in EEG-derived feature distributions as a covariate shift for BCI. Recent studies have explored psychological and neurophysiological predictors as well as inter-subject associativity assessment, which may augment transfer learning in EEG-based BCI. This chapter highlights the importance of measuring inter-session/subject performance predictors for generalised BCI frameworks for both normal and motor-impaired people, reducing the necessity for tedious and annoying calibration sessions and BCI training.

Associated Publication: *Saha, S.* and M. Baumert, "Intra- and inter-subject variability in EEG-based sensorimotor brain computer interface: a review", Frontiers in Computational Neuroscience, vol. 13, 2020.

2.1 Introduction

Brain computer interfaces (BCI) exploiting sensorimotor rhythms (SMR) have shown promise for both the improvement of motor performance in normal subjects and the rehabilitation of motor function in patients (Wang and Jung 2011, Dobkin 2007). The SMR can be elicited by motor imagery (MI) that shares common neurophysiological mechanisms with overt motor execution (ME), the former being more convenient for BCI users who cannot perform an overt ME task due to some degree of motor disability (Jeannerod 1995, Lotze and Halsband 2006, Vyas *et al.* 2018, Zich *et al.* 2015). ME supplements the MI-based motor learning process for people with intact cognitive functions (Allami *et al.* 2008, Ruffino *et al.* 2017).

Since the motor learning processes differ across individuals (Herzfeld and Shadmehr 2014, Wu *et al.* 2014), significant inter-subject variability in motor behaviour is anticipated that manifests in the task-specific electrical activities in the cortico-subcortical networks (Seghier and Price 2018). Consequently, the cortical activity observed in electroencephalogram (EEG) varies across subjects during MI, impeding its utility for BCI applications (Saha *et al.* 2017b). A study has suggested that time-variant brain functions cause unreliable EEG signatures with poor reproducibility even within a particular subject (Meyer *et al.* 2013). Such inter-session, intra-subject variability together with even larger inter-subject variability confounds BCI using SMR. This chapter discusses how inter-session and inter-subject performance predictors could potentially augment transfer learning to improve SMR-based BCI performance while reducing calibration efforts significantly.

2.2 Sensorimotor Dynamics and BCI

2.2.1 Motor learning process and brain function

Motor variability due to variability in human kinematic parameters, e.g., force field adaptation, speed and trajectory, and motivational factors such as level of user engagement, arousal and feelings of competence, necessary for performing a motor task is an integral part of the motor learning process (Duarte and Reinkensmeyer 2015,

Úbeda *et al.* 2015, Edelman *et al.* 2019, Faller *et al.* 2019). Such variability does not necessarily represent noise contents only, but may potentially be a manifestation of motor and perceptual learning processes. Motor variability may augment reinforcement-based motor learning (Herzfeld and Shadmehr 2014, Wu *et al.* 2014, Singh *et al.* 2016). Individuals with higher motor variability may learn a skill faster than individuals with lower motor variability (Wu *et al.* 2014, Singh *et al.* 2016). The EEG patterns associated with motor variability could therefore partly explain intra-individual variability in SMR-based BCI (Úbeda *et al.* 2015, Bradberry *et al.* 2010, Ostry and Gribble 2016). Furthermore, structural and functional differences between subjects are associated with the motor learning process, which might explain the motor learning variability (Tomassini *et al.* 2011). On the other hand, motor variability could be leveraged to augment motor learning and rehabilitation (Singh *et al.* 2016, Krakauer 2006). A study has demonstrated that alterations in EEG signatures due to motor training are dependent on intra- and inter-subject variability (Jochumsen *et al.* 2017).

2.2.2 Motor imagery versus motor execution

Motor imagery is the kinesthetic anticipation of corresponding overt ME without producing an actual motor output. Jeannerod stated that MI is functionally equivalent to its ME counterpart (Jeannerod 1995). More specifically, MI is related to the preparation of ME and represents meaningful neurophysiological dynamics of human motor functions (Zich *et al.* 2015). Consequently, both MI and ME share common sensorimotor areas such as primary motor area (M1), supplementary motor area (SMA) and premotor cortex (PMC) (Jeannerod 1995, Lotze and Halsband 2006, Zich *et al.* 2015).

The neurophysiology underlying MI may differ in healthy people and patients with motor-impairing conditions (Lotze *et al.* 2001). MI-based BCI may augment the motor learning process in healthy subjects (Ruffino *et al.* 2017). In patients with impaired motor functions, MI is often the only viable option to drive rehabilitative BCI due to users' inability to perform overt ME (Jackson *et al.* 2001, Lotze and Halsband 2006). The individuality and severity of motor impairments impact the underlying neurophysiology, for example, post-stroke neurophysiology relies on the lesion locations (Niazi *et al.* 2013). Studies are essential to further delineate the roles of MI and ME in motor learning or relearning for both healthy and impaired subjects to refine the design of BCI for supplementing the motor learning process.

2.2.3 Neuroplasticity and BCI-driven motor rehabilitation

Rehabilitative BCI designs either attach neural prostheses to the impaired upper/lower limb or restimulate the damaged synaptic networks. In either case, the idea is to exploit and promote neural plasticity (Wang *et al.* 2010a, Dobkin 2007). The plastic characteristics of the brain are created by the time-variant behaviour of the synapses within complex neural networks, first illustrated by Donald O. Hebb in 1949 (Brown and Milner 2003). The motor learning process and associated variability promote plasticity in the sensorimotor networks and adjust both motor and perceptual skills (Ostry and Gribble 2016). This inherent plasticity is exploited by BCI systems to rehabilitate impaired motor functions (Dobkin 2007). Ruffino *et al.* demonstrated that MI-based mental training can contribute to corticospinal plasticity (Ruffino *et al.* 2017). This might lead to BCI-driven rehabilitation systems for stroke and spinal cord injury patients (Niazi *et al.* 2013, Müller-Putz *et al.* 2014). Recent studies showed that BCI skill acquisition and associated physiological changes may improve BCI performance in both patients and healthy users (Perdikis *et al.* 2018, Edelman *et al.* 2019). Complex or cognitively entertaining tasks that require greater user engagement or motivation can compensate for intra- and inter-subject variability, leading to enhanced BCI learning in adverse operating conditions (Perdikis *et al.* 2018, Edelman *et al.* 2019, Faller *et al.* 2019, Li *et al.* 2019).

BCI-driven prostheses can extend the degree of freedom of users with motor impairments. The success of BCI control and rehabilitation depends on the user's capacity to modulate the intact neural ensembles (Dobkin 2007). Substantial changes in neural substrates that were observed following closed-loop BCI-driven motor learning of prosthesis control provide evidence of neuroplasticity (Orsborn *et al.* 2014). In stroke patients, post-rehabilitation electromyographic recordings showed increased activity in the paretic finger following BCI-driven rehabilitation using an orthosis, which exhibits improvement in neuromuscular coherence for movement control (Ramos-Murguialday *et al.* 2013). Furthermore, BCI-driven proprioceptive feedback-based and functional electrical stimulation-based rehabilitation strategies could reinforce motor control (Darvishi *et al.* 2017, Zhao *et al.* 2016, Selfslagh *et al.* 2019).

The structural and functional changes in neural substrates induced by MI-based training with transcranial direct current stimulation or transcranial magnetic stimulation provide further evidence for the induction of neuroplasticity that is essential for motor recovery (Hong *et al.* 2017, Johnson *et al.* 2018). Because the induction of plasticity

by rehabilitation varies across subjects (Leamy *et al.* 2014, Vallence *et al.* 2015), subject-specific training sessions may be required. Since the neurophysiology associated with SMR dynamics varies between individuals, quantification of variability in healthy user groups could be a beneficial first step that may guide the interpretation of altered neurophysiology in diverse conditions of motor-impairment (Müller-Putz *et al.* 2014).

2.3 Brain Topography and BCI Performance Predictors

2.3.1 Intra- and inter-subject variability in brain topography

The functional relevance of brain topographical variability with the anatomical boundaries is still not fully understood; however, significant structure-function correspondences may be derived at the aggregate level (Honey *et al.* 2009, Honey *et al.* 2010). Smith *et al.* delineated structural differences, suggesting that the number of folds and thickness of the cortex could be associated with whole-brain functional networks (Smith *et al.* 2019). Furthermore, inter-subject variability in topography occurs due to subject-specific cognitive style and strategy to perform a task over time (Seghier and Price 2018), which could augment the underlying learning processes, e.g., motor and perceptual learning (Herzfeld and Shadmehr 2014, Wu *et al.* 2014, Baldassarre *et al.* 2012, Singh *et al.* 2016, Krakauer 2006).

Intra- and inter-subject variability can be explained by scale-dependent brain networks in spatial, temporal and topological domains (Betzel and Bassett 2017, Betzel *et al.* 2019). For example, diversity in spatial organisation of the brain networks can be investigated either at cellular or system level. The sources of intra- and inter-subject variability in brain dynamics may be identifiable using multi-scale analysis tools (Betzel *et al.* 2019) although the interpretation of brain connectivity networks at different scales may not be straightforward (Raichle 2009).

Integrating intrinsic brain activities (i.e., resting state activities) into BCI design could offer experimental and methodological advantages for scrutinising task-specific brain dynamics (Northoff *et al.* 2010). While it has been argued that the brain is primarily reflexive, responding according to external stimuli/environmental demand, the brain also performs many intrinsic functions including signal acquisition, maintenance, and interpretation (Raichle 2009, Raichle 2010). Supporting the critical role of intrinsic brain activity, it consumes 20% of the body's energy (Clarke 1999). Thus, understanding the

role of resting EEG might supplement BCI performance (Northoff *et al.* 2010, Suk *et al.* 2014, Morioka *et al.* 2015).

2.3.2 BCI performance predictors

Around 15-30% of users are inherently not able to produce task-specific signature robust enough to control a BCI (Blankertz *et al.* 2009, Vidaurre and Blankertz 2010). The underlying causes of this BCI illiteracy are not well-understood; however, diverse psychological and neurophysiological predictors appear to be associated with BCI performance (Blankertz *et al.* 2009, Vidaurre and Blankertz 2010, Hammer *et al.* 2012, Jeunet *et al.* 2015, Sannelli *et al.* 2019, Ahn and Jun 2015, Reichert *et al.* 2015, Zhang *et al.* 2015b, Acqualagna *et al.* 2016, Vasilyev *et al.* 2017, Jensen *et al.* 2011).

Cognitive and neurological factors including functions and anatomy along with emotional and mental processes give rise to intra- and inter-subject variability affecting the performance of SMR-based BCI (Smith *et al.* 2019, Seghier and Price 2018, Betzel and Bassett 2017, Betzel *et al.* 2019, Wens *et al.* 2014, Reichert *et al.* 2015, Zhang *et al.* 2015b, Acqualagna *et al.* 2016, Vasilyev *et al.* 2017). Time-variant cognitive factors such as fatigue, memory load, attention and reaction time modulate instantaneous brain activity, and can cause inconsistent SMR-based BCI performance (Fox *et al.* 2015, Hammer *et al.* 2012, Jeunet *et al.* 2015, Sannelli *et al.* 2019, Ahn and Jun 2015, Darvishi *et al.* 2018). Furthermore, users' characteristics such as lifestyle, gender, and age can influence BCI performance (Ahn and Jun 2015). Kasahara *et al.* illustrated that a neuroanatomical feature, i.e., gray matter volume is associated with SMR-based BCI performance (Kasahara *et al.* 2015).

The structural and functional differences may characterise dynamic baseline activities manifested in resting-state network (RSN) dynamics. RSNs represent large-scale spatiotemporal structures exhibiting intrinsic brain activities that are thought to be functionally relevant (Deco *et al.* 2011). Studies have shown intra- and inter-subject variability in sensorimotor RSN, which may have implications for BCI performance variability (Wens *et al.* 2014, Reichert *et al.* 2015, Zhang *et al.* 2015b, Acqualagna *et al.* 2016, Vasilyev *et al.* 2017, Jensen *et al.* 2011). It has been hypothesized that SMR-based BCI performance predictor is reliable for people who display strong resting EEG amplitudes (Sannelli *et al.* 2019, Suk *et al.* 2014, Blankertz *et al.* 2010). Table 2.1 shows a list of intra- and inter-subject BCI performance predictors.

Table 2.1. Intra- and inter-subject BCI performance predictors.

Study	Subject*	Task Type	Task Description	Predictor
(Edelman *et al.* 2019)	68	MI, Rest	LH, RH, LH+RH (Continuous cursor or robotic arm control)	User engagement
(Faller *et al.* 2019)	40	Visuo-motor	Virtual reality-based plane control	Arousal
(Sannelli *et al.* 2019)	80	MO, ME, MI	MO: LH, RH, Foot ME: LH, RH, RF MI: LH, RH, RF	Tiredness, imagination strength, motivation, uneasiness
(Saha *et al.* 2019a)	5	MI	RH, RF	Cortical regions of interest
(Perdikis *et al.* 2018)	2 (SCI)	MI	LH, RH, LH+RH, LF+RF, Rest	Mutual learning (parameters derived from interface-application, BCI output, and EEG)
(Darvishi *et al.* 2018)	10	MI	LH, RH	Reaction time
(Jochumsen *et al.* 2017)	47	ME	Palmar grasp	Motor training
(Saha *et al.* 2017b)	9	MI	LH, RH, LF+RF, Tongue	Optimal channels
(Úbeda *et al.* 2015)	5	ME	Continuous Cursor control	Kinematic parameters, i.e., speed, trajectory
(Jeunet *et al.* 2015)	18	Motor: LH Mental Imagery	Non-motor: mental rotation and mental subtraction	Personality and Cognitive Profile; Neurophysiological markers
(Kasahara *et al.* 2015)	30	MI	LH, RH (Finger-thumb opposition)	Gray matter volume
(Suk *et al.* 2014)	83	Attention task	LH, RH, Foot	Resting EEG

(*Subjects were healthy unless specified otherwise; SCI: spinal cord injury; MI: motor imagery; ME: motor execution; MO: motor observation; LH: left hand, RH: right hand; LF: Left Foot; RF: right foot)

2.4 Transfer Learning

2.4.1 Covariate shift and transfer learning

Transfer learning techniques originating from the field of machine learning have been adopted to compensate BCI systems for inter-subject and inter-session variability of EEG feature distributions (Fazli *et al.* 2015, Jayaram *et al.* 2016). A key idea is to regularise BCI model parameters for covariate shift adaptation. Covariate shift occurs when distributions of training and test data differ significantly although their conditional distributions may remain unchanged (Krusienski *et al.* 2011). Figure 2.1 schematically illustrates the idea of covariate shift when the training and test data distributions are different. The underlying time-variant and subject-specific brain dynamics depends on associated psychological and neurophysiological factors (Blankertz *et al.* 2009, Vidaurre and Blankertz 2010, Hammer *et al.* 2012, Jeunet *et al.* 2015, Sannelli *et al.* 2019, Ahn and Jun 2015, Reichert *et al.* 2015, Zhang *et al.* 2015b, Acqualagna *et al.* 2016, Vasilyev *et al.* 2017, Jensen *et al.* 2011) and cause covariate shift in EEG-derived feature distributions (Fazli *et al.* 2015, Jayaram *et al.* 2016, Krusienski *et al.* 2011).

The earliest attempts to overcome inter-session variability include preliminary training sessions to enhance the user's ability to modulate brain signals robust enough to control BCI (Wolpaw *et al.* 1991, Wolpaw and McFarland 1994, Birbaumer *et al.* 1999). The training sessions required for users are tedious and inconvenient. Therefore, machine learning-based BCI models were introduced to reduce individual training session for each BCI use, in which a model has to be calibrated based on the data at the beginning of each session (Ramoser *et al.* 2000, Blankertz *et al.* 2002). Recent studies have proposed SMR-based BCI without any session- and subject-specific calibration utilising the concept of transfer learning (Fazli *et al.* 2015, Jayaram *et al.* 2016, Fahimi *et al.* 2018, He and Wu 2019, Kang *et al.* 2009, Kang and Choi 2014, Saha *et al.* 2017a, Saha *et al.* 2017b, Saha *et al.* 2019a, Li *et al.* 2010, Lotte 2015, Niazi *et al.* 2013, Lu *et al.* 2010).

2.4.2 The concept of inter-subject associativity

Most of the existing transfer learning approaches are based on regularisation or inter-session/subject transfer of model parameters, indirectly transferring knowledge pertaining to the sources of intra- and inter-subject variability (Lotte 2015, Samek *et al.* 2013). Many works on transfer learning for SMR-based BCI proposed the use of a very

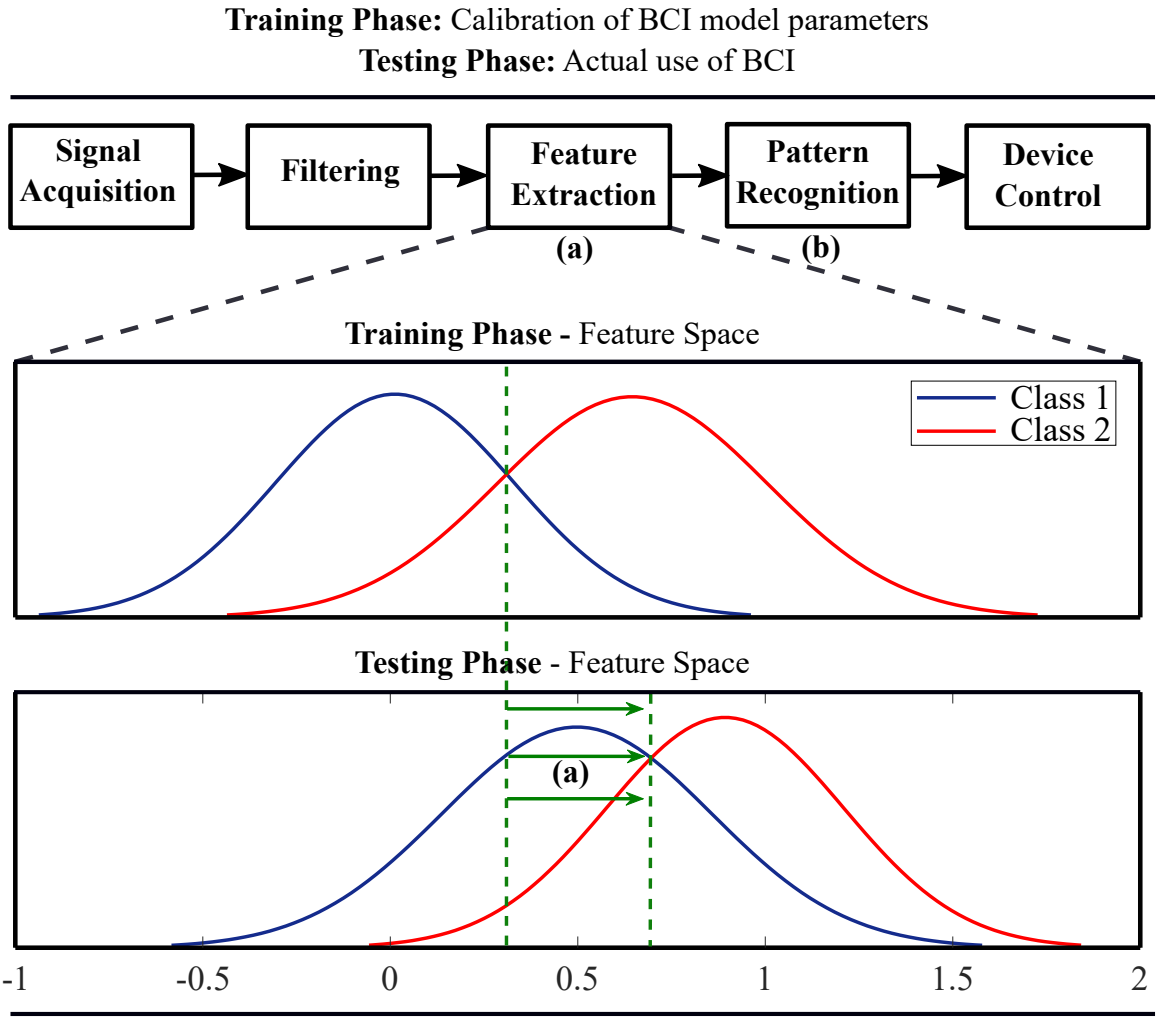

Figure 2.1. A schematic illustration of covariate shift in the feature space and application of transfer learning methods for covariate shift adaptation.

few training samples from the target subject (Lu *et al.* 2010, Fahimi *et al.* 2018, He and Wu 2019, Kang *et al.* 2009, Kang and Choi 2014). Recent studies have utilised resting EEG from the target subject incorporated into the transfer learning model before proceeding to the actual experiment (Morioka *et al.* 2015, Suk *et al.* 2014). While time and effort for building those models could be significantly reduced, they still require a training session. Others have recently demonstrated the feasibility of inter-subject BCI models without any training trial from the target subject (Saha *et al.* 2017a, Saha *et al.* 2017b, Saha *et al.* 2019a). However, their performance must be improved significantly prior to real-life use of such BCI systems.

A transfer learning method is worthwhile if the subjects share nonstationarities that can be modeled in an inter-subject context, but ineffective if the subjects exhibit unlike nonstationarities (Samek *et al.* 2013). The term *inter-subject associativity* refers to potential inter-subject BCI performance predictors, which could be incorporated into BCI design to augment transfer learning (Kang and Choi 2014, Wronkiewicz *et al.* 2015, Saha *et al.* 2017a, Saha *et al.* 2017b, Saha *et al.* 2019a). Source-space analysis for detecting inter-subject associative EEG channels can improve SMR-based BCI performance (Wronkiewicz *et al.* 2015, Saha *et al.* 2017a, Saha *et al.* 2019a). For example, the classification accuracies for two different subject pairs are $90.36 \pm 5.59\%$ and $63.21 \pm 8.43\%$, suggesting not both subject pairs can be used to achieve a good performance (Saha *et al.* 2019a).

A set of generalised BCI frameworks would be more feasible to implement as compared to a common BCI framework for all users. Because, it is evident to observe significant inter-subject variability in EEG signals (Saha *et al.* 2017b). Successful quantification of *inter-subject associativity* may suggest clustering of subjects, each cluster having subjects with EEG signal characteristics that are similar or can be interpreted in an inter-subject context. Considering the increasing volume of EEG-BCI databases, it may become feasible to quantify the exact sources of inter-subject/session variability as well as indicators of inter-subject associativity allowing training sessions to be reduced to a minimum (Lotte 2015). Recent advances in deep learning methods demonstrate a potential application that alleviates intra- and inter-subject variability in BCI settings (Chiarelli *et al.* 2018, Fahimi *et al.* 2018). Meanwhile, recent studies suggest that the quantification of *inter-subject associativity* could be equally important to increase the efficacy of only machine learning-based transfer learning strategies for covariate shift adaptation (Perdikis *et al.* 2018, Saha *et al.* 2019a, Saha *et al.* 2017b, Wronkiewicz *et al.* 2015, Kang *et al.* 2009, Kang and Choi 2014).

2.5 Conclusion

Intra- and inter-subject variability is undeniable due to time-variant factors related to the experimental setting and underlying psychological and neurophysiological parameters. Besides recent extensive use of transfer learning methods for the covariate shift adaptation, many recent works have sought to find suitable psychological and neurological predictors for BCI performance. The assimilation of such predictors into a

subject independent context may reduce or eliminate the tedious session or subject-specific training by supplementing the performance of existing transfer learning methods. However, collecting *a priori* information related to BCI performance predictors could be challenging. Inter-subject topographical associativity characterised by resting EEG could provide a viable alternative solution to reduce the calibration time to a minimum (Northoff *et al.* 2010, Suk *et al.* 2014, Morioka *et al.* 2015) assuming we understand the significance of intrinsic brain activities, i.e., resting EEG signals, and the role of RSN topographies on SMR-related brain functions.

Chapter 3

Localisation of Inter-subject Sensorimotor Cortical Source

THIS chapter introduces an event-related cortical sources estimation technique from subject-independent EEG recordings for SMR-based BCI. By using wavelet-based maximum entropy on the mean (wMEM), task-specific EEG channels are selected to predict right hand and right foot sensorimotor tasks, employing common spatial pattern and regularised common spatial pattern. EEG from five healthy individuals were evaluated by a cross-subject paradigm. Prediction performance was evaluated via a two-layer feed-forward neural network, where the classifier was trained and tested by data from two subjects independently. The highest mean prediction accuracy achieved for a specific subject pair by using selected EEG channels was on average (90.36 ± 5.59) and outperformed that achieved by using all available channels (86.07 ± 10.71). Spatially projected cortical sources approximated using wMEM may be useful for capturing inter-subject associative sensorimotor brain dynamics and pave the way towards an enhanced subject-independent BCI.

Associated Publication: *Saha, S.*, M.S. Hossain, K. Ahmed, R. Mostafa, L. Hadjileontiadis, A. Khandoker and M. Baumert, "Wavelet entropy-based inter-subject associative cortical source localization for sensorimotor BCI", Frontiers in Neuroinformatics, vol. 13, 2019.

3.1 Introduction

Most BCI require subject-specific training sessions, which can annoy users and limit BCI applications such as affective states assessment (Andujar *et al.* 2015), lie detection (Wang *et al.* 2016), and gaming (van de Laar *et al.* 2013). Furthermore, not all the users are able to control BCI due to BCI illiteracy (Allison and Neuper 2010) and spatio-temporally complex RSN dynamics over time and across individuals (Jensen *et al.* 2011). Many factors, including time-variant psychophysiological, neuroanatomical traits and user's basic characteristics, essentially cause unreliable estimates of RSNs, which engender short and long-term brain signal variation over time and across individuals (Goncalves *et al.* 2006, Zhang *et al.* 2015a, Acqualagna *et al.* 2016, Kasahara *et al.* 2015, Ahn and Jun 2015, Athanasiou *et al.* 2017). Resting state EEG-derived spectral entropy and power spectral density are associated with sensorimotor BCI performance (Zhang *et al.* 2015a, Acqualagna *et al.* 2016). Attention and motivation are psychological predictors that reflect sensorimotor BCI performance (Hammer *et al.* 2012). Taking anatomical information such as electrode positioning and head morphologies into consideration can augment subject-to-subject transfer learning and thus BCI performance (Wronkiewicz *et al.* 2015).

The inter-subject and inter-session variabilities of brain dynamics significantly degrade the performance of EEG-based BCI (Saha *et al.* 2017b). Subjects who show dissociative brain responses, i.e., responses with negligible commonalities across individuals, cannot be accommodated by a generic BCI framework. On the contrary, subjects showing significant commonalities in their brain responses achieve relatively high performance in the context of subject independent MI classification (Saha *et al.* 2017b, Saha *et al.* 2017a). A recent EEG-based experiment on drowsiness detection signifies the influences of intra- and inter-subject variability and has proposed multi-subject transfer framework for reducing calibration time (Wei *et al.* 2018).

This chapter explores inter-subject associative brain responses to identify pairs of individuals who demonstrate similar EEG dynamics during MI tasks. We anticipate higher classification accuracy in people with higher inter-subject associativity. Previous works used the Indian Buffet process and Kullback-Leibler divergence to identify inter-subject associative individuals prior to classifying multi-subject EEG signals and showed that inter-subject associativity could be potentially used for multi-subject

subspace learning (Kang *et al.* 2009, Kang and Choi 2014). Thus, inter-subject associative BCI could eliminate the need for subject-specific calibrations despite differences in cortical activities across subjects, mostly because of various time variant psychophysiological factors (Goncalves *et al.* 2006) and individuals' basic characteristics (Ahn and Jun 2015). Compensating for inter-subject difference in brain responses can be crucial for improving BCI performance. One approach is to select inter-subject associative EEG channels that exhibit robust activation during specific cortical tasks (Saha *et al.* 2017a). The implicit assumption is that eliminated channels represent RSN and subject-specific MI dynamics free from signatures that are common between subjects. Moreover, individual brain dynamics sometimes show inter-subject cortical association during external stimulation, i.e., visual (Hasson *et al.* 2004) and auditory (Abrams *et al.* 2013) events. Subjects having common psychological perspective share associative brain responses during natural vision (Lahnakoski *et al.* 2014). An ensemble of classifiers has been used to classify mental states from single trial inter-subject EEG recordings (Fazli *et al.* 2009). In carefully selected subjects, common spatial pattern (CSP)-based subspaces learning methods deal with inter-subject/session data efficiently (Samek *et al.* 2013, Samek *et al.* 2014). Subject independent BCI is currently feasible (Abibullaev *et al.* 2013) and could be used in research, rehabilitation and gaming. A recent study used a particle swarm optimization based inter-subject common feature learning technique for BCI implementation without subject-specific training (Atyabi *et al.* 2017). An unsupervised spectral transfer using information geometry has shown promising classification accuracy in cases using fewer or no trials from the target subject (Waytowich *et al.* 2016).

The aim of this study is to identify inter-subject associative electromagnetic sources, estimated from wavelet-based maximum entropy of the mean (wMEM) on single trial EEG, and project them into a three-dimensional (3D) head model. Results show that wMEM captures associative inter-subject sensorimotor dynamics, which can be utilised to assess inter-subject cortical associativity.

3.2 Methods

3.2.1 Data and experimental settings

We used dataset IVa of BCI Competition III, comprising of EEG of five healthy subjects specified as *aa*, *al*, *av*, *aw* and *ay* recorded during right hand and right foot MI

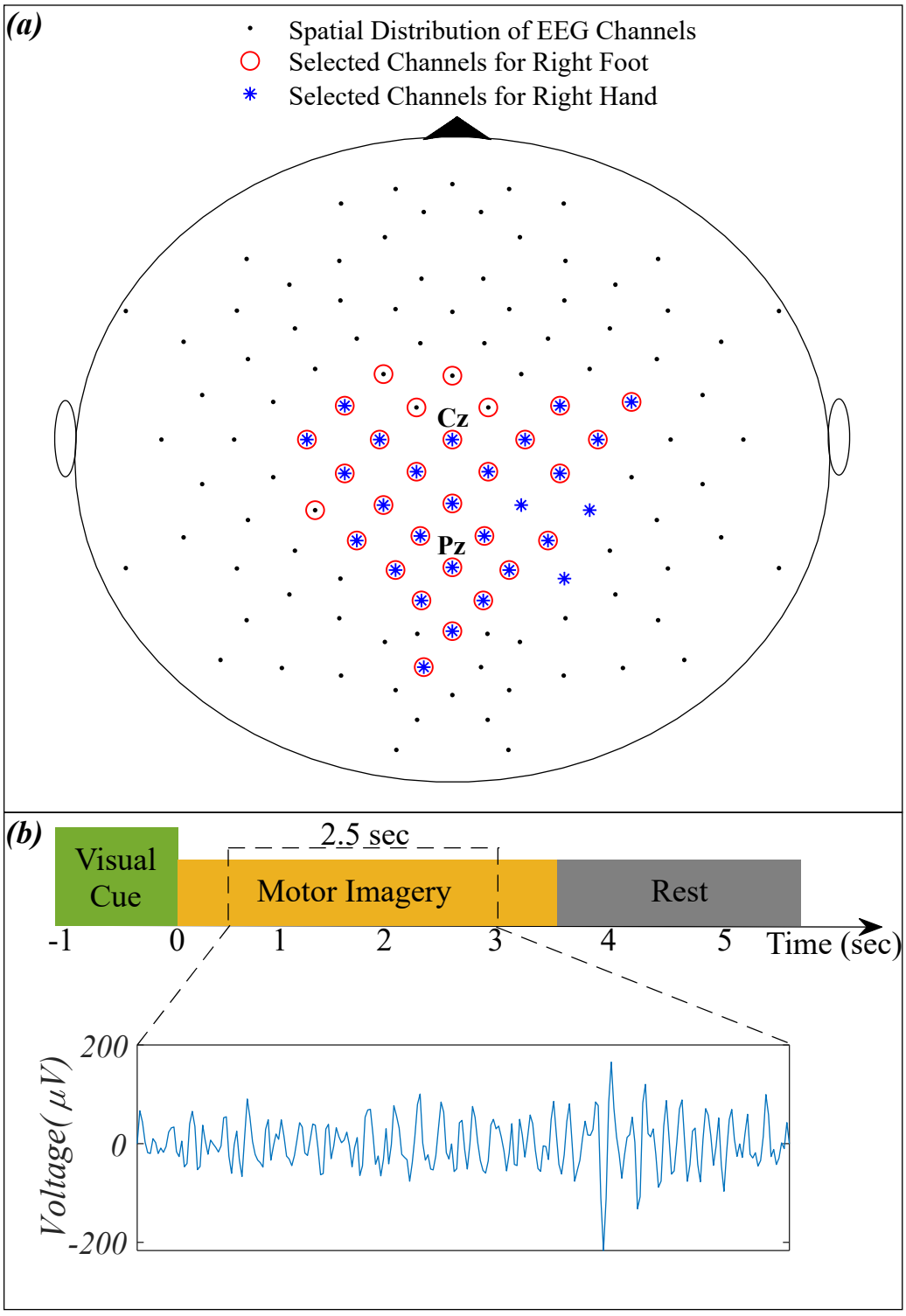

Figure 3.1. (a) Spatial distribution of 118 EEG channels based on the extended International 10/20 System and selected channels for subject pair $al - ay$; (b) Timing of the recording paradigm for dataset IVa of BCI Competition III and example of selected 2.5 seconds EEG signal for channel *Cz*.

(Blankertz *et al.* 2006). The dataset consists of 280 trials for each subject, i.e., 140 trials for each class. A visual cue was given before each trial, consisting of 3.5 sec of EEG recordings with 118 electrodes (Extended 10/20 system). To eliminate the effect of visual cues, 2.5 sec of recordings following 0.5 sec of the visual cues were considered corresponding to MI for experimentation. Figure 3.1 illustrates the spatial distribution of EEG channels (Extended 10/20 System) and the timing of recording paradigm.

Two experiments for evaluating the inter-subject associative sources and estimating the inter-subject classification performance, respectively, were carried out on any two subjects at once as shown in Figure 3.2, i.e., all possible pairs of the subjects set were considered. Then, we compared the classification performance achieved by using all 118 channels versus that achieved by the selected channels.

Any two subjects' EEG from the set of five participants (*aa*, *al*, *av*, *aw* and *ay*) are represented as X and Y, respectively. The total number of trials Tr available for each subject (280) was divided into 10 equal sets as follows:

$$X = [x_1, x_2, ..., x_{10}]; Y = [y_1, y_2, ..., y_{10}]. \tag{3.1}$$

Then, sets of inter-subject EEG are formed:

$$XY = [x_1y_1, x_2y_2, ..., x_{10}y_{10}], \tag{3.2}$$

where each component of XY contains $\frac{Tr}{10}$ trials from subject X that were used to train the classifier and $\frac{Tr}{10}$ trials from subject Y that were used to test the classifier. On each set of XY, wMEM was computed to estimate inter-subject associative cortical sources and to test the classification performance. The classification performance was averaged over the ten sets.

Figure 3.2 shows the block diagram demonstrating the experimental settings corresponding to preprocessing, channel selection and classification of inter-subject EEG signals. In the preprocessing step, inter-subject set of EEG trials were band-pass filtered (8 Hz and 40 Hz), using a Butterworth filter of order ten (Saha *et al.* 2017b, Saha *et al.* 2017a). For each class, trials were separated to apply the wMEM method to investigate class-specific inter-subject associative cortical sources and then to select EEG channels representing the mostly activated sensorimotor sources. The union of two channel sets corresponding to right hand and right foot was considered the optimal channel set for a specific subject pair. The numbers of channels used in this study varied between two different cases: *Case I* – all available 118 channels were employed for classification;

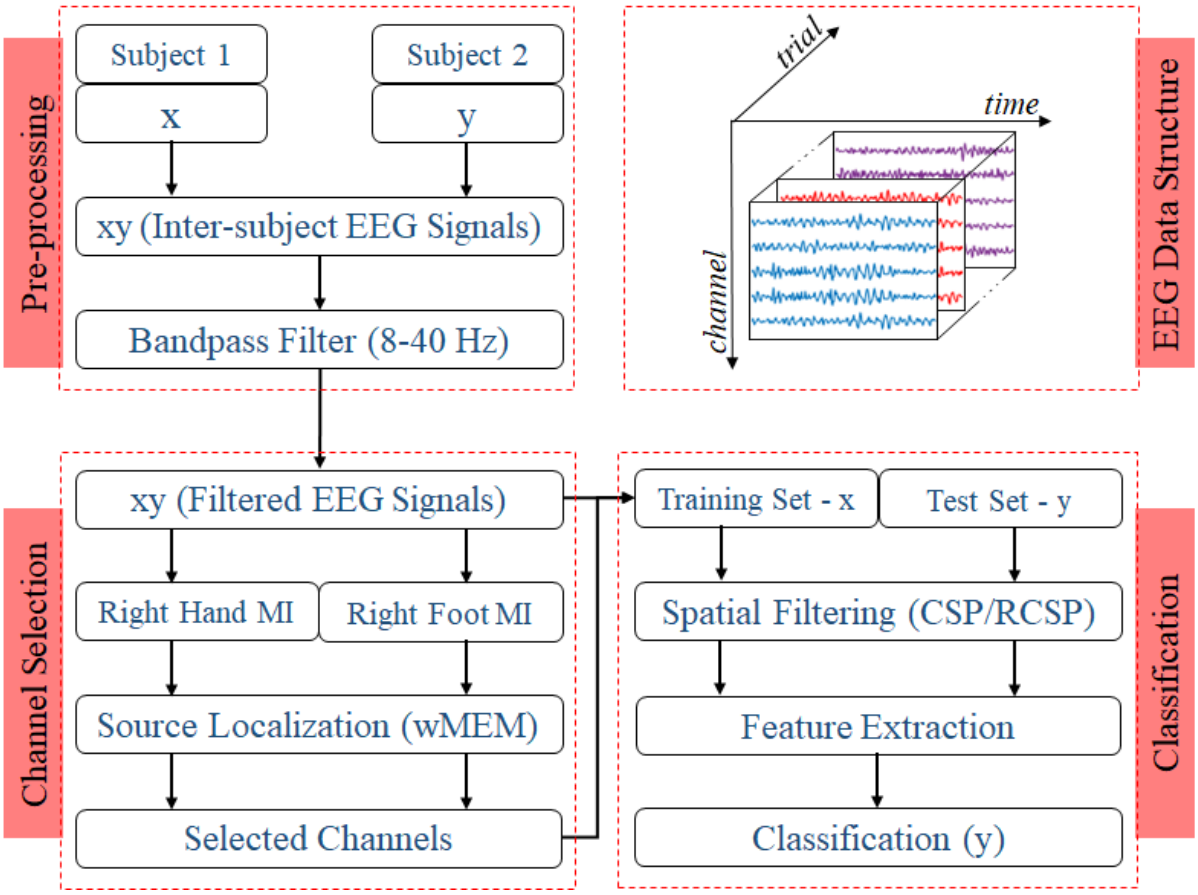

Figure 3.2. Block diagram representing the EEG trial structure and the proposed methodology to identify inter-subject associative EEG channels and to evaluate the BCI performance. Preprocessing step includes constructing a set of EEG trials from two different subjects with a ratio of 1:1 and applying a Bandpass filter with corner frequencies of $8Hz$ and $40Hz$. Inter-subject trials are separated according to the nature of motor imagery tasks, i.e., right hand or right foot. Then the class-specific set of trials were used to estimate inter-subject cortical sources and consequently EEG channels. For evaluating the BCI performance, trials from one subject were used to establish the single-trial BCI classifier model, which was then evaluated on the trials acquired from a different subject.

Case II – only those channels selected by the wMEM approach (<118) were employed for classification. Apart from the numbers of channel, all other parameters were kept identical for evaluating BCI classification performance.

To evaluate inter-subject BCI performance, CSP without and with covariance estimation regularisation (Ramoser *et al.* 2000, Lotte and Guan 2011) were computed to spatially project multichannel EEG. Wavelet decomposition-based subband entropy

(Daubechies 3, level: 3) was calculated to obtain features (Saha *et al.* 2017b, Saha *et al.* 2017a) for a two-layer feed-forward neural network classifier as described previously (Svozil *et al.* 1997).

3.2.2 Wavelet-based source localisation

Time-frequency forward model and source distribution

Assuming that oscillatory brain activities result from underlying processes occurring at different frequency bands located in extended cortical areas (Lina *et al.* 2014), a *time-frequency (t-f)* forward model utilising discrete wavelet transform of the data as well as the brain sources along with spatial clustering in homogeneous parcels can be defined (Tadel *et al.* 2011). To calculate the discrete wavelet transform, real Daubechies filter banks with four vanishing moments were used. The complete details of the numerical implementation of wMEM method can be found in (Lina *et al.* 2014). In this study, we assume that single trial inter-subject EEG signals result from diverse physiological background activity and MI induced cortical activities. Ensemble-averaging over class-specific MI trials effectively reduces the effect of independent physiological fluctuations, and thus offers a potential tool for locating sensorimotor cortical sources. The underlying hypothesis is that wMEM-based cortical sources on an inter-subject EEG trials set would give only inter-subject associative cortical sources, in which only the inter-subject common EEG patterns related to right hand or right foot MI are detected.

The *t-f* forward model depends on the lead field matrix that governs the relationship between co-registered bioelectric sources and the set of sensors. A generalised anatomical MRI template (ICBM152), estimated from MRI scans acquired from 152 healthy subjects, was used to create a realistic head model (Fonov *et al.* 2011). The template is included in the Brainstorm software (Tadel *et al.* 2011). The template comprises of three head layers, i.e., scalp, outer skull and inner skull, which were approximated using T1 MRI sequences. It exhibits greater contrast and captures fine definition of top boundary of the brain. OpenMEEG software was then used to solve the steady-state Maxwell's equations to calculate the lead field matrix by establishing a realistic relationship between the bioelectric sources in the ICBM152 and the co-registered sensors on the scalp (Gramfort *et al.* 2010).

The EEG inverse solution utilises a distributed source model, where a large number of dipolar sources is disseminated beside the cortical surface. Depending on the anatomical restrictions, each dipole is oriented orthogonally with the local cortical surface. The linear relation of the source amplitude to the recordings can be written as

$$\mathbf{M} = \mathbf{GJ} + \mathbf{E}, \tag{3.3}$$

where $\mathbf{M}$ is the recording matrix of dimension $(q \times \tau)$ which contains EEG signals of q channels at τ time samples. $\mathbf{E}$ represents Gaussian recording noise. $\mathbf{J}$ is an unknown matrix of the size $(r \times \tau)$ that represents the current density of the r dipolar sources along the tessellated cortical surface. $\mathbf{G}$ represents the lead field matrix $(q \times r)$ and is estimated by solving the *t-f* forward problem that evaluates the contributions of every dipolar source on the electrodes. Hence, the inverse solution approximates $\mathbf{J}$ from the recorded data $\mathbf{M}$ and the evaluated lead field matrix $\mathbf{G}$.

wMEM inverse solution

Solving the ill-posed inverse problem of source localisation requires some *a priori* information to be incorporated inside the regularisation framework so that a unique solution is obtained. In the *MEM* framework, the amplitude of the sources J is considered a multivariate random variable j of length r that has a probability distribution $dp(j)$. In the *MEM* framework, to regularise the inverse problem some previous knowledge on j is incorporated as reference distribution $dv(j)$. This reference distribution represents a realistic spatial model which presumes the brain activity is organised into $K(K << r)$ cortical parcels and every parcel is related to a secret state variable. This variable controls the parcel's activity, whether or not the parcel is active during a certain activity. A data driven parcellization method is used to spatially cluster the cortical surface into K nonoverlapping parcels. The technique consists of first applying a projection method named as the multivariate source prelocalisation technique, estimating a probability-like coefficient for every dipolar sources distributed along the cortical mesh. This coefficient characterises the contribution of every source to the data, followed by region growing around local maxima.

In the *MEM* reference model, every parcel is assigned a secret variable to model the probability of the parcel's activity, whether or not it is active. It is to be noted that the multivariate source prelocalisation coefficients of all the sources within the parcel was used to initialize this probability. Based on the state of activation of the parcels,

MEM inference can switch any of these parcels on or off. It is also able to approximate a contrast of source intensities within the selected active parcels. Usually, *MEM* is applied for solving the inverse problem in the time domain. *wMEM* is the wavelet variant of MEM that operates in the *time-frequency* (Lina *et al.* 2014).

While the joint probability of the wavelet coefficient of all sources at a specific time and scale is represented as $p(w)$, the *MEM* estimation deduces the expectation $E_p[w]$ by assuming a reference probability $\mu(w)$ from which the entropy deviation is minimised under the goodness-of-fit data constraint. The entropy $S_\mu(f)$ of any μ density, $p(w) = f(w)\mu(w)$, can be described as follows:

$$S_\mu(f) = -\int_w f(w) ln f(w) \mu(w) dw, \tag{3.4}$$

where w is the wavelet coefficients of the sources. The optimum solution is given by $w^* = E_{p^*}[w]$, where $p^*(w) = f^*(w)\mu(w)$, considering

$$\begin{cases} f^* = argmax_f S_\mu(f). \\ _{with} \int_w \mathbf{G} w f(w) \mu(w) dw = d^*, \end{cases} \tag{3.5}$$

where d^* can be obtained from $d^* = W^{-1}\delta_\tau(Wd)$ and $W = \sum_d^{-\frac{1}{2}}$ is the whitening matrix. This whitening matrix can be evaluated from a baseline EEG recording assuming no signal of interest is contained in the baseline recording. $\delta_\tau(w)$ represents the soft shrinkage of the wavelet coefficient which can be defined as

$$\delta_\tau(w) = \left(1 - \frac{\tau}{|w|}\right)_+ w, \tag{3.6}$$

where $w_+ = w$ for $w > 0$ and $w_+ = 0$ for other cases. The threshold τ of each channel is obtained from the variance of the highest frequency wavelet coefficients, evaluated using a median estimator.

With respect to optimum μ-density f^*, the mean of the wavelet coefficients of the sources is used to estimate the expectation of the coefficient. Finally, the expectation of the coefficient with respect to the f^*, can be expressed as the *a posteriori* mean estimate of the wavelet coefficients:

$$w^* = \int w f^*(w) \mu(w) dw = \frac{d}{d\xi} F_\mu^*(\xi) \Big|_{\xi = G^t \lambda^*}, \tag{3.7}$$

with $F_\mu^*(\xi) = ln \int e^{\xi^t w} \mu(w) dw$ and $lnZ(\lambda) = F_\mu^*(G^t\lambda)$. In (3.7) λ^* is the unique solution of

$$\lambda = argmax_\lambda D(\lambda)$$

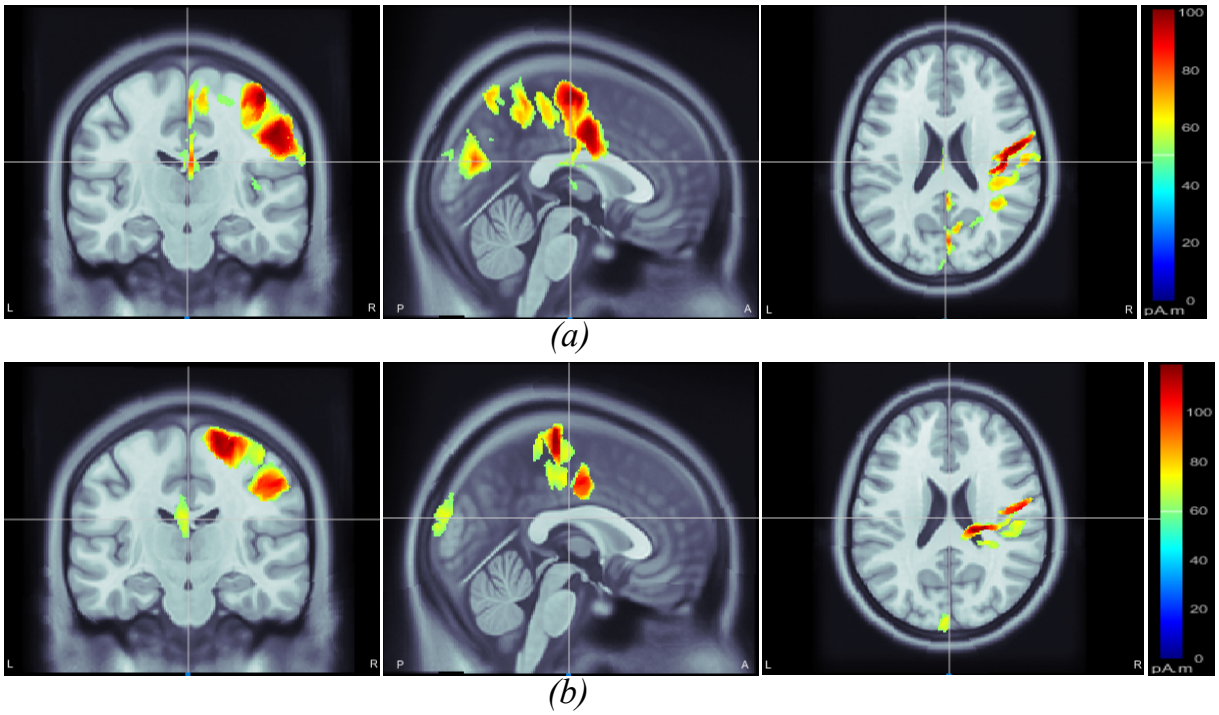

Figure 3.3. Motor imagery induced inter-subject (subject pair *al-ay*) cortical sources on a MRI head model estimated via wMEM: from left-right, coronal view, sagittal view and axial view, respectively for two motor imagery tasks: (a) right hand and (b) right foot movement.

where

$$D(\lambda) = \lambda^t d^* - F_\mu^*(G^t\lambda) - \frac{1}{2}\lambda^t \eta^* \lambda$$

and η^* is a covariance matrix of residual noise.

For localising cortical sources, either the time courses of the sources obtained by inverse wavelet transform or spatial cortical map of the wavelet coefficients have been considered. A complete description of wMEM-based localisation can be found in (Lina *et al.* 2014).

To implement the wMEM-based source localisation for the inter-subject EEG, the open source Brainstorm software was used (Tadel *et al.* 2011). MI-induced sources were projected into the 3D anatomical head model. For each class, all available trials were averaged and a noise covariance matrix was estimated. Finally, the *BrainEntropy MEM* with the *wMEM* option was used to calculate the sources from the averaged data.

Inter-subject associative EEG channel selection

Following class-specific wMEM-based cortical source localisation, careful visual inspection on the MRI head images (i.e., coronal, sagittal and axial view) and 3D cortex

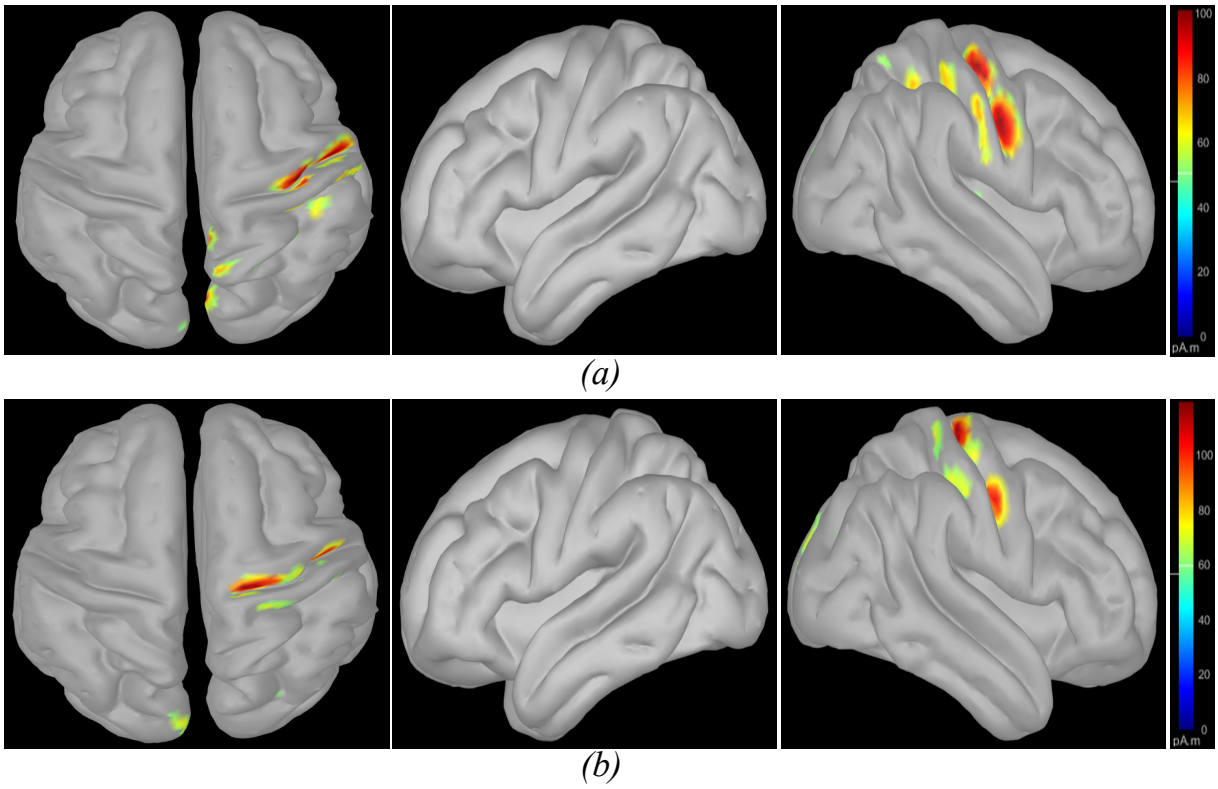

Figure 3.4. wMEM based inter-subject (subject pair *al-ay*) associative cortical source localisation illustrated on 3D cortex cartoon model: from left-right, top view, side view (right hemisphere) and side view (left hemisphere), respectively for (a) right hand and (b) right foot motor imagery. In (b), the activity visible on the top view is not clearly projected on the side view (left hemisphere) as the activated sources lie mostly within relatively inner part of the cortex (in between gyri).

cartoon model as shown in Figure 3.3 and Figure 3.4, respectively, was carried out. For each class, all time instances were examined for activated sources within the trial duration, i.e., 0-2.5 sec. The EEG channels located on/around the estimated sources on the 3D head model template were considered as task-specific inter-subject associative optimal channels. Figure 3.3 and Figure 3.4 illustrate inter-subject associative cortical source estimation for subject pair *al-ay* at a time instance. Notably, 3D cortex head model can be examined visually by rotating the view at any of the 360°.

3.2.3 Common spatial pattern with and without regularisation

The aim of CSP is to maximise the difference between class specific features (Ramoser *et al.* 2000). Here, we use CSP with tuning the covariance estimation, which effectively deals

with undesired outliers and is suitable in case of small training trials (Lu *et al.* 2010, Lotte and Guan 2011).

The EEG signal is represented by $\mathbf{E}$ and of size $N \times P$, where N is the number of channels and P is the number of samples per trial. For the conventional CSP algorithm, estimation of the sample based covariance matrix is required. The sample covariance matrix of a trial $\mathbf{E}$ is normalised to the total variance as (Lu *et al.* 2010, Ramoser *et al.* 2000).

$$\mathbf{S} = \frac{\mathbf{E}\mathbf{E}^T}{\text{trace}\left[\mathbf{E}\mathbf{E}^T\right]}, \tag{3.8}$$

where ^{T} denotes the transpose of a matrix.

If K trials are available for training corresponding to each class for a subject, indexed by k as $\mathbf{E}_{(\mathbf{c},\mathbf{k})}$ that refer to the $S_{(c,k)}$, based on (7), $k = 1, 2, ..., K$, the mean sample covariance matrix across the trials is given by

$$\bar{\mathbf{S}}_c = \frac{1}{K}\sum_{k=1}^{K}\mathbf{S}_{(\mathbf{c},\mathbf{k})}, \tag{3.9}$$

where $c \in \{1, 2\}$ represents two classes of the trial associated with the MI tasks.

The discriminative spatial patterns in CSP are calculated based on the sample mean covariance matrix estimation based on (3.9). The next section will introduce regularisation in CSP.

Covariance matrix estimation with regularisation:

Regularisation is achieved by biasing the covariance estimation away from their sample-based values towards more physically plausible values, which reduces the variance of the sample-based estimates while tending to increase bias (Lu *et al.* 2010). This is done by using one or more regularisation parameters (i.e., β and γ in this paper).

The regularised average spatial covariance matrix for each class is defined as

$$\widehat{\sum}_c(\beta,\gamma) = (1-\gamma)\widehat{\mathbf{\Omega}}_c(\beta) + \frac{\gamma}{N}\text{trace}\left[\widehat{\mathbf{\Omega}}_c(\beta)\right]\cdot\mathbf{I}. \tag{3.10}$$

Here, β and γ are regularisation parameters $(0 \leq \beta, \gamma \leq 1)$ and $\mathbf{I}$ is the identity matrix. $\widehat{\mathbf{\Omega}}_c(\beta)$ comprises the covariance matrix for the trials from the specific subjects, as well as generic trials, and is given by

$$\widehat{\mathbf{\Omega}}_c(\beta) = \frac{(1-\beta).\mathbf{S}_c + \beta.\widehat{\mathbf{S}}_c}{(1-\beta).M + \beta.\widehat{M}}. \tag{3.11}$$

Here, $\mathbf{S}_c$ is the sum of the sample covariance matrices for all M training trials for class c :

$$\mathbf{S}_c = \sum_{k=1}^{K} \mathbf{S}_{(c,k)}. \tag{3.12}$$

$\widehat{\mathbf{S}}_c$ is the sum of the sample covariance matrices for $\widehat{K}$ generic training trials with covariance matrix $\mathbf{E}_{(c,\hat{k})}$ for class c:

$$\widehat{\mathbf{S}}_c = \sum_{\hat{k}=1}^{\widehat{K}} \mathbf{S}_{(\mathbf{c},\widehat{\mathbf{k}})}. \tag{3.13}$$

Here, $\mathbf{S}_c$ and $\widehat{\mathbf{S}}_c$ are normalised and are analogous to the sample covariance matrix in (6.1). The objective of $\widehat{\mathbf{S}}_c$ is to reduce the variance in the covariance matrix estimation and produce more reliable results.

Feature Extraction In RCSP

The regularised composite spatial covariance is formed and factorised as (Lu *et al.* 2010)

$$\widehat{\sum}(\beta,\gamma) = \widehat{\sum}_1(\beta,\gamma) + \widehat{\sum}_2(\beta,\gamma) = \widehat{\mathbf{U}}\widehat{\wedge}\widehat{\mathbf{U}}^T. \tag{3.14}$$

Here, $\widehat{\mathbf{U}}$ denotes the matrix eigenvectors and $\widehat{\wedge}$ denotes the diagonal matrix of corresponding eigenvalues. The eigenvalues are assumed to be sorted in descending order throughout this paper (Lu *et al.* 2010), (Ramoser *et al.* 2000).

Finally, the projection matrix is formed as (Lu *et al.* 2010)

$$\widehat{\mathbf{W}} = \widehat{\mathbf{B}}^T\widehat{\wedge}^{-1/2}\widehat{\mathbf{U}}^T, \tag{3.15}$$

where $\widehat{\mathbf{B}}$ denotes the matrix of eigenvectors for the whitened spatial covariance matrix and defined as

$$\widehat{\mathbf{B}} = \widehat{\wedge}^{-1/2}\widehat{\mathbf{U}}^T\widehat{\sum}_c(\beta,\gamma)\widehat{\mathbf{U}}\widehat{\wedge}^{-1/2}. \tag{3.16}$$

In RCSP, an input trial E is projected as (Lu *et al.* 2010)

$$\widehat{\mathbf{X}} = \widehat{\mathbf{W}}^T\mathbf{E}. \tag{3.17}$$

To obtain the most discriminative features for both classes, the optimal channels are to be selected from the leftmost and rightmost channels. For example, the first channel

Table 3.1. Number of selected EEG channels.

Subject Pair	RH	RF	Total
aa-al	36	36	43
aa-av	33	39	42
aa-aw	40	42	44
aa-ay	42	37	45
al-av	36	37	43
al-aw	40	23	46
al-ay	28	30	33
av-aw	42	37	46
av-ay	47	45	55
aw-ay	46	54	59

(RH: Right Hand, RF: Right Foot)

represents the most distinguished features for class 1 and the last channel represents the most distinguished features for class 2. As the channel selection converges to the central channel of the $\widehat{\mathbf{X}}$, the features become poor and may hardly distinguish different classes. It is to be noted that RCSP equals traditional CSP when $\beta = \gamma = 0$. The following combinations of γ and β values were considered during regularisation (Wang *et al.* 2006, Lu *et al.* 2010, Saha *et al.* 2017b):

$\beta = (0, 0.001, 0.01, 0.1, 0.2, 0.3, 0.4, 0.5, 0.6, 0.7, 0.8, 0.9)$

$\gamma = (0, 0.01, 0.1, 0.2, 0.3, 0.4, 0.5, 0.6, 0.7, 0.8, 0.9)$.

A total of four CSP components, two for each class, were selected for extracting features (Wang *et al.* 2006).

3.3 Results and Discussion

3.3.1 Selection of inter-subject associative channels

Figure 3.3 and Figure 3.4 illustrate inter-subject associative source locations for subject pair *al-ay* at a time instance. Table 3.1 lists the total number of selected channels used to classify MIs (*Case II*). Although the number of selected channels differed between right hand and right foot MI, many common channels were identified for both classes. Some of the projected cortical sources lie within deeper regions of the brain, thus maintaining

good signal-to-noise ratio in the scalp EEG becomes critical. Modelling the signal attenuation from cortical sources located within deeper brain areas to the EEG electrode montages might play an important role for dealing with noise efficiently (Cosandier-Rimélé *et al.* 2008). Specific parts of the interconnected cortico-subcortical networks show sensorimotor signatures. For example, basal ganglia and the ventrolateral part of the thalamus show sensorimotor activations (Gerardin *et al.* 2000, Hétu *et al.* 2013). Projections of sensorimotor activities to deeper brain areas are present in motor cortex and supplementary area (Hétu *et al.* 2013). Possibly, sensorimotor activities in subcortical networks manifest in EEG signals. Previous works have exploited subject-specific EEG source localisation based information for improving sensorimotor BCI performance (He *et al.* 2015, Congedo *et al.* 2006). The cortical sources corresponding to MI shown in Figure 3.3 and Figure 3.4 lie mostly within subcortical areas. The validation of the implication about the subcortical sources as mostly activated during inter-subject MI requires further investigation. Notably, it has been hypothesized that the estimated sources delineate only the inter-subject associative sources; the MI sources that are not common in the subject pair should not present in this experimental context, because the source localisation method was applied on inter-subject set of EEG comprising equal number of trials from each subject.

3.3.2 Motor imagery prediction performance

Table 3.2 shows the MI prediction performance averaged over ten sets of inter-subject data of two subjects. Each set consisted of 56 trials in total, the first 28 trials from a subject were used to train the classifier and the remaining 28 trials from another subject were used to evaluate the performance. Each subject pair was used twice, alternating the training and evaluation subjects. The highest prediction performance $(90.36 \pm 5.59\%)$ was achieved for subject pair *ay-al* using CSP with covariance regularisation. This demonstrates the feasibility of inter-subject BCI for subjects who show similar EEG patterns. In this case, only 33 of the 118 available channels were employed, reflecting the inter-subject associative cortical areas. Alternating the order of training and evaluation trials for subject pair *al-ay* reduced the prediction performance to $(84.64 \pm 13.15\%)$, suggesting that the performance of CSP depends on the training data. Since CSP is a data driven method it can be overfitted, adapting to outliers in the training set (Sannelli *et al.* 2016). Tuning of the covariance estimation via

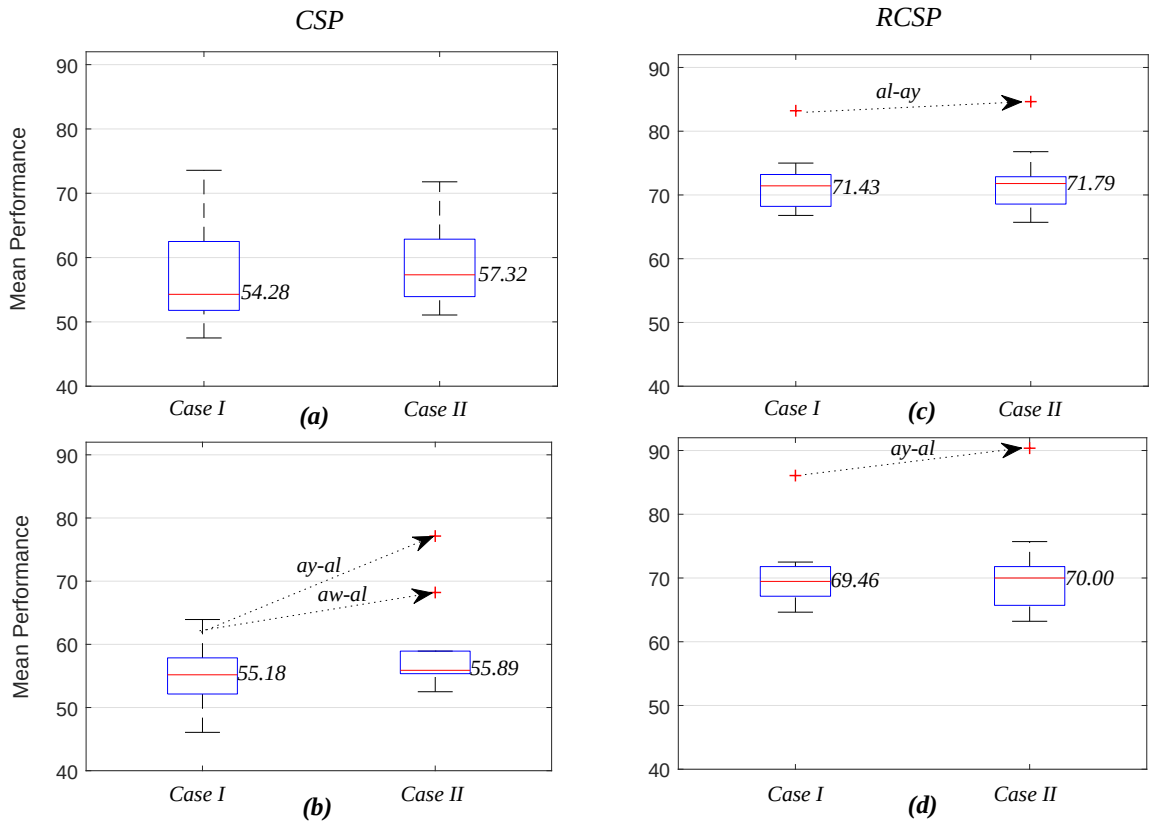

Figure 3.5. Box plots illustrating mean prediction performances for different subject pairs: the performances were measured while applying common spatial pattern (c)-(d) with (RCSP) and (a)-(b) without (CSP) covariance estimation regularisation.

two regularisation parameters, γ and β can alleviate this problem. Overall, regularisation of the covariance matrix enhanced prediction performances compared to standard CSP. For subject pair *aa-al*, significant improvements in performances were evident ($64.64 \pm 14.33\%$ vs. $76.79 \pm 9.11\%$), further demonstrating the potential of wMEM as a tool for localising inter-subject associative cortical sources.

Figure 3.5 compares average prediction performance and highlights cases where selected EEG channels outperformed results obtained when using all available 118 channels. In Figure 3.5, (a) and (c) compare the mean performances of the first ten subject pairs summarised in Table 3.2, while (b) and (d) compare the mean performances of the last ten subject pairs for CSP without and with covariance regularisation, respectively. Applying CSP with covariance estimation, the median values of average classification accuracies for the first ten subject pairs using all channels and selected channels are 71.43% and 71.79%, respectively, while they were 69.46% and 70% for the last ten subject pairs. Thus, the overall results might not indicate a generalised trend

of improved performance of inter-subject BCI performance. However, particular subject pair-specific $(al - ay)$ improved performance would suggest a novel application of wMEM and a probable role in investigating inter-subject sensorimotor dynamics. A reduced number of channels can be used to achieve comparable performance while lessening the computational cost.

3.3.3 Enhanced inter-subject associative sensorimotor dynamics

Localising task-induced cortical sources is important because specific sources provide more informative and inter-class distinguishable attributes for predicting sensorimotor events. The minimum current estimates algorithm, applied to magnetoencephalogram recordings, suggest that the contralateral motor cortex is highly active during intended movement direction (Wang *et al.* 2010b). Estimating sensorimotor cortical sources with fine spatial resolution EEG source imaging could augment BCI in decoding complex MI tasks (Edelman *et al.* 2016). Measurement of entropy by different means was shown to be useful for cortical source localisation. For example, Von Neumann entropy was applied to classify MI tasks (Kamousi *et al.* 2007) and wavelet ridge analysis-based MEM was applied to localise EEG sources (Zerouali *et al.* 2013). However, the cortical sources widely vary in the spatiotemporal domain across subjects that makes the inter-subject source localisation challenging, as is evident from an electromagnetic spatiotemporal independent component analysis-based multi-subject EEG study (Tsai *et al.* 2014).

Selecting inter-subject associative cortical sources can not only be used to sort out optimal task-induced EEG channels, but also can provide enhanced weight of associativity between subjects. Not well-understood variability due to functionally relevant RSN (Wens *et al.* 2014) and sometimes outliers (Arvaneh *et al.* 2011) manifest in undesired channels, which negatively contribute to the prediction performance. Basically, efficiently dealing with the EEG inverse problem is challenging as the solution is non-unique and unstable (Grech *et al.* 2008). However, the results presented here have demonstrated that wMEM is a potential tool for approximating cortical sources originating inside/on the cortico-subcortical networks. Improved prediction accuracies with reduced number of selected inter-subject channels indicate enhanced associativity of the subjects' sensorimotor dynamics. In (Hossain *et al.* 2016), wMEM was adopted as a channel selection tool in subject-specific BCI settings in the first instance. Clarke and Janday proposed MEM for solving the inverse problem (Clarke and Janday 1989)

and Rice had proposed this method as the most probable solution to the inverse problem in EEG considering realistic neurophysiological constraints (Rice 1990). Lina *et. al.* have recently proposed wMEM in the context of localising epileptic sources from EEG data (Lina *et al.* 2014). The present study has adopted the wMEM method to investigate inter-subject associative channels for improving subject independent BCI performance. It demonstrates that selecting inter-subject associative channels could be used to supplement transfer learning across subjects.

3.3.4 Study significance and limitation

Subject-to-subject and session-to-session transferability of trained model parameters is inevitably critical for the generalisation of a BCI system (Jayaram *et al.* 2016). In supervised machine learning-based applications, a principal assumption is that the training and test data follow similar distributions. This assumption often fails and, consequently, covariate shift occurs (Pan and Yang 2010). Covariate shift adaptation has been a key strategy to compensate inter-subject and inter-session variability in BCI (Sugiyama *et al.* 2007). However, this study aims at investigating inter-subject associativity in cross-subject BCI paradigm (Saha *et al.* 2017b, Saha *et al.* 2017a). The aim is to evaluate if there are similarities between two subjects' neural substrates quantified by wMEM-based inter-subject cortical source localisation for MI tasks. Exploiting inter-subject associativity, i.e., leveraging source space related neuroscience priors, may augment transfer learning (Wronkiewicz *et al.* 2015) and reduce/eliminate the calibration effort for BCI. The advantage of this cross-subject paradigm over pooled-subject paradigm is that it directly investigates associativity of any two subjects' brain dynamics in source space. This study suggests that WMEM selection of EEG channels could advance this goal beyond the reduction in computational cost due to fewer analysed channels because it has been hypothesized that the selected channels manifest the inter-subject associative sensorimotor dynamics in source space.

It is to be noted that our results do not indicate a common trend of BCI prediction performance for all subject pairs. Our goal was to identify pairs of subjects sharing common sensorimotor dynamics. Thus, achieving poor BCI prediction performance for any subject pair might manifest dissimilar MI-related dynamics between subjects (Saha *et al.* 2017b, Saha *et al.* 2017a). On the other hand, it might not be improbable to achieve good prediction performance for a subject pair only, assuming both subjects share common sensorimotor dynamics related to right hand and right foot MI. Further

studies would be necessary to explore the role of wMEM-based cortical source estimation in subject pairs showing poor classification performance. This study is limited by using data from a few subjects with no individual information on head/brain anatomy.

Another key limitation of this study is the manual selection of EEG channels by visually inspecting the MI-related source activation projected on the 3D head geometry. To the best of my knowledge, this study is the first attempt to investigate the role of any source localisation method on inter-subject EEG signals in the BCI context to evaluate inter-subject associativity. Future studies should aim at extracting optimal channels automatically, by imposing selection criteria in the 3D head model geometry source space.

3.4 Conclusion

Brain dynamics reflected on RSN are complex and variable across individuals and, thus, compensating inter-subject diversity is important for calibration-free BCI. In this chapter, I have demonstrated that wMEM could be used to identify inter-subject associative sources within the cortico-subcortical networks, which allow selecting optimal EEG channels for classifying subject independent MI tasks. The improved prediction performance utilising fewer, optimal EEG channels result in enhanced inter-subject coherence and suggest the suitability of wMEM for assessing inter-subject associative sensorimotor oscillations.

Table 3.2. Single trial motor imagery prediction performances.

	CSP		RCSP	
Subject	Case I	Case II	Case I	Case II
Pair	Mean±SD	Mean±SD	Mean±SD	Mean±SD
aa-al	51.79±14.70	64.64±14.33	73.21±9.71	76.79±9.11
aa-av	54.64±10.25	55.71±7.38	66.79±6.53	66.07±10.00
aa-aw	55.36±10.28	62.86±11.93	68.93±10.92	72.86±7.93
aa-ay	53.93±12.76	58.93±17.11	75.00±8.58	72.14±13.24
al-av	53.93±6.40	51.07±4.47	68.21±6.40	65.71±7.75
al-aw	62.50±7.39	53.93±11.22	72.50±11.91	71.79±10.44
al-ay	73.57±13.38	71.78±11.47	83.21±12.26	84.64±13.15
av-aw	49.29±8.55	53.93±14.43	70.36±6.74	68.57±9.34
av-ay	62.50±10.81	62.86±11.81	72.50±10.39	71.79±8.49
aw-ay	47.50±10.39	53.21±11.84	66.79±7.54	70.00±9.25
al-aa	56.79±10.97	58.93±11.82	72.50±5.84	70.71±13.55
av-aa	52.14±13.70	52.50±5.84	67.14±9.34	64.29±7.14
aw-aa	56.07±9.68	56.43±13.86	64.64±7.23	63.21±8.43
ay-aa	57.86±9.49	56.07±10.11	69.29±6.56	70.36±11.05
av-al	46.07±8.82	55.36±12.17	71.79±7.80	71.79±9.74
aw-al	63.93±14.72	68.21±20.86	69.64±12.05	75.71±15.50
ay-al	63.21±20.55	77.14±14.40	86.07±10.71	**90.36±5.59**
aw-av	54.29±11.88	55.36±5.89	66.43±5.38	65.71±4.52
ay-av	53.93±8.82	54.29±5.53	68.93±8.08	66.07±4.84
ay-aw	50.36±10.02	55.71±5.11	70.00±6.12	69.64±5.39
Mean(Mean)±SD(Mean)	55.98±6.53	58.95±6.90	71.20±5.32	71.41±6.65

(CSP: Common Spatial Pattern, RCSP: Regularised Common Spatial Pattern, Case I: all channels, Case II: selected channels)

Chapter 4

Intracardiac Electrogram Measurement Uncertainty

MAPPING of clinical atrial fibrillation (AF) remains challenging. Several characteristics of the local atrial bipolar electrograms (EGM) are clinically used to guide ablation and include peak-to-peak voltage (Vpp), dominant frequency (DF) and Shannon entropy (ShEn). The effect of bipolar vector orientation and inter-electrode spacing on these EGM-derived measures during AF is unclear. To quantify the impact of bipolar vector orientation and inter-electrode spacing, bipolar EGM (23,589 and 20,968 atrial recording sites, respectively) were reconstructed from unipolar EGM recorded with an array of 18 electrodes (HD Grid, Abbott Medical) in 14 patients with persistent AF. We compared Vpp, DF and ShEn between two diagonally orthogonal bipolar vectors representing a common recording site during AF characterisation. Vpp, DF and ShEn values were categorised as 'high' and 'low' value. To quantify the effect of inter-electrode spacing, bipolar EGM were constructed from electrodes spaced $4mm$, $8mm$, and $12mm$ apart, respectively. Bipolar vector orientation and inter-electrode spacing both significantly affect bipolar EGM-derived measures that may result in significant uncertainty around the electroanatomical substrate characterisation in AF patients. These factors require consideration in developing and evaluating newer tools and in the interpretation of EGM during clinical mapping.

4.1 Introduction

Atrial fibrillation (AF) is the most common arrhythmia in humans, which occurs due to the presence of irregular and disorganised electrical activities (Lip *et al.* 2016, Nattel 2002). The underlying causes of AF include structural remodeling of the arrhythmogenic substrates that potentially disrupt the regular cardiac conduction dynamics in sinus rhythm (Lau *et al.* 2017). Intracardiac catheter ablation is a widely used clinical procedure to terminate AF-related atrial electrical sources and to restore sinus rhythm. As a predecessor step of any catheter ablation (CA), intracardiac eletrograms (EGM) are recorded using catheter-based electrodes to select ablation targets. Usually, bipolar EGM are constructed from unipolar EGM to quantify the arrythmogenic substrates, because bipolar EGM are less prone to be contaminated by far-field potentials, i.e., ventricular artefacts. However, bipolar EGM are heavily dependent on bipolar vector orientation and inter-electrode spacing, which has been discussed in this chapter.

Peak-to-peak voltage (Vpp) of local bipolar EGM are used to quantify areas of low voltage (Thanigaimani *et al.* 2017). Low voltage areas (Vpp$< 0.5mV$) have been used as an indication of structural change, diseased myocardium and electrical scar (Baumert *et al.* 2016b, Burstein and Nattel 2008, Dimitri *et al.* 2012, John *et al.* 2010, Oakes *et al.* 2009, Rolf *et al.* 2014, Sanders *et al.* 2003, Schreiber *et al.* 2017, Stiles *et al.* 2009, Verma *et al.* 2005). Additional bipolar EGM-derived measures such as dominant frequency (DF) and Shannon entropy (ShEn) have been clinically used to examine the propagation of predominant waves and to detect the pivot of a rotor, respectively, which may help to guide substrate-based ablation (Atienza *et al.* 2009, Ganesan *et al.* 2013, Sanders *et al.* 2005).

Bipolar EGM are less prone to far-field potentials but are naturally dependent on bipolar vector orientation and inter-electrode spacing (Anter and Josephson 2016), which is not sufficiently incorporated in the design of many clinically-used mapping catheters or software algorithms. Particularly during AF, where the coordinated activation of the atrium is replaced by a complex and multidirectional activation pattern, the impact of vector orientation and inter-electrode distance on bipolar EGM-derived measures is difficult to predict.

This study aims to quantify the effect of bipolar vector orientation and inter-electrode spacing on Vpp, DF and ShEn derived from bipolar EGM recordings in patients with persistent AF using a novel 18 unipolar electrodes grid catheter.

4.2 Methods

4.2.1 Study population

This is an ancillary study of a prospective, multicentre clinical study for evaluating the use of HD-Grid catheter in humans (EnSite^{TM} HD Grid Catheter AF/AT Mapping Study; $NCT02656537$). All recordings were obtained at the Royal Adelaide Hospital from 14 patients with symptomatic drug-refractory persistent AF, before they underwent catheter ablation. All patients provided written informed consent to participate in the study. The protocol was approved by the Ethics Committee of the Royal Adelaide Hospital ($HREC/15/RAH/344$).

Baseline patient characteristics are provided in Table 4.1. The inclusion criteria were presence of non-paroxysmal AF referred for catheter ablation, an age of 18 years or older at the time of enrollment, continuous anticoagulation (INR $2-3$) for >4 weeks prior to the ablation. Exclusion criteria included secondary AF, presence of a prosthetic valve(s) or hemodynamically significant valvular heart disease as determined by the study investigator, active systemic infection, presence of left atrial thrombus or myxoma, or interatrial baffle or patch via the transseptal approach, contraindication to systemic anticoagulation, a history of cerebrovascular accidents, previous myocardial infarction, unstable angina pectoris or coronary artery by-pass, left atrial size $>55mm$, a NYHA functional class III or IV, left ventricular ejection fraction $<35\%$.

4.2.2 Electrophysiology study

All patients were studied in the fasted state under general anesthesia. Procedures were undertaken on uninterrupted oral anticoagulation. All patients who were not utilising Amiodarone stopped anti-arrhythmic medications for 5 days prior to the procedure. Prior to the insertion of catheters, all patients underwent trans-esophageal examination to exclude the presence of left atrial thrombus. Femoral venous access was obtained using ultrasound guidance.

A 10 pole catheter ($2-5-2mm$ spacing, Abbott Medical) was positioned in the coronary sinus with the proximal pole at the coronary sinus ostium in best septal left anterior oblique projection. A SLO sheath was used with a BRK1 needle (Abbott Medical) to undertake a TEE-guided transseptal puncture. The one transseptal puncture was used to introduce a D/F Flexibility externally-irrigated ablation catheter (Abbott

Table 4.1. Baseline patient characteristics ($n = 14$).

Demographics	
Age, year	65.3 ± 6.4
Male gender, $n(\%)$	$10(71.4)$
Weight, kg	98.9 ± 12.2
Height, cm	178.1 ± 6.6
Body Mass Index	31.4 ± 5.3
AF-specific	
Persistent AF, $n(\%)$	$14(100)$
Electrical Cardioversion, n	8
CHA2DS2-VASc	$2(1,3)$
Anticoagulation, $n(\%)$	$14(100)$
Riskfactors	
Sleep apnea, $n(\%)$	$3(21.4)$
Hypertension, $n(\%)$	$10(71.4)$
Hyperlipidemia, $n(\%)$	$2(14.3)$
Diabetes, $n(\%)$	$2(14.3)$
Medication	
Flecainide, $n(\%)$	$3(21.4)$
Sotalol, $n(\%)$	$3(21.4)$
Amiodarone, $n(\%)$	$1(7.1)$
L-type CCB, $n(\%)$	$4(28.6)$
ACEI/ARB, $n(\%)$	$12(85.7)$
Beta-blockers, $n(\%)$	$6(42.9)$
Echocardiography	
LA diameter, cm	4.5 ± 0.6
LA area, cm^2	28.1 ± 4.5
LA volume, cm^3	99.7 ± 24.8
LV ejection fraction , %	55 ± 6.1
LV interventricular septum, cm	$1.1(1, 1.2)$

(Values are presented as mean±SD, median (interquartile range) or n (%). LV: left ventricle. LA: left atrium. CCB: calcium channel blockers. ACEI/ARB: ACE inhibitors/ Angiotensin receptor blockers.)

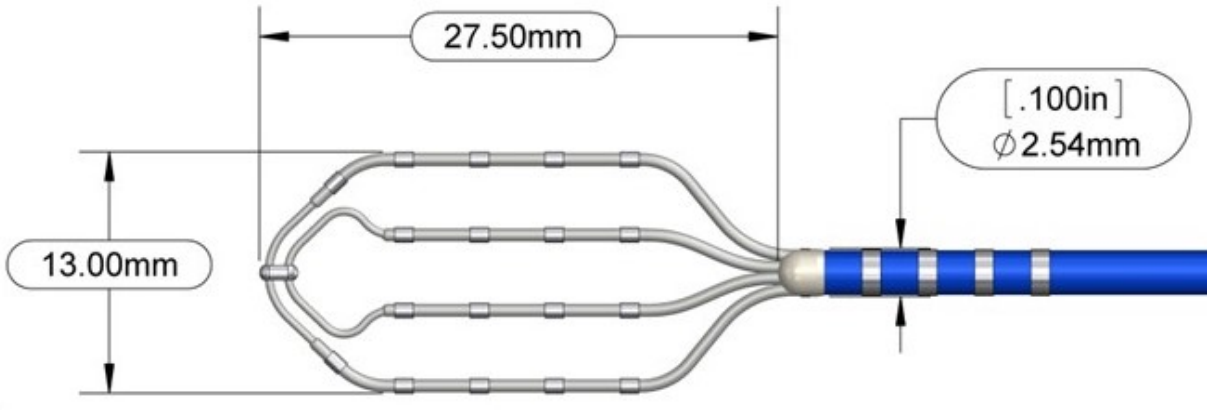

Figure 4.1. HD grid catheter used to collect atrial EGM.

Medical) through an Agilis sheath (Abbott Medical). The HD Grid catheter (Abbott Medical) was introduced through the SLO sheath. Repeated boluses of heparin was used to maintain the ACT $>$ 350 seconds for the duration of the study.

4.2.3 HD-Grid catheter

The high-density grid catheter (EnSite^{TM} HD Grid Catheter, Abbott Medical) with an 18 unipolar electrodes grid within $357mm^2$ surface area was used to collect local atrial EGM (Figure 4.1; (Bellmann *et al.* 2018)). The unipolar electrodes are aligned in four parallel struts and the spacing between two adjacent struts is $4mm(\pm 0.5mm)$. The centre-to-centre distance between two adjacent electrodes along a strut is $4mm(\pm 0.5mm)$. The inter-electrode spacing (centre-to-centre) is $4mm$ for any two adjacent electrodes along or across the strut. The length of each electrode is $1mm$ with an outer diameter of $0.81mm$. The HD grid catheter is made of nickel-titanium alloy (Nitinol). Nitinol is characterised especially by its shape memory and superelasticity. The deformation of catheter under pressure is negligible and as a result, the spacing between electrodes remain same throughout the mapping.

4.2.4 Mapping protocol

Electroanatomic maps were created using two versions of NAVX systems, i.e., Velocity V4.2/V5.0.1 (commercial) and Velocity Research Software (Abbott Medical). Patients were mapped during AF. If patients presented to the laboratory in sinus rhythm, AF was induced by burst pacing and mapping commenced only after AF had been sustained for $\geq$ 10 minutes. Detailed left atrial geometry was initially created. Following

this electrophysiological parameters were collected. At each map site, the catheter was held stationary for 8 seconds, after fluoroscopic contact verification before the point was collected. EGM were recorded for 3 seconds. Mapping sites were evenly distributed to cover the entire left atrium. Recordings were acquired at $2034.5Hz$ and preprocessed using a notch filter ($50Hz$) and a band-pass filter ($30 - 300Hz$) to eliminate the power-line interference and to extract clinically important band of the signal with locations annotated on NAVX system. In order to reduce selection bias, we did not exclude scar areas or areas with marked EGM fractionation handled, as these EGM characteristics could also depend on inter-electrode spacing or bipolar vector orientation. Following mapping, ablation was undertaken in accordance with the operator's preference and constituted pulmonary vein or posterior wall isolation in all and additional ablation based on available online EGM characteristics.

4.2.5 Study protocol

To quantify the impact of bipolar vector orientation on EGM during AF, two EGM with diagonally orthogonal bipolar vectors were constructed for each atrial recording site. Figure 4.2 illustrates the orientations of the two bipolar vectors around a common centre. Reflecting the geometry and dimensions of the HD-Grid catheter, the bipolar inter-electrode spacing was $5.65mm$ and the angular distance between two bipolar vector orientations was $90°$. To quantify the bipolar EGM characteristics across two diagonally orthogonal orientations, Vpp, DF and ShEn values were computed as described in the section EGM processing. Finally, EGM-derived features were classified according to 'high' and 'low' values for statistical inference.

To assess the effect of inter-electrode spacing on bipolar EGM, vectors were derived for electrodes spaced at $4mm$, $8mm$, and $12mm$ apart, respectively. One unipolar electrode was kept common while constructing EGM signals along or across the strut (i.e., the same bipolar vector for each set of three EGM). Figure 4.3 shows three bipolar EGM constructed along a bipolar vector corresponding to the inter-electrode spacing of $4mm$, $8mm$, and $12mm$, respectively.

Each shot captures 18 unipolar EGM simultaneously. A total of 2621 shots were recorded from 14 patients (187.21 ± 68.17 shots/patient). Notably, only 16 electrodes were used for a single shot to construct two sets of nine diagonally orthogonal bipolar vectors.

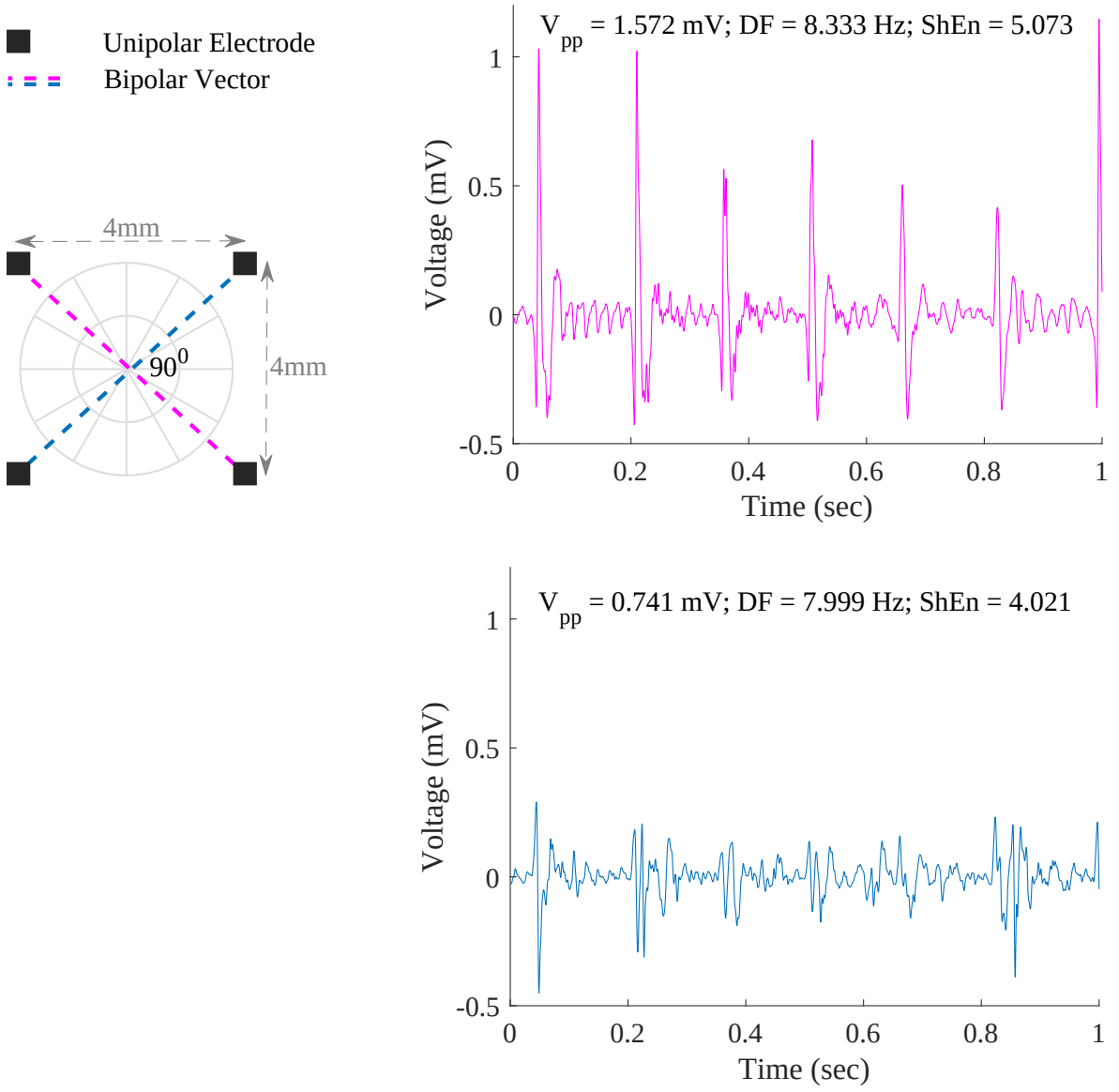

Figure 4.2. Examples of EGM constructed for two diagonally orthogonal bipolar vector orientations around a common centre. The angle between the two bipolar vectors is 90°. EGM and corresponding measures differ due to bipolar vector orientation.

Therefore, a total of 23,589 and 20,968 atrial sites were assessed to investigate the impact of bipolar vector orientation and inter-electrode spacing, respectively.

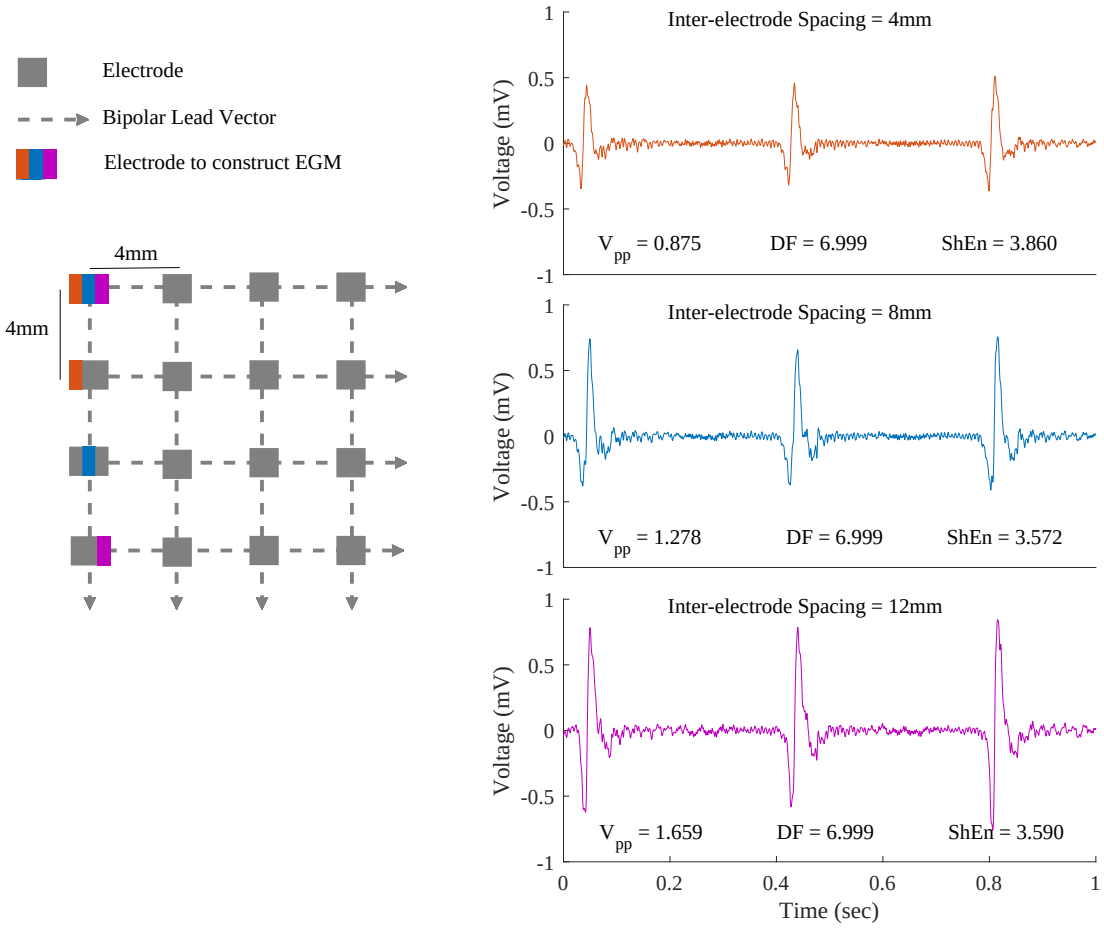

Figure 4.3. Examples of constructed bipolar EGM with an inter-electrode spacing of $4mm$, $8mm$, and $12mm$, respectively, while keeping a common reference unipolar electrode. EGM and corresponding measures differ due to diverse inter-electrode spacing.

4.2.6 EGM processing

Bipolar EGM-derived measures, i.e., Vpp, DF and ShEn have potential in clinical ablation and are being undertaken as previously described in various studies (Atienza *et al.* 2009, Ganesan *et al.* 2013, Sanders *et al.* 2005, Takigawa *et al.* 2018).

Peak-to-peak voltage (Vpp): Vpp was calculated as the difference between maximum and minimum value within EGM.

Dominant frequency (DF): DF estimation involves filtering EGM using the nonlinear method proposed by Botteron and Smith (Botteron and Smith 1995). First, EGM were filtered using a band-pass filter with corner frequencies of $30Hz$ and $300Hz$, followed by rectification and filtering using a secondary band-pass filter with corner frequencies of $3Hz$ and $15Hz$ (Baumert *et al.* 2016b, Sanders *et al.* 2005). DF was estimated as

the frequency corresponding to the peak of the power spectrum density derived by an 8192-point fast Fourier transform. To reduce the effect of spectral leakage, edge tapering was performed by a Hanning window. The regularity index (RI) was then estimated as a marker of DF detection reliability, defined as the ratio between the power at DF and its adjacent frequencies ($\approx 0.75Hz$ bandwidth).

Shannon entropy (ShEn): Assuming $p_1, p_2, \ldots\ldots\ldots, p_N$ are the discrete probabilities (bins) of an EGM time series, then ShEn is defined as (Shannon 1948):

$$ShEn = -\sum_{i=1}^{N} p_i \log_2 p_i \tag{4.1}$$

The number of bins was set to $N = 100$ (Ganesan *et al.* 2014).

4.2.7 Statistical analysis

To evaluate the effects of bipolar vector orientation and inter-electrode spacing on EGM measures, either of the analysis of variance (ANOVA) or the Kruskal-Wallis test was conducted for normal and non-normal distributed variables, respectively. The Lilliefors test was performed to test variables for Gaussianity. For post-hoc analysis, the Tukey-Kramer method was applied. Results are presented as mean±SD (SD: standard deviation). P-values < 0.01 were considered statistically significant.

4.3 Results

4.3.1 Patient characteristics

Patient characteristics are summarised in Table 4.1. All 14 patients (mean age 65.3 ± 6.4 year, 10 males, weight $98.9 \pm 12.2kg$, height $178.1 \pm 6.6cm$ and body mass index 31.4 ± 5.3) had persistent AF and eight patients underwent electrical cardioversion. The median (interquartile range) of CHA2DS2-VASc score was $2(1,3)$ and all 14 patients were taking anticoagulants. A proportion of patients were receiving antiarrhythmic medications (i.e., Flecainide (3/14), Sotalol (3/14), Phenylalkylamines (4/14), Amiodarone (1/14), Beta-blocker (6/14)). The average left ventricular ejection fraction was $55 \pm 6.1\%$. Left atrial volume was $99.7 \pm 24.9cm^3$ (left atrial area $28.1 \pm 4.5cm^2$ and left atrial diameter $4.5 \pm 0.6cm$). The AF cycle length was $203.9 \pm 31.1ms$ estimated from coronary sinus EGM.

Table 4.2. Summary of extracted measures using two diagonally orthogonal bipolar vector orientations.

Measure	high value	low value	p-value
	Mean±SD	Mean±SD	
Vpp	1.023 ± 1.714	0.691 ± 0.855	1.10^{-155}
DF	7.873 ± 2.595	6.707 ± 1.487	0.00
RI	0.246 ± 0.068	0.209 ± 0.063	0.00
ShEn	4.646 ± 0.607	4.251 ± 0.684	0.00

(Vpp: peak-to-peak voltage, DF: dominant frequency, RI: regularity index and ShEn: Shannon entropy.)

4.3.2 Effect of bipolar vector orientation on EGM-derived measures

A total of 23,589 atrial sites were assessed to investigate the impact of bipolar vector orientation on EGM-derived measures. Table 4.2 shows EGM-derived Vpp, DF and ShEn measures using two diagonally orthogonal bipolar vector orientations. The number of constructed bipolar EGM signals collected from 14 patients for each class (high or low value) was 23,589. All measures are significantly different between 'high' and 'low' groups ($p < 0.01$). Patient-specific statistics are included in Tables 4.3-4.5.

4.3.3 Effect of inter-electrode spacing on measures derived from bipolar EGM

From 14 AF patients, a total 20,968 bipolar EGM have been constructed to investigate the effect of inter-electrode spacing. Table 4.6 shows the EGM measures corresponding to the inter-electrode spacing of $4mm$, $8mm$, and $12mm$, respectively. All three measures were significantly affected by inter-electrode spacing ($p < 0.01$). For example, the Vpp value increased from $0.854 \pm 1.299mV$ to $0.958 \pm 1.483mV$ and $1.013 \pm 1.302mV$ for $4mm$, $8mm$, and $12mm$, respectively. Post-hoc comparisons (Tukey-Kramer method) were all significant except for DF and RI values between $8mm$ and $12mm$, respectively. Detailed patient-specific statistics are shown in Tables 4.7-4.9.

Table 4.3. Patient-specific summary of Vpp using two diagonally orthogonal bipolar vector orientations.

Measure	high value	low value	p-value	N
	Mean±SD	Mean±SD		
Vpp	0.731 ± 0.887	0.497 ± 0.634	3.92^{-13}	1161
	0.559 ± 0.794	0.387 ± 0.557	3.27^{-15}	1269
	0.506 ± 0.726	0.331 ± 0.408	3.08^{-10}	846
	0.554 ± 0.508	0.379 ± 0.330	1.26^{-27}	1314
	0.668 ± 3.356	0.269 ± 0.478	1.19^{-04}	864
	1.454 ± 1.354	1.060 ± 0.962	1.45^{-20}	1350
	0.895 ± 0.686	0.632 ± 0.482	8.15^{-34}	1539
	1.934 ± 1.399	1.432 ± 1.043	4.70^{-27}	1431
	1.377 ± 3.168	0.869 ± 0.879	6.23^{-12}	1998
	0.573 ± 0.741	0.379 ± 0.491	1.57^{-23}	2124
	2.238 ± 2.129	1.564 ± 1.510	1.56^{-32}	2151
	0.662 ± 0.718	0.466 ± 0.469	1.46^{-29}	2475
	0.554 ± 0.828	0.371 ± 0.528	9.95^{-23}	2817
	0.994 ± 1.848	0.590 ± 0.516	3.06^{-23}	2250

(Vpp: peak-to-peak voltage and N is number of bipolar electrogram signals for each class.)

4.3.4 Quantification of threshold-based substrate characterisation

For all EGM-derived measures (Vpp, DF and ShEn), five thresholds were defined based on each measure's distribution (10th, 20th, 30th and 40th percentile and the median value), because no established thresholds exist for DF and ShEn. In the case of Vpp, the previously used threshold for low voltage areas (Vpp$< 0.5mV$) was included.

Figure 4.4 shows the comparison of Vpp, DF and ShEn values derived using diagonally orthogonal bipolar vector orientations, i.e., two bipolar vectors placed at 90° with an inter-electrode spacing $5.65mm$. For example, the percentage of atrial sites below low voltage threshold (Vpp$< 0.5mV$) differed across bipolar vector orientations, i.e., 58.45% and 47.34% for 'high' and 'low' groups, respectively.

Figure 4.5 illustrates the variability in Vpp, DF and ShEn values due to the difference in inter-electrode spacing, i.e., $4mm$, $8mm$, and $12mm$. The percentage of atrial sites

Table 4.4. Patient-specific summary of DF and RI using two diagonally orthogonal bipolar vector orientations.

Measure	high value	low value	p-value	N
	Mean±SD	Mean±SD		
DF	7.350 ± 2.141	6.442 ± 1.047	$3.01 - 37$	1161
	5.525 ± 3.927	4.519 ± 3.032	2.04^{-46}	1269
	8.961 ± 3.057	7.775 ± 2.147	2.74^{-34}	846
	6.722 ± 2.786	5.682 ± 1.653	8.28^{-48}	1314
	6.087 ± 3.978	4.851 ± 2.715	4.79^{-38}	864
	7.988 ± 2.865	7.309 ± 2.119	1.06^{-30}	1350
	7.305 ± 2.461	6.149 ± 1.213	7.81^{-59}	1539
	6.835 ± 1.974	6.062 ± 0.987	6.63^{-39}	1431
	8.995 ± 2.643	7.916 ± 1.543	2.35^{-54}	1998
	7.399 ± 2.653	6.274 ± 1.291	8.66^{-67}	2124
	8.235 ± 2.530	7.208 ± 1.407	4.48^{-59}	2151
	7.782 ± 2.677	6.384 ± 1.472	3.98^{-109}	2475
	8.103 ± 2.728	6.582 ± 1.332	7.74^{-147}	2817
	8.081 ± 2.293	6.954 ± 1.084	4.86^{-94}	2250
RI	0.262 ± 0.076	0.225 ± 0.071	3.86^{-32}	1161
	0.171 ± 0.108	0.148 ± 0.095	1.51^{-45}	1269
	0.261 ± 0.104	0.212 ± 0.089	3.66^{-33}	846
	0.231 ± 0.076	0.195 ± 0.068	1.63^{-62}	1314
	0.193 ± 0.109	0.161 ± 0.094	9.05^{-36}	864
	0.276 ± 0.105	0.235 ± 0.095	8.06^{-47}	1350
	0.217 ± 0.043	0.184 ± 0.040	1.12^{-98}	1539
	0.250 ± 0.052	0.215 ± 0.050	2.70^{-71}	1431
	0.272 ± 0.080	0.229 ± 0.071	1.04^{-70}	1998
	0.261 ± 0.079	0.224 ± 0.075	2.78^{-54}	2124
	0.258 ± 0.067	0.220 ± 0.063	1.06^{-82}	2151
	0.221 ± 0.053	0.187 ± 0.048	4.88^{-117}	2475
	0.227 ± 0.057	0.191 ± 0.052	9.53^{-127}	2817
	0.237 ± 0.055	0.199 ± 0.049	5.55^{-118}	2250

(DF: dominant frequency, RI: regularity index and N is number of bipolar electrogram signals for each class.)

Table 4.5. Patient-specific summary of ShEn using two diagonally orthogonal bipolar vector orientations.

Measure	high value	low value	p-value	N
	Mean±SD	Mean±SD		
ShEn	4.595 ± 0.623	4.188 ± 0.680	1.21^{-48}	1161
	3.420 ± 2.022	3.148 ± 1.881	2.47^{-47}	1269
	4.690 ± 1.117	4.319 ± 1.119	8.00^{-35}	846
	4.539 ± 1.120	4.172 ± 1.093	5.36^{-63}	1314
	3.950 ± 1.967	3.600 ± 1.850	2.63^{-38}	864
	4.200 ± 1.208	3.872 ± 1.151	3.92^{-52}	1350
	4.515 ± 0.551	4.122 ± 0.600	1.15^{-75}	1539
	4.341 ± 0.509	3.991 ± 0.545	4.98^{-67}	1431
	4.663 ± 0.515	4.289 ± 0.616	1.46^{-91}	1998
	4.642 ± 0.674	4.222 ± 0.739	4.07^{-80}	2124
	4.595 ± 0.705	4.194 ± 0.762	2.33^{-69}	2151
	4.838 ± 0.600	4.456 ± 0.682	7.21^{-93}	2475
	4.732 ± 0.586	4.327 ± 0.697	1.83^{-117}	2817
	4.594 ± 0.565	4.141 ± 0.684	5.98^{-122}	2250

(ShEn: Shannon entropy and N is number of bipolar electrogram signals for each class.)

Table 4.6. Summary of extracted EGM measures using an inter-electrode spacing of $4mm$, $8mm$, and $12mm$ obtained along a common bipolar vector orientation.

Measure	4mm	8mm	12mm	p-value
	Mean±SD	Mean±SD	Mean±SD	
Vpp	0.854 ± 1.299	0.958 ± 1.483	1.013 ± 1.302	1.82^{-32}
DF*	7.316 ± 2.239	7.238 ± 2.140	7.234 ± 2.124	6.31^{-05}
RI*	0.226 ± 0.068	0.231 ± 0.069	0.231 ± 0.069	4.20^{-14}
ShEn	4.364 ± 0.714	4.481 ± 0.647	4.514 ± 0.624	9.09^{-129}

($*$ indicates measures that were not significantly different between $8mm$ and $12mm$; All other measures are significantly different amongst classes)

Table 4.7. Patient-specific summary of Vpp using an inter-electrode spacing of $4mm$, $8mm$, and $12mm$.

Measure	4mm	8mm	12mm	p-value	post hoc analysis	N
	Mean±SD	Mean±SD	Mean±SD			
Vpp	0.576 ± 0.679	0.686 ± 0.870	0.762 ± 0.968	4.02^{-06}	$*\#$	1032
	0.654 ± 0.795	0.756 ± 0.822	0.795 ± 0.787	8.44^{-05}	$*\#$	1128
	0.480 ± 0.755	0.536 ± 0.748	0.603 ± 0.790	7.54^{-03}	$\#$	752
	0.514 ± 0.525	0.565 ± 0.520	0.631 ± 0.547	5.90^{-07}	$*\#\wedge$	1168
	0.638 ± 2.981	0.598 ± 2.400	0.589 ± 1.923	9.18^{-01}		768
	1.269 ± 1.308	1.420 ± 1.247	1.584 ± 1.344	2.24^{-08}	$*\#\wedge$	1200
	0.783 ± 0.646	0.829 ± 0.583	0.851 ± 0.548	8.79^{-03}	$\#$	1368
	1.65 ± 1.25	1.79 ± 1.22	1.89 ± 1.20	4.68^{-06}	$*\#$	1272
	1.188 ± 1.174	1.335 ± 2.471	1.273 ± 1.112	3.49^{-02}	$*$	1776
	0.482 ± 0.733	0.550 ± 0.704	0.621 ± 0.733	2.70^{-08}	$*\#\wedge$	1888
	1.879 ± 2.050	2.124 ± 2.246	2.175 ± 2.214	4.04^{-05}	$*\#$	1912
	0.595 ± 0.726	0.646 ± 0.716	0.672 ± 0.673	9.94^{-04}	$*\#$	2200
	0.440 ± 0.634	0.492 ± 0.669	0.541 ± 0.926	1.38^{-05}	$*\#$	2504
	0.716 ± 1.393	0.893 ± 1.722	1.017 ± 1.482	4.69^{-09}	$*\#\wedge$	2000

(Vpp: peak-to-peak voltage, N is number of bipolar electrogram signals for each class, $*$ means 4mm and 8mm groups are significantly different from each other, # means $4mm$ and $12mm$ groups are significantly different from each other and $\wedge$ means $8mm$ and $12mm$ groups are significantly different from each other.)

differed when Vpp$< 0.5mV$, i.e., 53.77%, 46.85% and 42.03%, respectively for $4mm$, $8mm$ and $12mm$.

Figure 4.6 compares left atrial maps reconstructed for Vpp (Figure 4.6A), DF (Figure 4.6B) and ShEn (Figure 4.6C) for 'high' and 'low' values obtained from diagonally orthogonal bipolar vector orientations (inter-electrode spacing $=$ $5.65mm$) (for quantification please refer to Figure 4.4).

4.4 Discussion

Table 4.8. Patient-specific summary of DF and RI using an inter-electrode spacing of $4mm$, $8mm$, and $12mm$.

Measure	4mm	8mm	12mm	p-value	post hoc analysis	N
	Mean±SD	Mean±SD	Mean±SD			
DF	6.942 ± 1.993	6.813 ± 1.598	6.876 ± 1.798	0.266		1032
	6.725 ± 2.485	6.625 ± 2.560	6.546 ± 2.549	0.244		1128
	8.798 ± 2.221	8.830 ± 2.196	8.705 ± 2.090	0.512		752
	6.541 ± 1.945	6.422 ± 1.845	6.476 ± 1.864	0.317		1168
	6.557 ± 2.302	6.519 ± 2.361	6.509 ± 2.175	0.908		768
	8.182 ± 1.748	8.149 ± 1.717	8.190 ± 1.712	0.827		1200
	6.767 ± 2.069	6.672 ± 1.873	6.682 ± 1.928	0.380		1368
	6.52 ± 1.68	6.55 ± 1.76	6.51 ± 1.69	0.794		1272
	8.376 ± 2.038	8.386 ± 2.084	8.438 ± 2.174	0.642		1776
	6.934 ± 2.256	6.764 ± 2.051	6.696 ± 2.011	0.002	$*$#	1888
	7.824 ± 2.267	7.706 ± 2.096	7.799 ± 2.218	0.215		1912
	7.164 ± 2.417	6.970 ± 2.094	6.973 ± 2.089	0.004	$*$#	2200
	7.307 ± 2.233	7.271 ± 2.145	7.228 ± 2.017	0.244		2504
	7.472 ± 2.014	7.446 ± 1.904	7.417 ± 1.729	0.657		2000
RI	0.241 ± 0.070	0.249 ± 0.075	0.246 ± 0.076	0.046	$*$	1032
	0.210 ± 0.052	0.218 ± 0.056	0.218 ± 0.057	0.001	$*$#	1128
	0.241 ± 0.088	0.252 ± 0.093	0.258 ± 0.092	0.001	$*$#	752
	0.223 ± 0.060	0.226 ± 0.061	0.226 ± 0.059	0.365		1168
	0.219 ± 0.066	0.224 ± 0.068	0.227 ± 0.069	0.069		768
	0.270 ± 0.082	0.271 ± 0.079	0.272 ± 0.080	0.780		1200
	0.200 ± 0.045	0.202 ± 0.046	0.202 ± 0.044	0.414		1368
	0.23 ± 0.05	0.23 ± 0.05	0.23 ± 0.05	0.526		1272
	0.256 ± 0.080	0.254 ± 0.078	0.253 ± 0.078	0.564		1776
	0.236 ± 0.078	0.250 ± 0.081	0.254 ± 0.083	0.000	$*$#	1888
	0.238 ± 0.068	0.243 ± 0.070	0.241 ± 0.067	0.067	1912	
	0.205 ± 0.055	0.209 ± 0.056	0.210 ± 0.053	0.007	$*$#	2200
	0.208 ± 0.060	0.211 ± 0.059	0.212 ± 0.058	0.025	#	2504
	0.215 ± 0.057	0.218 ± 0.055	0.216 ± 0.053	0.159		2000

(DF: dominant frequency, RI: regularity index, N is number of bipolar electrogram signals for each class, $*$ means $4mm$ and $8mm$ groups are significantly different from each other and # means $4mm$ and $12mm$ groups are significantly different from each other.)

Table 4.9. Patient-specific summary of ShEn using an inter-electrode spacing of $4mm$, $8mm$, and $12mm$.

Measure	4mm	8mm	12mm	p-value	post hoc analysis	N
	Mean±SD	Mean±SD	Mean±SD			
ShEn	4.295 ± 0.679	4.415 ± 0.662	4.445 ± 0.665	5.67^{-07}	$*\#$	1032
	4.257 ± 0.680	4.338 ± 0.622	4.402 ± 0.607	4.68^{-07}	$*\#\wedge$	1128
	4.624 ± 0.733	4.710 ± 0.668	4.727 ± 0.663	7.62^{-03}	$*\#$	752
	4.463 ± 0.654	4.582 ± 0.577	4.587 ± 0.554	1.02^{-07}	$*\#$	1168
	4.546 ± 0.729	4.625 ± 0.690	4.643 ± 0.661	1.57^{-02}	$\#$	768
	4.215 ± 0.674	4.375 ± 0.591	4.389 ± 0.564	1.56^{-12}	$*\#$	1200
	4.238 ± 0.615	4.321 ± 0.560	4.358 ± 0.510	1.44^{-28}	$*\#$	1368
	4.08 ± 0.57	4.26 ± 0.51	4.31 ± 0.51	6.89^{-40}	$*\#\wedge$	1272
	4.297 ± 0.604	4.484 ± 0.576	4.547 ± 0.534	7.56^{-40}	$*\#\wedge$	1776
	4.382 ± 0.808	4.463 ± 0.700	4.486 ± 0.667	2.15^{-05}	$*\#$	1888
	4.281 ± 0.793	4.429 ± 0.730	4.478 ± 0.709	1.94^{-16}	$*\#$	1912
	4.557 ± 0.709	4.652 ± 0.650	4.684 ± 0.606	2.17^{-10}	$*\#$	2200
	4.445 ± 0.703	4.559 ± 0.654	4.593 ± 0.646	1.25^{-14}	$*\#$	2504
	4.385 ± 0.743	4.479 ± 0.633	4.491 ± 0.616	2.89^{-07}	$*\#$	2000

(ShEn: Shannon entropy, N is number of bipolar electrogram signals for each class, $*$ means $4mm$ and $8mm$ groups are significantly different from each other, # means $4mm$ and $12mm$ groups are significantly different from each other and $\wedge$ means $8mm$ and $12mm$ groups are significantly different from each other.)

4.4.1 Major Findings

Mapping of AF has been dependent heavily on EGM analysis. However, little is known of the variability in EGM characteristics based on bipolar vector orientation or inter-electrode distance. This ancillary study undertaking detailed mapping in patients with persistent AF demonstrates the following:

- Bipolar vector orientation impacts EGM amplitude and EGM-derived measures. It may limit the reproducibility of 3D atrial surface reconstruction during AF-related substrate characterisation.

- Inter-electrode spacing also influences the EGM-derived measures.

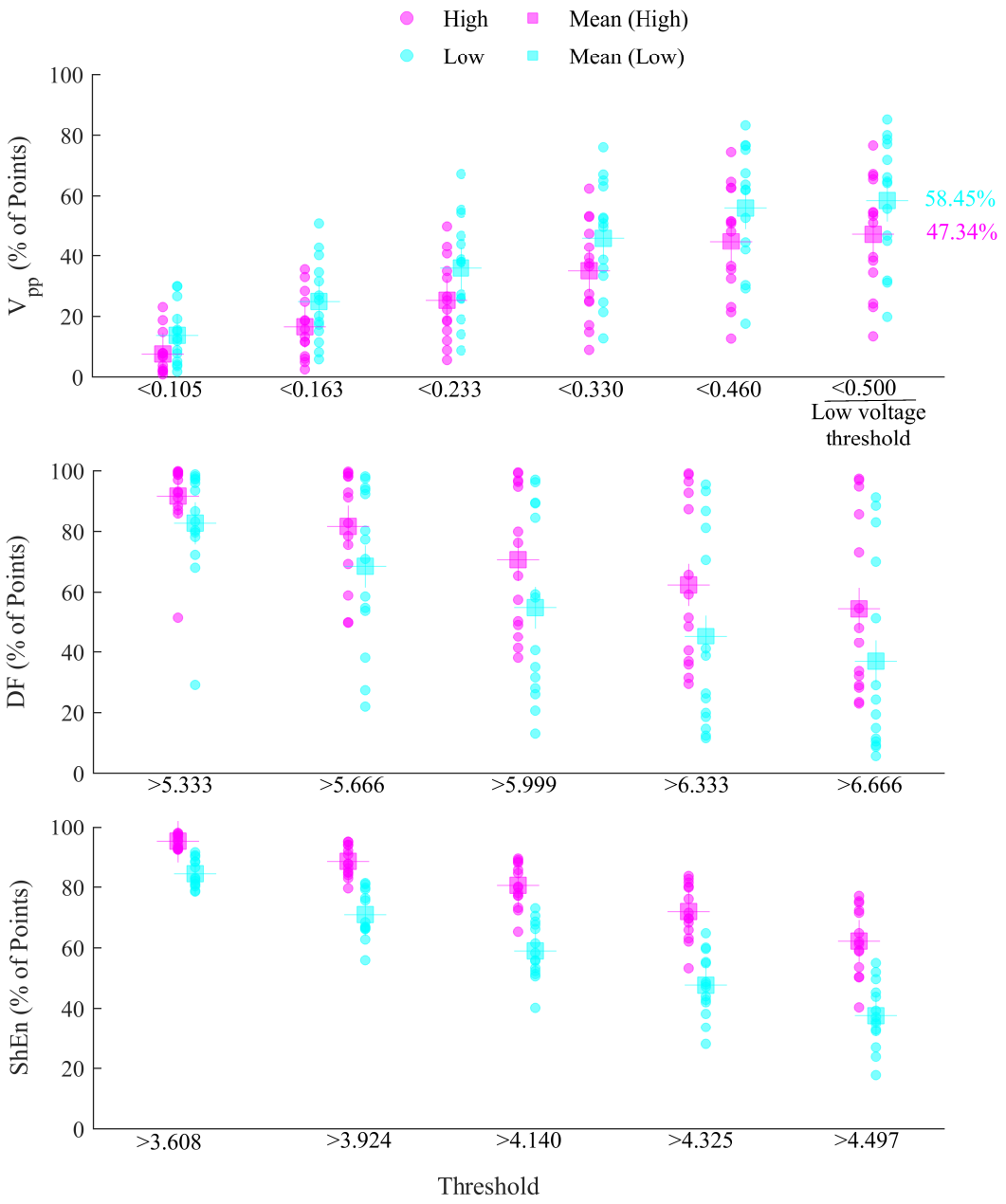

Figure 4.4. Percentage of points (atrial sites) below or above certain thresholds defined as 10, 20, 30 and 40 percentiles and the median. In case of Vpp, the previously used low voltage threshold (i.e., $0.5mV$) is also included. Deviation in the measurement due to 2 bipolar vector orientations placed at 90° angular distance, cause variability in EGM-derived Vpp, DF and ShEn.

These findings highlight the variability using current mapping techniques and have important implications for the reproducibility and interpretation of substrate-based AF mapping.

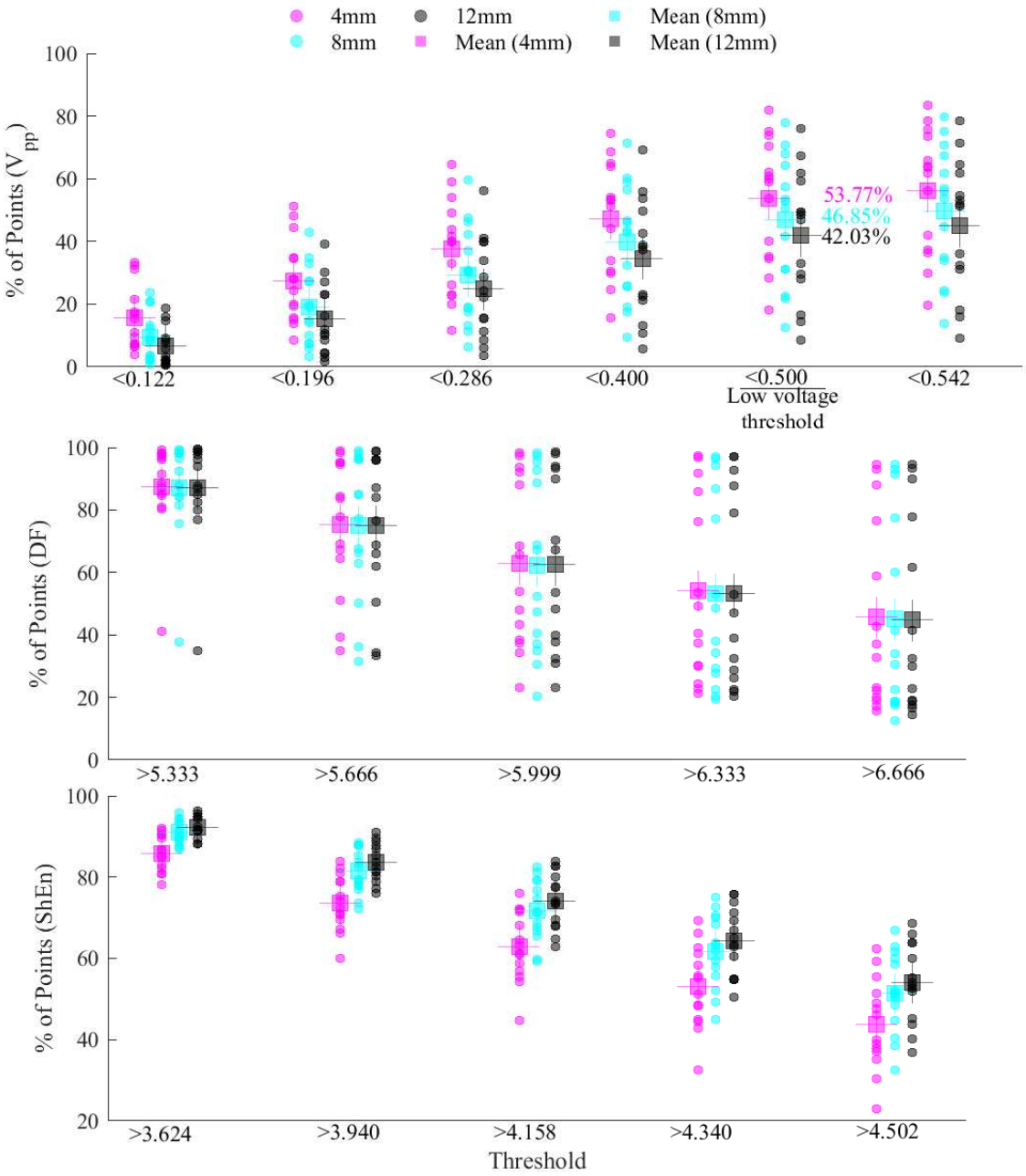

Figure 4.5. Percentage of points (atrial sites) below or above certain thresholds defined as 10, 20, 30 and 40 percentiles and the median. In case of Vpp, the previously used low voltage threshold (i.e., $0.5mV$) is also included. Deviation in the measurement due to bipolar electrodes placed at $4mm$, $8mm$, and $12mm$, respectively cause variability in EGM-derived measures.

4.4.2 Impact of bipolar vector orientation

Assuming a single planar wave propagation in a $2D$ homogenous medium/surface, the EGM amplitude is at a theoretical maximum if the propagation vector is exactly

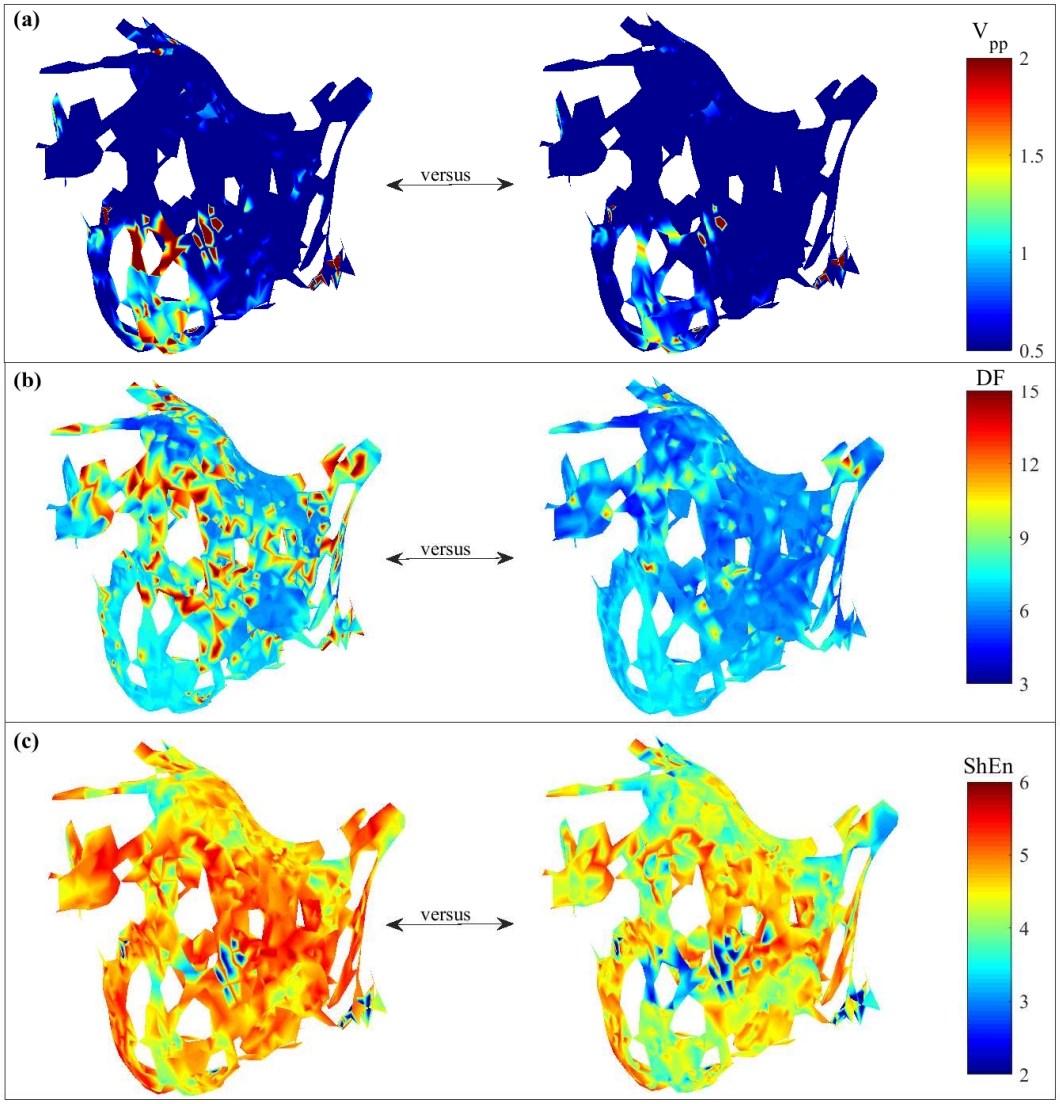

Figure 4.6. 3D atrial maps, i.e., (a) Vpp, (b) DF and (c) ShEn, reconstructed using two diagonally orthogonal bipolar EGM measurement ('high' vs. 'low' group), i.e., bipolar EGM were recorded with two bipolar vectors having an angular distance of 90^0. [Note: to maintain a defined spatial resolution, triangles having any of the three lines $> 6mm$ were excluded and kept disconnected.]

parallel to the bipolar lead vector; in the case of perfect perpendicular orientation, the EGM amplitude is zero. Consequently, a bipolar vector can detect activation waves with the maximum directional uncertainty of 180° (Deno *et al.* 2016). Studies have demonstrated altered Vpp values for two diagonally orthogonal bipolar vector orientations while maintaining an identical centre (Beheshti *et al.* 2018, Takigawa *et al.* 2018). Beheshti *et al.* have shown larger amplitudes occur when the bipolar vector is perfectly

parallel to the propagation vector (at 0°) as compared to perpendicular bipolar vector (at 90°).

During AF, the coordinated activation of the atria is replaced by an irregular multi-directional activation pattern. Additionally, with the progression of the underlying arrhythmogenic substrate, the complexity of the fibrillatory process increases and is characterised by more and narrower activation wave fronts, slower conduction, higher number of breakthrough waves and electrical dissociation likely reflecting an increase in transmural conduction and the development of a 3D AF substrate (Eckstein *et al.* 2010, Lau *et al.* 2017, Thanigaimani *et al.* 2017, Verheule *et al.* 2014). Therefore, wave propagation vectors during persistent AF are not stable and activation patterns are often not stationary during continuous bipolar EGM recording.

By using the novel high-density grid catheter, which allows characterisation of one continuous 3-second EGM recording by reconstructing different bipolar vectors, we showed, that Vpp, DF and ShEn are highly dependent on bipolar vector orientation. The percentage of bipolar EGM having Vpp $< 0.5mV$ differed due bipolar vector orientations maintaining an angular distance of 90° between two diagonally orthogonal bipolar vectors (inter-electrode spacing $\approx 5.65mm$), indicating that threshold-based substrate characterisation is not independent of bipolar vector orientation and, thus potentially induce measurement uncertainty that might make it hard to unravel the AF-related substrates.

This study further demonstrates that DF and ShEn maps are highly sensitive to bipolar vector orientation. Alteration in DF and ShEn values might be caused by multiple variables such as the amplitude of the wavefronts that are captured by EGM. Small amplitudes of local activations may impact power spectrum density estimation for DF calculation and increase the probability of values in the histogram used for determining ShEn.

4.4.3 Impact of inter-electrode spacing

This is the first study assessing the effect of inter-electrode distance on EGM-derived measures in humans with persistent AF. Increased Vpp values with increasing inter-electrode spacing, i.e., $4mm$, $8mm$, and $12mm$, respectively, was observed in human AF patients. This study quantifies the variability in EGM measurement due to the difference in inter-electrode spacing. Specifically, the percentage of atrial recording

sites below a previously used low voltage threshold, i.e., Vpp$<$ $0.5mV$, varies for altered inter-electrode spacing. A recent study has furthermore demonstrated that bipolar voltage distributions differ regionally according to the underlying rhythm, i.e., sinus rhythm, AF and other arrhythmias, which implicates the low voltage threshold might be adjusted to be regionally specific for each different rhythm (Rodríguez-Mañero *et al.* 2018). It would be clinically more relevant to evolve a methodology of defining patient- and rhythm-specific voltage threshold, which must also be further adjusted as bipolar EGM amplitude increases with increasing inter-electrode spacing, evident from an *ex vivo* magnetic resonance imaging-defined ventricular scar areas on the porcine infarct model (Tung *et al.* 2016). Mori *et al.* have suggested taking the impact of inter-electrode spacing into account while characterising atrial substrates (Mori *et al.* 2018). Closer inter-electrode spacing offers better local field EGM while reducing the far-field effects significantly, and that would better differentiate scar and surviving myocardium tissue (Nguyen and Tumolo 2019, Takigawa *et al.* 2018). Further studies are required to understand the exact role of inter-electrode spacing in bipolar EGM-derived measures and the gravity of this effect on AF-ablation.

Interestingly, the DF values are not significantly different when extracted from EGM signals with an inter-electrode spacing of $8mm$ and $12mm$, respectively. This finding could be explained by the effect of the wave propagation vector and its prevalent influence on the EGM. Assuming the wave propagates uniformly through the whole $12mm$ distance, EGM collected using bipolar electrodes spaced at $4mm$, $8mm$, and $12mm$ apart would differ in amplitude; however, the predominant wave should be clearly present.

To date, ShEn has been used to characterise the pivot of a rotor that has been hypothesized as potential source of AF. Previous findings suggest pivots have higher ShEn values than the periphery of a rotor (Ganesan *et al.* 2014, Ganesan *et al.* 2013). This study implicates that variability in ShEn measurement due to diversity in bipolar vector orientation and inter-electrode spacing could influence the detection of rotors.

4.4.4 Limitations

This study demonstrated EGM measurement variability due to bipolar vector orientation with an uncertainty of 90°. It is inconclusive from this study if any of the orientations could detect the wave propagation dynamics with maximal impact. Because the wave propagation vector with respect to the bipolar vector orientation is unknown

and not all possible bipolar vector orientations spanning the whole 360° can be studied in practice. Additionally, the findings of this study are derived from EGM recorded during AF in the included 14 patients with persistent AF. Theoretically, the impact of inter-electrode spacing and bipolar vector orientation on EGM-derived measures may be even higher, when less complex fibrillatory processes with more regular and repetitive activation patterns (self-terminating AF episodes, AF after antiarrhythmic drug treatment or atrial flutter) are analysed (Eckstein *et al.* 2010, Verheule *et al.* 2014). This needs to be investigated in future studies.

4.5 Conclusion

Bipolar vector orientation and inter-electrode spacing both significantly affect EGM measures that may result in significant uncertainty around the electroanatomical characterisation of atrial substrates and potentially lead to misinterpretation of AF sources and ablation targets. This observation has important implications for atrial substrate characterisation and the assessment and definition of low voltage areas, which should be considered in the development of future mapping catheter tools and algorithms.

Chapter 5

Beamforming-inspired Spatial Filtering Technique

THE interpretation of bipolar EGM is not straightforward. Variables including bipolar lead (vector) orientation relative to the wave propagation dynamics significantly impact the EGM and EGM-derived measures, which are clinically used to select target sources for catheter ablation. In this study, left atrial unipolar EGM were recorded using a 4×4 grid of 16 unipolar electrodes. A set (node) of 4 unipolar EGM were used to construct 6 bipolar EGM to evaluate the measurement uncertainty within a particular node. A novel beamforming-inspired spatial filtering (BiSF) method is proposed to reduce the potential measurement uncertainty inevitable in bipolar EGM. Results show greater signal power gain (at least around $10dB$) for all BiSF EGM with better or similar signal-to-noise ratio as compared to their respective bipolar counterparts. In conclusion, reduced uncertainty in BiSF EGM improve the interpretation of EGM and EGM-derived measures used in clinical practice after further validation on a larger dataset.

Associated Publication: *Saha, S.*, D. Linz, P. Sanders and M. Baumert, "Beamforming-inspired spatial filtering technique for intracardiac electrograms," 2019 41st Annual International Conference of the IEEE Engineering in Medicine and Biology Society (EMBC), Berlin, Germany, 2019, pp. 4254-4257.

5.1 Introduction

Bipolar EGM are naturally dependent on bipolar lead (vector) orientation. The EGM amplitude is at the theoretical maximum if the wave propagation vector is exactly parallel to the bipolar lead vector. In case of perpendicular orientation, the EGM amplitude is zero while assuming a single planar wave propagation in a 2D homogeneous surface/medium (Deno *et al.* 2016). Larger EGM amplitudes occur when the bipolar lead is perfectly parallel to the wave propagation vector (at 0°) as compared to perpendicular placement (at 90°) (Beheshti *et al.* 2018). Another recent study has demonstrated that two orthogonally bipolar leads provide altered EGM amplitudes although both leads represent a common atrial site in a 3D atrial map during catheter ablation (Takigawa *et al.* 2018). In addition, the previous chapter demonstrated the impact of bipolar vector orientation on EGM. The findings show significant variability in EGM measurement due to the directed placement of the bipolar lead orientation.

In multiuser wireless communications, the beamforming technique is used to achieve the maximum gain of a signal arriving from only the direction of interest while minimising the effect of undesired signals arriving from other random directions (Wongchampa and Uthansakul 2017). Diversity gain achieved using a set of beamformers placed in particular directions can augment the signal strength (Jeong *et al.* 2015). The concept of the proposed spatial filtering technique is based on the same motivation of conventional beamforming used in wireless communications. The underlying hypothesis was to detect enhanced intracardiac signal while maximising diversity gain by forming hypothetical beamformers within a node of four unipolar electrodes.

In this study, the measurement uncertainty quantified by the signal-to-noise ratio (SNR) and signal power has been evaluated on a set of six bipolar EGM constructed using 4 unipolar electrodes in a common node. A novel beamforming-inspired spatial filtering (BiSF) is used to intertwine bipolar components into an improved signal that not only offers better or comparable SNR but higher signal power.

5.2 Methods

5.2.1 Unipolar EGM and bipolar EGM construction

Data used in this experiment were recorded from a human subject undergoing catheter ablation due to symptomatic drug-refractory persistent AF. The ethics committee of

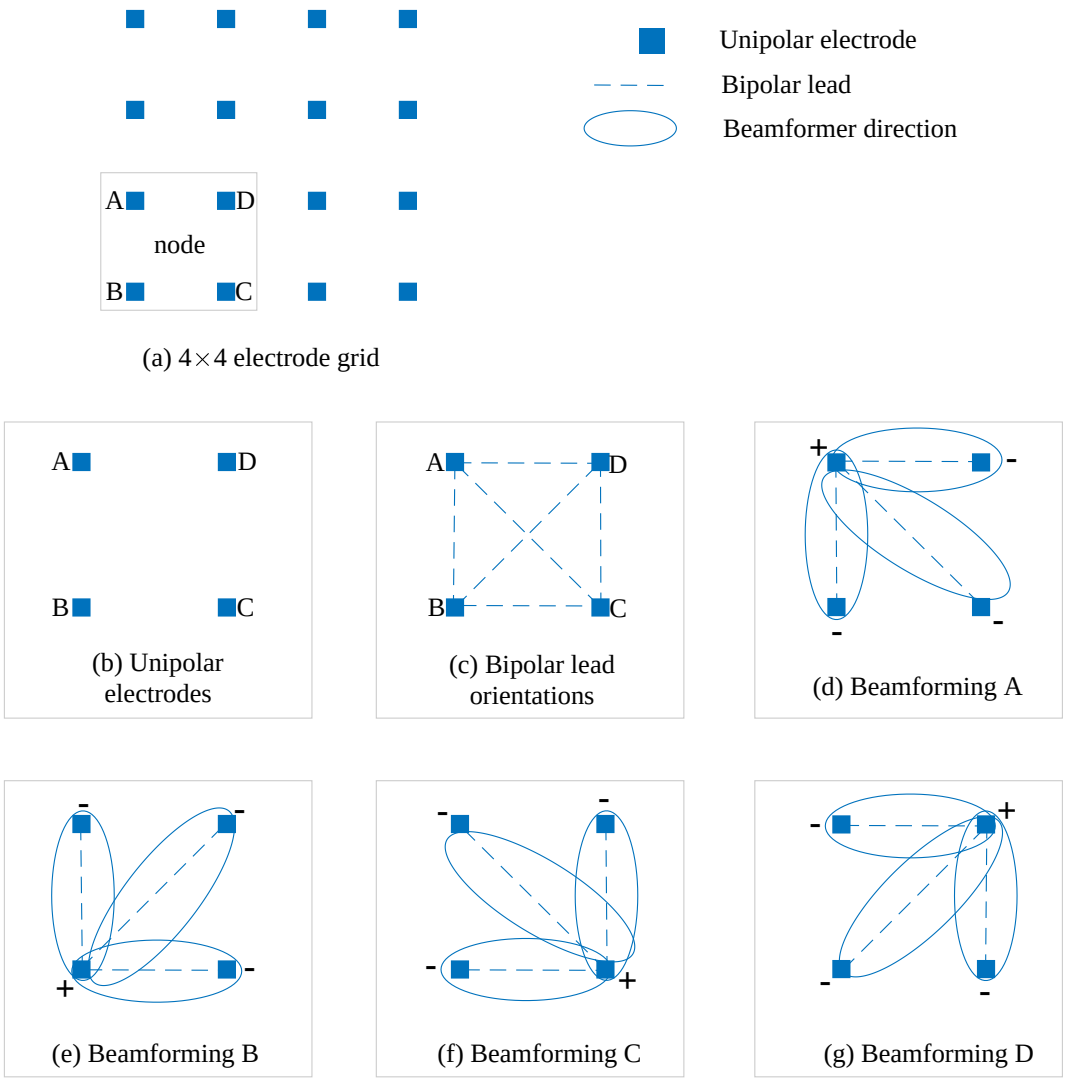

Figure 5.1. Illustration of four beamforming centres, each constructed using set of three bipolar leads placed equally at 45°: (a) 4×4 grid of electrodes, (b) 4 unipolar electrodes at each node, (c) possible six bipolar leads, (d)-(g) construction of hypothetical beamformers centered at unipolar electrodes.

the Royal Adelaide Hospital had approved the study. A high-density grid catheter (Abbott) with a grid of 18 unipolar electrodes was used. The unipolar electrodes are aligned in four parallel struts and the spacing between two adjacent struts is $4mm$ ($\pm 0.5mm$). The centre-to-centre distance between two adjacent electrodes along a strut is $4mm$ ($\pm 0.5mm$). The inter-electrode spacing (centre-to-centre) is $4mm$ for any two adjacent electrodes along or across the strut. The length of each electrode is $1mm$ with an outer diameter of $0.81mm$. Recordings were acquired at $2034.5Hz$ and preprocessed

using a notch filter ($50Hz$) and a bandpass filter ($30 - 300Hz$) to eliminate the power-line noise and to extract the clinically important band of the signal.

The prerequisite for applying the proposed filtering technique is that the grid of electrodes has to be of size $N \times N$ as shown in Figure 5.1(a). For this experiment only 16 electrodes were considered to define 9 nodes, each having 4 unipolar electrodes (designated as A, B, C and D in Figure 5.1(b)) placed at an equal distance to each other. Using 4 unipolar EGM at each node, the maximum possible six bipolar leads were constructed (Figure 5.1(c)). Total of 24 nodes were included in the analysis in which the visual annotation of signal and noise as possible. The inclusion of each node was determined by visual inspection, i.e., for this study bipolar EGM from a node were considered if distinct atrial local activation patterns can be annotated. While EGM from all 54 nodes (i.e., 6 shots of recording) were visually inspected, EGM from only 24 nodes were identified suitable for demonstrating the effect of beamforming.

For each node, bipolar EGM, beamforming EGM and BiSF EGM were visually inspected. Signal components and noise components were annotated carefully. Finally, SNR and signal power were calculated. The signal power was calculated as the sum of the absolute squares of its time-domain samples divided by the signal length. A ratio of signal and noise power measured in the dB scale is the SNR of a signal.

5.2.2 Beamforming construction and spatial filtering

At each node, a beamforming EGM was constructed centered at a unipolar electrode combining three different hypothetical beamformers (i.e., bipolar leads). Notably, a unipolar electrode was kept common for constructing bipolar leads used for constructing beamforming EGM as indicated in Figure 5.1(d-g). The related bipolar EGM were simply added. The underlying assumption was that wave propagation vector arriving toward each beamforming centre does not change the direction abruptly within the $4 \times 4mm^2$ areas spanned by 4 electrodes. Each beamforming EGM would achieve diversity gain within at least 90° radius. After constructing four beamforming EGM, peak cross-correlation coefficients were estimated between any two beamforming EGM. The two beamforming EGM with the highest correlation were added to get BiSF EGM.

5.3 Results and Discussion

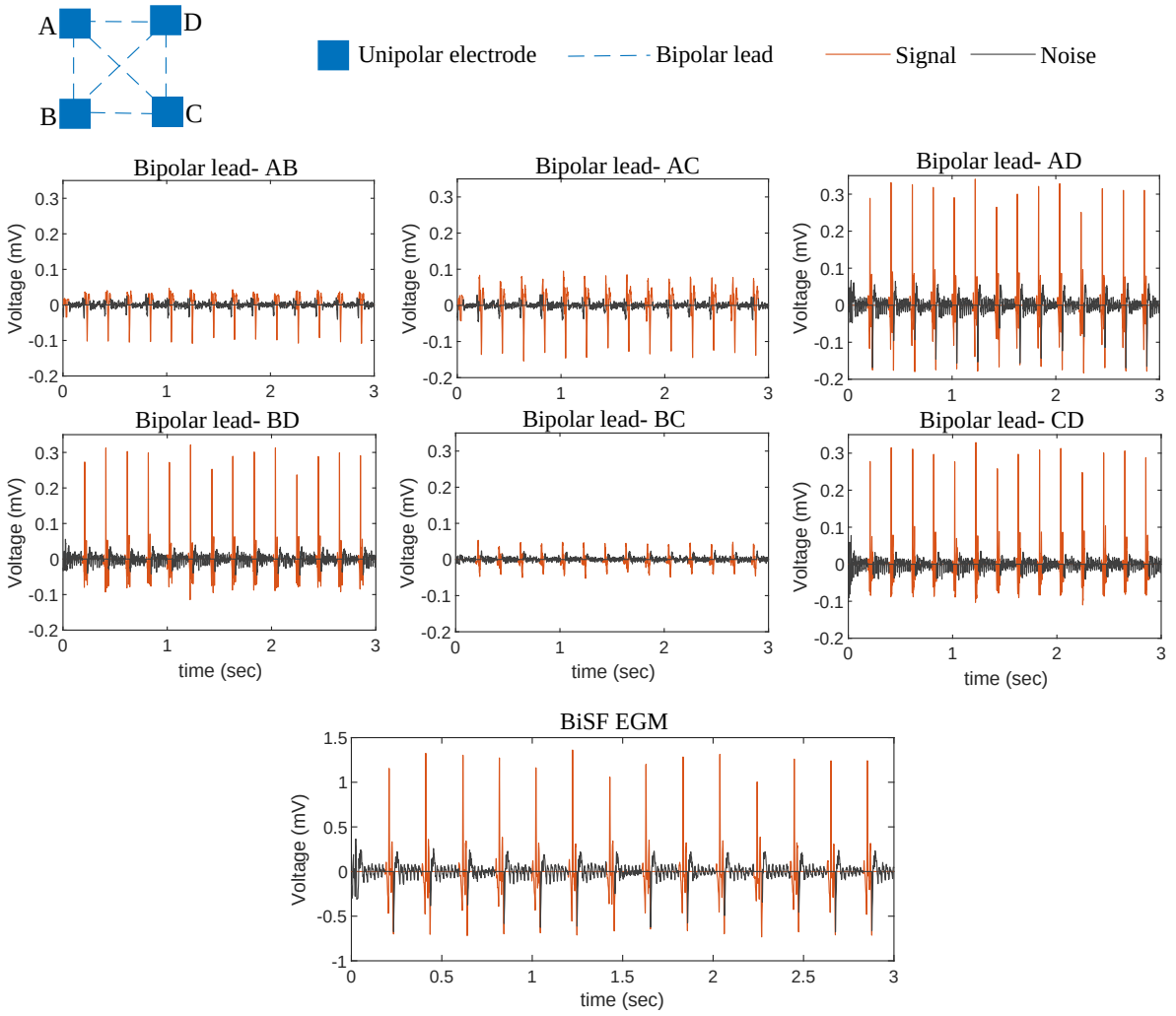

Figure 5.2. Four unipolar electrodes, six bipolar leads and bipolar EGM and corresponding Beamforming-inspired Spatial Filtered EGM.

5.3.1 Measurement uncertainty and substrate characterisation

Figure 5.2 shows six bipolar EGM and corresponding BiSF EGM for a particular node. It is evident that bipolar EGM varies significantly due to diverse lead orientations relative to the wave propagation. Notably, the EGM for leads AC and BD differ significantly although both represent a common atrial site during the 3D reconstruction of atrial anatomy. The frequency of annotated signal components seems unchanged here. However, the difference in the amplitudes intensify measurement uncertainty that would have an explicit impact on voltage threshold-based substrate characterisation. For example, peak-to-peak voltage threshold ($< 0.5mV$) is often used clinically

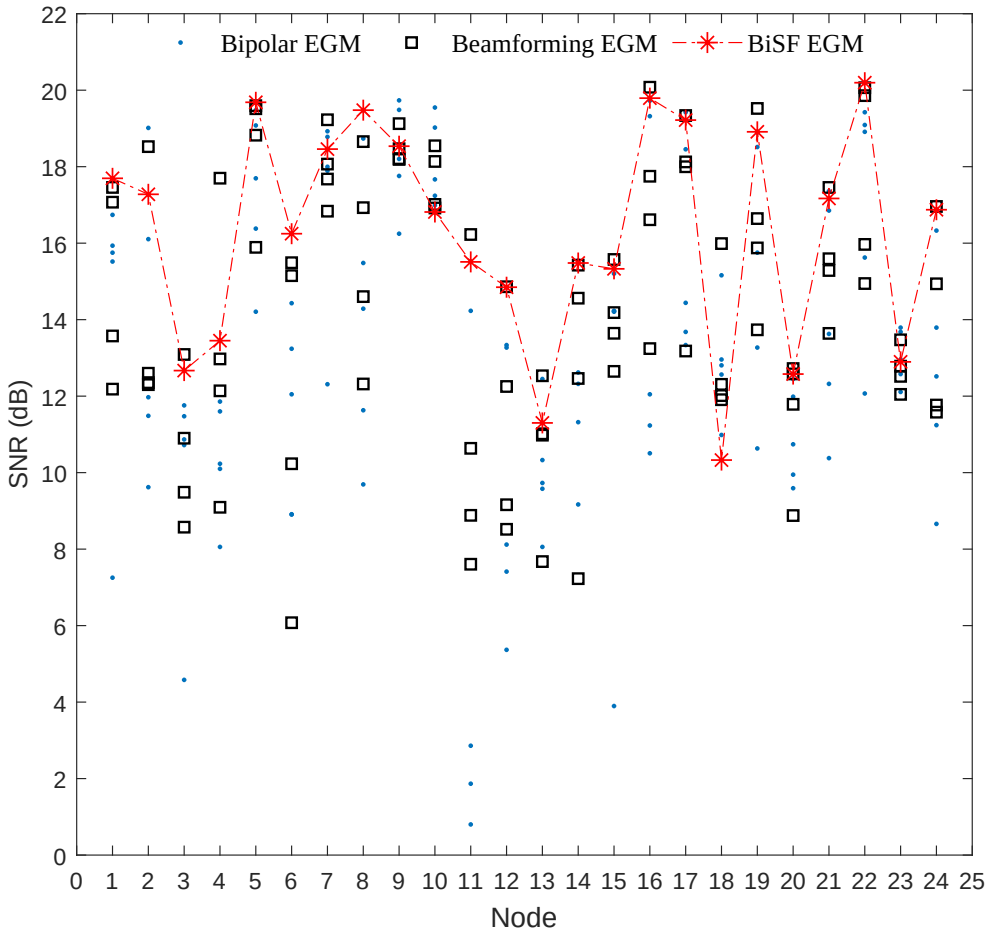

Figure 5.3. Signal-to-noise ratio (SNR) of bipolar EGM, beamforming EGM and corresponding BiSF EGM for 24 different nodes.

to specify low voltage areas assumed to manifest scar/fibrotic tissues. In this circumstance, BiSF EGM would be a potential alternative to using conventional bipolar EGM to propose a more reliable mapping tool.

The addition of signals from multiple bipolar orientations should be larger than any single EGM. This must be studied further to formulate any scaling factor for a BiSF signal to make a comparison with its bipolar counterparts. The significance of scaling would essentially be on threshold-based AF-related substrate characterisation. However, the mathematical interpretation of the BiSF method is difficult by using data with a regular clinical setup. An alternative way of further investigating the effectiveness of the proposed BiSF method is *in silico* simulation of wave propagation dynamics with diverse wavefront characteristics in 2D or 3D homogeneous surface (Deno *et al.* 2016).

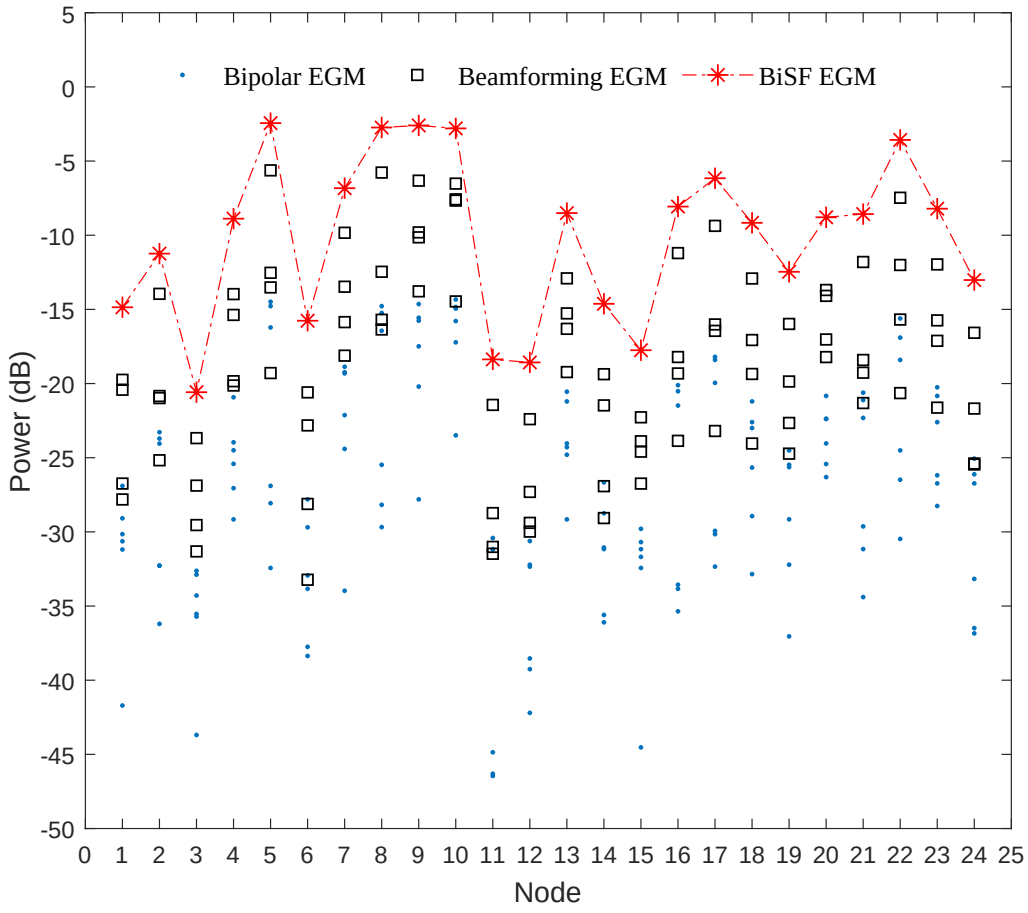

Figure 5.4. Signal power of bipolar EGM, beamforming EGM and BiSF EGM for 24 different nodes.

Before validating on clinical setting, the BiSF method could then be applied to HD-grid recordings from an animal model in a more controlled environment.

5.3.2 Improved EGM detection and diversity gain

Figure 5.3 illustrates the SNR values for bipolar EGM, beamforming EGM and BiSF EGM. Results suggest significant variability occurs in SNR values regarding the six bipolar leads at each node, which further quantifies the probable uncertainty in bipolar EGM measurement. The SNR values for beamforming EGM also vary considerably. In contrast, BiSF EGM offer comparable SNR values relative to their bipolar counterparts.

Figure 5.4 elucidates the power of only the signal components annotated for bipolar EGM, beamforming EGM and BiSF EGM, respectively. Results clearly indicate increased signal gain for BiSF EGM as compared to its bipolar counterparts. This is

analogous to the idea of diversity gain while combining signals arriving from different directions (Jeong *et al.* 2015).

5.3.3 Directionality in bipolar EGM-based cardiac mapping

Multiple variables including bipolar lead orientation as relative to the wave propagation vector, inter-electrode spacing, electrode size and tissue contact, impact bipolar EGM (Anter and Josephson 2016). Both inter-electrode spacing and electrode size are predefined during catheter design. Tissue contact relies on the accuracy of placing electrodes during signal acquisition and it is an onerous task to maintain stable electrode placement in the presence of pulsatile blood flow and contraction of the heart muscles. Once EGM are already recorded using a catheter with certain specifications, the only variable that could be integrated into a mapping tool is the bipolar lead orientation. Previous studies have demonstrated the critical impact of bipolar lead orientation in cardiac mapping (Beheshti *et al.* 2018, Takigawa *et al.* 2018). This study has endeavored to quantify the impact of bipolar lead orientation in intracardiac EGM from a signal processing perspective. The idea of beamforming (combining spatially directed beamformers) is to maximise the diversity gain when signals may arrive from multiple directions. A bipolar EGM is related to the directionality of the lead orientation (Deno *et al.* 2016) and directional diversity of multiple bipolar leads would inspire to adopt the strategy like beamforming in the development of a cardiac mapping tool. The recently proposed Omnipolar technology is another potential strategy based on local electric field measurement to compensate for the impact of bipolar vector orientation (Deno *et al.* 2016). While Omnipolar technology relies on the cell physiology and biophysical model, the BiSF method can be implemented using a specially designed multi-electrode catheter.

5.4 Conclusion

Exploiting directional diversity of bipolar lead orientations could enhance the reproducibility of EGM measurement. However, further analysis on a larger dataset is warranted to validate the potentiality of BiSF method after evaluating the clinical aspects of substrate characterisation during AF.

Chapter 6

A Ventricular Artefact Filtering Technique

A filtering technique integrating independent component analysis (ICA) and wavelet decomposition has been proposed to significantly reduce the ventricular far-field contents while preserving the EGM morphology related to atrial activations. First, the wavelet decomposition is applied to each unipolar EGM. Then, ICA is applied to the decomposed unipolar EGM components and surface ECG template. Each independent component is cross-correlated with the simultaneously recorded ECG template and the three components with higher correlation coefficients were eliminated before applying inverse ICA. Total of 126 unipolar EGM collected from an atrial fibrillation patient have been included. Results indicate that the proposed filtering can reduce the ventricular signal power by around $17dB$. Furthermore, the signal-to-noise ratio is increased by approximately $17dB$ after applying the proposed filtering. In conclusion, the proposed filtering method could be used for atrial fibrillation-related intracardiac mapping for catheter ablation.

Associated Publication: *Saha, S.*, S. Hartmann, D. Linz, P. Sanders and M. Baumert, "A ventricular far-field artefact filtering technique for atrial electrograms," 2019 Computing in Cardiology (CinC), Singapore, Singapore, 2019, pp. 1-4.

6.1 Introduction

Ventricular far-field potentials often influence local EGM recordings. Specifically, unipolar EGM are more likely to be influenced by the ventricular artefacts. Although current mapping systems use bipolar EGM that are assumed to be less sensitive to the far-field potentials, bipolar EGM are constructed from unipolar EGM. Thus, it is important to characterise the influence of inevitable ventricular far-field effects on local unipolar EGM. It is essential to further evaluate the effects on bipolar EGM.

Rieta and Hornero have studied the effect of ventricular activities on both unipolar and bipolar EGM signal and described three different techniques for removing ventricular artefacts (Rieta and Hornero 2007). The techniques are independent component analysis (ICA)-based filtering, template matching, and subtraction and adaptive ventricular cancellation.

In this study, a combination of ICA and wavelet decomposition (WD) has been utilised to reduce the effects of ventricular contents on local unipolar EGM. Previous studies integrated wavelet transform and independent component analysis for source separation in single channel recording (Mijovic *et al.* 2010, Hartmann and Baumert 2019). The underlying motivation of using ICA is that atrial and ventricular activities can be considered statistically independent originated from two distinct sources (Rieta *et al.* 2004). In that case, in the electrode output, i.e., unipolar EGM is the mixture of both atrial and ventricular contents.

6.2 Methods

6.2.1 Intracardiac electrogram acquisition

This study had been approved by the ethics committee of the Royal Adelaide Hospital. An array of 18 unipolar electrodes (EnSite^{TM} HD Grid Catheter, Abbott Medical) was used to record the left atrial intracardiac EGM from a patient undergoing catheter ablation due to symptomatic drug-refractory persistent AF. The detailed specifications of the electrode array are discussed in Chapter 4 and 5. The sampling rate was set at 2034.5 Hz.

The EGM were acquired for 3 seconds for each shot along with surface ECG. Each shot consists of simultaneously recorded 18 unipolar EGM. A total of 7 shots were

included in this analysis after visually inspecting them for the annotation of significant contamination of ventricular far-field potentials in local atrial EGM. As a result, the performance of the proposed filtering technique has been validated on 126 unipolar recordings.

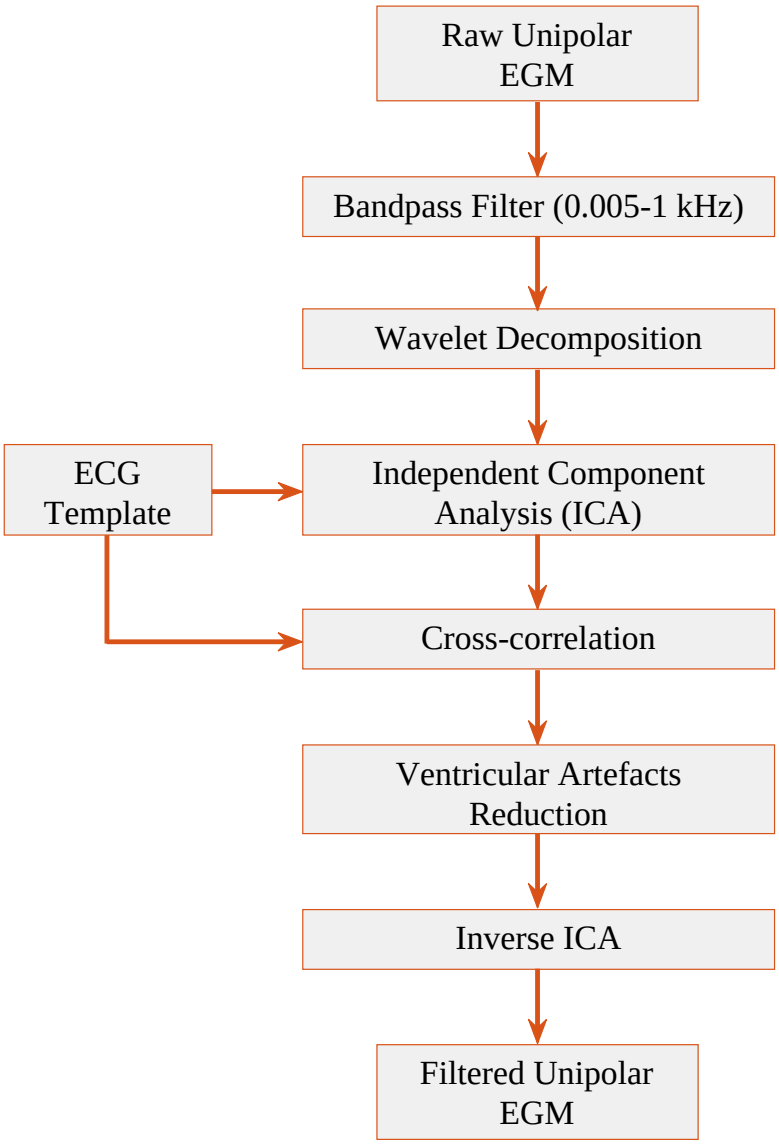

Figure 6.1. A basic block diagram illustrating the proposed filtering technique integrating independent component analysis and wavelet decomposition.

6.2.2 Ventricular artefact reduction method

Figure 6.1 illustrates the basic block diagram of the proposed filtering method for ventricular artefact reduction. The raw unipolar EGM were first filtered using a bandpass (Butterworth) filter of order 4. The corner frequencies were 5 Hz and 1 kHz. The low

cut-off was used to eliminate any baseline drift from the raw EGM and the high cut-off is selected to maintain the Nyquist rate (approximately half of the sampling rate). Then, each unipolar EGM was decomposed up to level 6 using wavelet transform. The used wavelet basis was Coiflet 5 due to its morphological resemblance to the QRS complex morphology. Simultaneously recorded lead II ECG ($30 - 300$ Hz) was considered as a template for characterising ventricular contents, i.e., QRS event related to ventricular depolarization. The lead II was selected because it provides a relatively higher amplitude as compared to other ECG leads. A notch filter was applied to eliminate powerline interference, i.e., 50 Hz from both EGM and ECG.

ICA was then applied to the 8 signal contents including the 7 contents of unipolar EGM extracted by wavelet decomposition and one simultaneously recorded ECG. As a blind source separation technique, ICA works with N observed signals that are considered as mixtures of multiple signal contents from diverse independent sources. Assuming $x(t) \in \mathbb{R}^M$ represents the observed signals in M sensors (i.e., electrodes) and $s(t) \in \mathbb{R}^N$ represents N source signals, then the linear mixtures model for ICA decomposition can be written as follows (Hyvärinen and Oja 2000)

$$x(t) = As(t). \tag{6.1}$$

Here, $A \in \mathbb{R}^{M \times N}$ is the unknown mixing matrix that has to be estimated. ICA algorithms work by assuming the statistical independence of the source signals. In this study, the FastICA algorithm is used. FastICA transforms the observed signals by maximising non-gaussianity of the components, which is an alternative manifestation of statistical independence. For more details of FastICA algorithm, please refer to (Hyvärinen and Oja 1997, Hyvärinen and Oja 2000).

Each of the eight independent components was cross-correlated with the ECG template. Finally, three independent components showing higher cross-correlation were eliminated proceeding to inverse ICA to reconstruct the filtered EGM. The number of independent components to be eliminated was selected based on empirical investigation for this preliminary study.

6.2.3 Performance evaluation

The performance of the proposed filtering technique was evaluated by estimating the reduction in signal power in QRS events as defined by a 125 ms window. Figure 6.2

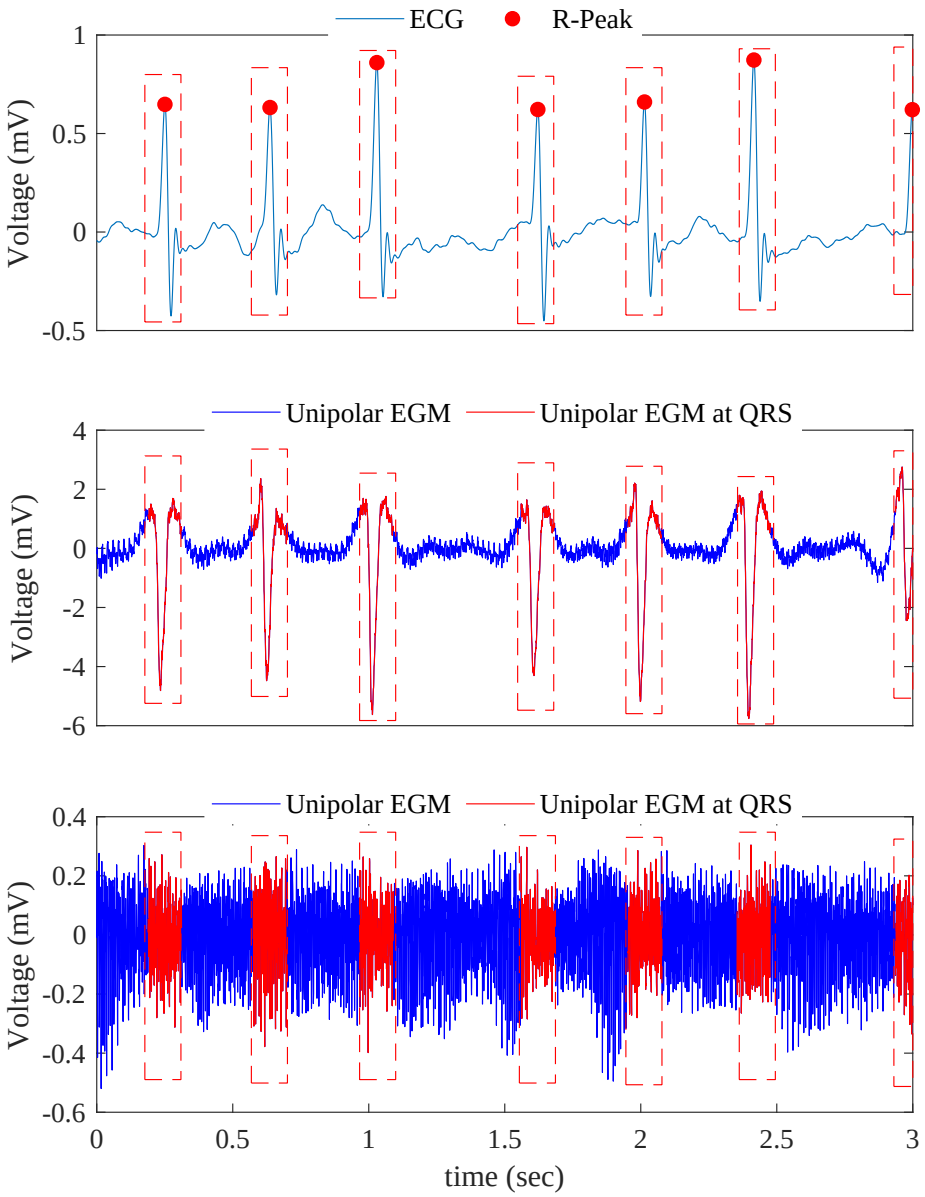

Figure 6.2. Illustration of defining ventricular signal contents as characterised by QRS complexes, top-bottom: lead II surface ECG and R-peak annotations, signal and noise contents before and after ventricular artefact elimination (Note: a 125ms window is placed at each QRS event to define the ventricular signal).

depicts the definition of the ventricular contents (characterised by the QRS complex) and the contents of the remaining signal. Ventricular artefact power was calculated on signal contents in the QRS-defined windows. Furthermore, the signal-to-noise ratio (SNR) was calculated by considering the signal contents at QRS events as noise and the remaining signal contents as a signal. It is to be noted that the SNR measurement

would be useful to investigate the contribution of ventricular far-field potentials in local atrial EGM.

Finally, statistical analysis was carried out to evaluate if the power at QRS-defined signal contents and SNR were significantly different. The Lilliefors test was applied to check the distributions of the power and SNR values with and without filtering. As the distributions do not follow Gaussianity, the Mann–Whitney U test was applied. P-values < 0.01 were considered significant.

6.3 Results and Discussion

Figure 6.2 delineates the effectiveness of the proposed filtering technique for ventricular artefact reduction. Specifically, the significant reduction of signal amplitudes in the QRS-defined ventricular artefacts implicates the potential use of the proposed method during intracardiac mapping for AF catheter ablation. The unipolar EGM included in this study are significantly contaminated with ventricular artefacts, i.e., QRS-defined events due to ventricular depolarization. As a surface ECG template includes the P-wave originating in atria, a more sophisticated method is further to be studied for minimising the effect of P-wave while eliminating only the QRS-defined ventricular event. Similarly, the definition of noise does not include T-wave originating in ventricles. Future improvements may consider this for a more precise interpretation of ventricular artefacts.

Figure 6.3 compares the power of QRS-defined ventricular artefacts for all 126 unipolar EGM with and without applying the proposed filtering technique. Overall, the ventricular power is decreased by around 17 dB after applying the filtering. Figure 6.4 indicates an increase in SNR by approximately 17 dB. Both the increase in SNR and the decrease in QRS-defined ventricular signal power are evidence of the applicability of the proposed method in intracardiac mapping.

To date, there is no automatic filtering technique in commercially available mapping tools. Generally, the ventricular artefact reduction is done by visually inspecting the EGM in an electrophysiology laboratory, which is a tedious process. With the advancement of high density and high-resolution mapping tools, the proposition of an automated filtering method for ventricular artefact reduction would be practical. Typically, a band of $30 - 300$ Hz is used clinically to extract meaningful signal attributes that are

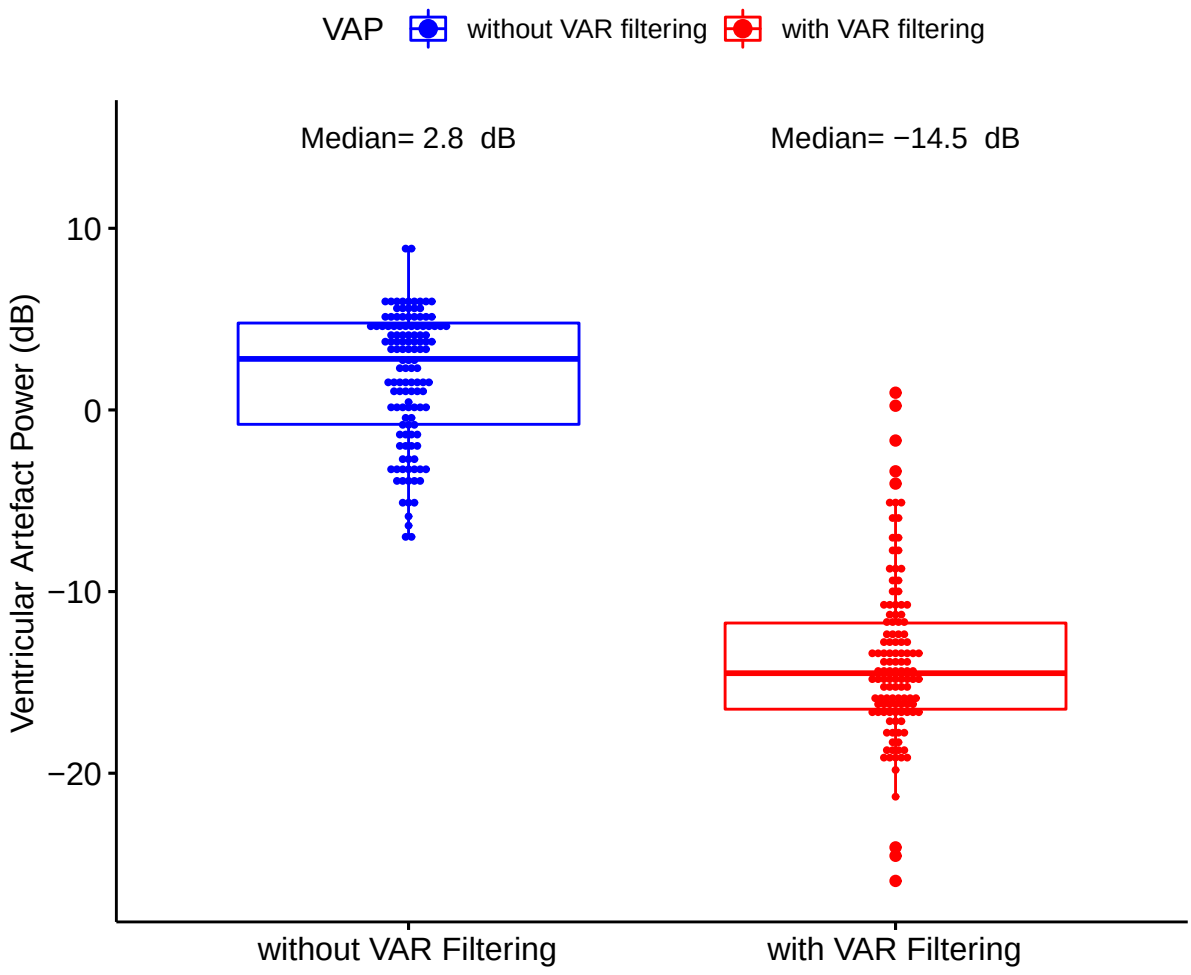

Figure 6.3. Comparison of the power of ventricular contents before and after ventricular artefact reduction filtering (VAR: ventricular artefact reduction).

used to identify ablation targets. However, the clinical significance of the signal contents in the eliminated bands would require to be further studied for scrutinising the effects of filtering in substrate-based AF ablation. As the peak-to-peak voltage is typically used for AF-related atrial substrate characterisation, it might be critical to filter the raw unipolar EGM carefully while preserving local amplitude and morphology.

Bipolar EGM are considered less sensitive to ventricular far-field potentials relative to unipolar EGM and current cardiac mapping tools use bipolar EGM for atrial substrate characterisation. There are multiple variables, including bipolar vector, inter-electrode spacing, electrode size and tissue contact that influence the interpretation of bipolar EGM (Anter and Josephson 2016, Saha *et al.* 2019b). Tissue contact depends on the accuracy of electrode placement during signal acquisition although it is very difficult to

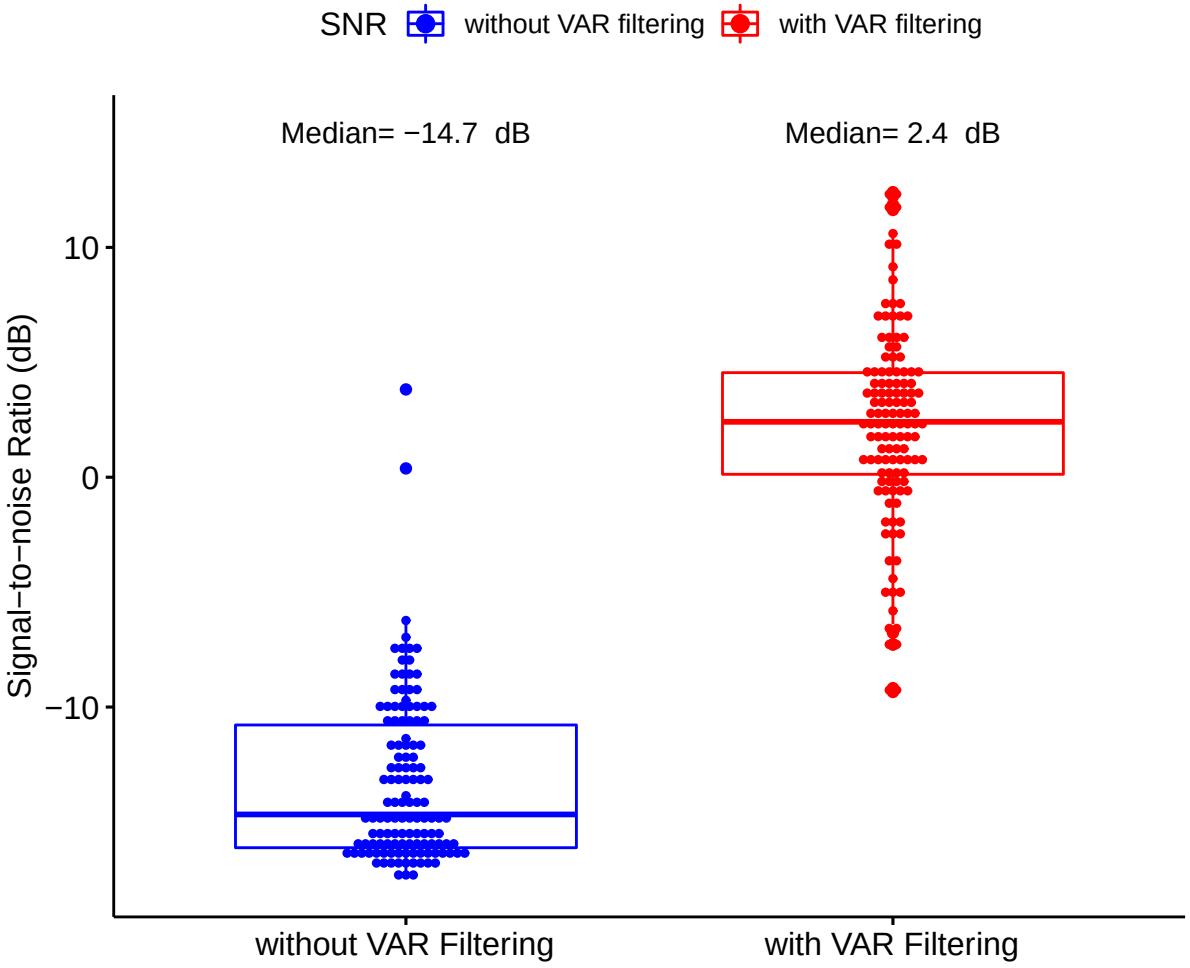

Figure 6.4. Comparison of the signal-to-noise ratio before and after ventricular artefact reduction filtering (VAR: ventricular artefact reduction).

maintain stable electrode placement in the presence of pulsatile blood flow and contraction of the heart muscles. As the bipolar EGM are constructed using unipolar EGM, it might be critical to carefully filter out undesired artefacts, i.e., ventricular far-field potentials while preserving the local EGM morphology for more accurate interpretation of bipolar EGM.

The elimination of three independent components was an arbitrary selection based on the experimental context. As mentioned earlier, all the unipolar EGM used in this study are severely contaminated with ventricular far-field effects. Notably, the unipolar EGM included in this preliminary study were selected from the atrial sites near the mitral valve. Future studies may consider algorithms for adaptive elimination of independent components for better preserving the local EGM morphology.

6.4 Conclusion

Intracardiac unipolar EGM are usually contaminated with ventricular far-field effects that may cause misinterpretation of AF-related target sources during catheter ablation. The proposed ICA and wavelet decomposition-based ventricular artefact reduction technique seems effective, which could be incorporated in future mapping tools after further validation on a larger dataset.

Chapter 7

Thesis Summary and Future Work

7.1 Significance Of Personalised Signal Processing

Biomedical signals often convey meaningful information that is associated with diverse physiological phenomena essential for a healthy human lifestyle. However, the interpretation of biomedical signals is a non-trivial task due to the time-variant and subject-specific physiological parameters. The signal acquisition-related variables further influence the characterisation of biomedical signals. This thesis delineates the impact of intra- and inter-subject variability and the signal acquisition-related variables in the context of cortical signal (i.e., noninvasive EEG) and cardiac signal (i.e., intracardiac EGM) processing.

To compensate for the variable (biomedical) signal dynamics, personalisation of signal processing algorithms is important. Personalisation refers to the inclusion of intra- and inter-subject variability and signal acquisition-related parameters to be included in the proposed signal processing-based strategies, which were investigated in the contexts of inter-subject associative BCI and intracardiac EGM-based AF mapping, respectively.

7.2 Inter-subject Associative BCI

Although the SMR-based BCI are often useful to augment human motor performance or to reinstate motor function in patients, inherent intra- and inter-subject variability in EEG dynamics hinders the generalisation of a proposed model for its use by a larger community. While such variability is related to the intrinsic motor learning process, it is essential to understand the associated nonstationary nature of EEG for enhanced BCI design.

Covariate shift adaptation strategies based on data-driven approaches (i.e., transfer learning) have been studied extensively for the reproducibility of a BCI model across subjects. But, a transfer learning strategy is ineffective if the subjects share dissimilar EEG nonstationarities that can not be efficiently modeled in an inter-subject context. The most significant contribution of this dissertation is the proposition of an inter-subject associative BCI. Results suggest that *inter-subject associativity*, i.e., predictors for subject independent BCI can augment only data-driven transfer learning strategies.

More comprehensive studies should aim at investigating the role of *inter-subject associativity* in data-driven transfer learning strategies for the proposition of more generalised BCI frameworks. Finding a potential psychological or neurophysiological predictor sometimes seems another tedious process, which is counterproductive for reducing or eliminating the calibration time. Although recent literature on intra- and inter-subject BCI performance predictors have reinforced our understanding of performance variation, a little is known about how the calibration time can be reduced to a minimum. The functional relevance of resting EEG is being extensively investigated. Studies found that resting EEG might be associated with SMR dynamics. As a result, the successful integration of resting EEG-related parameters into a BCI design could offer a significant reduction in the calibration time using only a few minutes of EEG before each use. Future studies may include the assessment of resting EEG as a potential measure of *inter-subject associativity* for SMR-based BCI.

7.3 Intracardiac EGM-based AF Mapping

Atrial fibrillation occurs due to the presence of disorganised and irregular electrical activities in atrial cardiomyocyte substrates. Patient-specific AF-related source (i.e., substrate) identification is the precursor to restoring sinus rhythm. However, the electrical activities recorded as intracardiac bipolar EGM are heavily dependent on bipolar vector orientation and inter-electrode spacing, which may hinder the reproducibility of AF maps and, thus, the target source identification.

Inter-electrode spacing is specified during the catheter design although recent multi-electrode array may offer multiple options. For example, this thesis demonstrated the impact of inter-electrode spacing on EGM by constructing EGM with electrodes spaced at 4mm, 8mm, and 12mm, respectively. From a signal processing perspective, the impact of bipolar vector orientation seems relatively more interesting. Directionality is

related to the conventional ideas of signal processing algorithms that have been widely used in wireless communication.

The concepts, i.e., the direction of arrival of a signal (e.g., radar) and the use of multiple spatially directed antennas are well-studied in wireless communication. In this thesis, the idea of beamforming was inspired by the direction of arrival of a signal and spatially directed multiple antennas to capture a signal of interest with increased gain. It has been hypothesized that the proposed beamforming-based filtering may be integrated using a multi-electrode catheter to produce more reliable AF maps.

Future studies should focus on the translational aspect of the demonstrated BiSF-based strategies after validation with clinical markers of AF-related substrates. The impact of bipolar vector orientation on EGM is apparent; notwithstanding, how to utilise the structure of specially designed multi-electrode catheters is yet to be studied comprehensively. With the advancement of signal processing and data-driven algorithms, taking advantage of spatially diverse bipolar vector orientations should not be unfeasible. Existing algorithms can be redesigned easily, but it is an important question on how to assess the efficacy of those methods for enhanced detection of AF-related substrates. In my opinion, the substrate characterisation is highly dependent on a cardiologist's individual perspective leading to potentially greater inter-rater disagreement. Building a database with expert cardiologists' mutually agreed annotations of AF-related sources can inspire engineers and scientists to apply available signal processing and data-driven methods for the development of a better mapping tool.

7.4 Conclusion

Quantification of variables that can potentially impact the biomedical signal characterisation is the predecessor step to personalised signal processing algorithm development. Once the role of a variable associated with intra- and inter-subject variability or signal acquisition is known, the signal processing algorithms could be customised to comprehend physiological changes in healthy and pathological conditions.

Bibliography

ABIBULLAEV-B., AN-J., JIN-S.-H., LEE-S. H., AND MOON-J. I. (2013). Minimizing inter-subject variability in fnirs-based brain–computer interfaces via multiple-kernel support vector learning, *Medical engineering & physics*, **35**(12), pp. 1811–1818.

ABRAMS-D. A., RYALI-S., CHEN-T., CHORDIA-P., KHOUZAM-A., LEVITIN-D. J., AND MENON-V. (2013). Inter-subject synchronization of brain responses during natural music listening, *European Journal of Neuroscience*, **37**(9), pp. 1458–1469.

ACQUALAGNA-L., BOTREL-L., VIDAURRE-C., KÜBLER-A., AND BLANKERTZ-B. (2016). Large-scale assessment of a fully automatic co-adaptive motor imagery-based brain computer interface, *PloS one*, **11**(2), p. e0148886.

AHN-M., AND JUN-S. C. (2015). Performance variation in motor imagery brain–computer interface: a brief review, *Journal of neuroscience methods*, **243**, pp. 103–110.

ALLAMI-N., PAULIGNAN-Y., BROVELLI-A., AND BOUSSAOUD-D. (2008). Visuo-motor learning with combination of different rates of motor imagery and physical practice, *Experimental Brain Research*, **184**(1), pp. 105–113.

ALLISON-B. Z., AND NEUPER-C. (2010). Could anyone use a BCI?, *Brain-computer interfaces*, Springer, pp. 35–54.

ANDUJAR-M., CRAWFORD-C. S., NIJHOLT-A., JACKSON-F., AND GILBERT-J. E. (2015). Artistic brain-computer interfaces: the expression and stimulation of the user's affective state, *Brain-computer interfaces*, **2**(2-3), pp. 60–69.

ANTER-E., AND JOSEPHSON-M. E. (2016). Bipolar voltage amplitude: what does it really mean?, *Heart Rhythm*, **13**(1), pp. 326–327.

ARVANEH-M., GUAN-C., ANG-K. K., AND QUEK-C. (2011). Optimizing the channel selection and classification accuracy in EEG-based BCI, *IEEE Transactions on Biomedical Engineering*, **58**(6), pp. 1865–1873.

ATHANASIOU-A., ARFARAS-G., PANDRIA-N., XYGONAKIS-I., FOROGLOU-N., ASTARAS-A., AND BAMIDIS-P. D. (2017). Wireless brain-robot interface: user perception and performance assessment of spinal cord injury patients, *Wireless Communications and Mobile Computing*.

ATIENZA-F., ALMENDRAL-J., JALIFE-J., ZLOCHIVER-S., PLOUTZ-SNYDER-R., TORRECILLA-E. G., ARENAL-A., KALIFA-J., FERNÁNDEZ-AVILÉS-F., AND BERENFELD-O. (2009). Real-time dominant frequency mapping and ablation of dominant frequency sites in atrial fibrillation with left-to-right frequency gradients predicts long-term maintenance of sinus rhythm, *Heart Rhythm*, **6**(1), pp. 33–40.

ATYABI-A., LUERSSEN-M., FITZGIBBON-S. P., LEWIS-T., AND POWERS-D. M. (2017). Reducing training requirements through evolutionary based dimension reduction and subject transfer, *Neurocomputing*, **224**, pp. 19–36.

BALDASSARRE-A., LEWIS-C. M., COMMITTERI-G., SNYDER-A. Z., ROMANI-G. L., AND CORBETTA-M. (2012). Individual variability in functional connectivity predicts performance of a perceptual task, *Proceedings of the National Academy of Sciences*, **109**(9), pp. 3516–3521.

BAUMERT-M., PORTA-A., AND CICHOCKI-A. (2016a). Biomedical signal processing: From a conceptual framework to clinical applications [scanning the issue], *Proceedings of the IEEE*, **104**(2), pp. 220–222.

BAUMERT-M., SANDERS-P., AND GANESAN-A. (2016b). Quantitative-electrogram-based methods for guiding catheter ablation in atrial fibrillation, *Proceedings of the IEEE*, **104**(2), pp. 416–431.

BEHESHTI-M., MAGTIBAY-K., MASSÉ-S., PORTA-SANCHEZ-A., HALDAR-S., BHASKARAN-A., NAYYAR-S., GLOVER-B., DENO-D. C., VIGMOND-E. J ETXXXXX AL.. (2018). Determinants of atrial bipolar voltage: inter electrode distance and wavefront angle, *Computers in biology and medicine*, **102**, pp. 449–457.

BELLMANN-B., PLENGE-T., SULTAN-A., AND STEVEN-D. (2018). First endocardial mapping of the left ventricle using the Advisor^{TM} HD Grid Catheter in a patient with a mitral valve clip, *European heart journal*, **39**(31), pp. 2911–2911.

BETZEL-R. F., AND BASSETT-D. S. (2017). Multi-scale brain networks, *Neuroimage*, **160**, pp. 73–83.

BETZEL-R. F., BERTOLERO-M. A., GORDON-E. M., GRATTON-C., DOSENBACH-N. U., AND BASSETT-D. S. (2019). The community structure of functional brain networks exhibits scale-specific patterns of inter-and intra-subject variability, *NeuroImage*.

BIRBAUMER-N., GHANAYIM-N., HINTERBERGER-T., IVERSEN-I., KOTCHOUBEY-B., KÜBLER-A., PERELMOUTER-J., TAUB-E., AND FLOR-H. (1999). A spelling device for the paralysed, *Nature*, **398**(6725), p. 297.

BLANKERTZ-B., CURIO-G., AND MÜLLER-K.-R. (2002). Classifying single trial EEG: Towards brain computer interfacing, *Advances in neural information processing systems*, pp. 157–164.

BLANKERTZ-B., MULLER-K.-R., KRUSIENSKI-D. J., SCHALK-G., WOLPAW-J. R., SCHLOGL-A., PFURTSCHELLER-G., MILLAN-J. R., SCHRODER-M., AND BIRBAUMER-N. (2006). The BCI Competition III: Validating alternative approaches to actual BCI problems, *IEEE transactions on neural systems and rehabilitation engineering*, **14**(2), pp. 153–159.

BLANKERTZ-B., SANELLI-C., HALDER-S., HAMMER-E., KÜBLER-A., MÜLLER-K.-R., CURIO-G., AND DICKHAUS-T. (2009). Predicting BCI performance to study BCI illiteracy, *BMC Neuroscience*, **10**(Suppl 1), p. P84.

BLANKERTZ-B., SANNELLI-C., HALDER-S., HAMMER-E. M., KÜBLER-A., MÜLLER-K.-R., CURIO-G., AND DICKHAUS-T. (2010). Neurophysiological predictor of SMR-based BCI performance, *Neuroimage*, **51**(4), pp. 1303–1309.

BOTTERON-G. W., AND SMITH-J. M. (1995). A technique for measurement of the extent of spatial organization of atrial activation during atrial fibrillation in the intact human heart, *IEEE Transactions on Biomedical Engineering*, **42**(6), pp. 579–586.

BRADBERRY-T. J., GENTILI-R. J., AND CONTRERAS-VIDAL-J. L. (2010). Reconstructing three-dimensional hand movements from noninvasive electroencephalographic signals, *Journal of Neuroscience*, **30**(9), pp. 3432–3437.

BROWN-R. E., AND MILNER-P. M. (2003). The legacy of Donald O. Hebb: more than the Hebb synapse, *Nature Reviews Neuroscience*, **4**(12), p. 1013.

BURSTEIN-B., AND NATTEL-S. (2008). Atrial fibrosis: mechanisms and clinical relevance in atrial fibrillation, *Journal of the American College of Cardiology*, **51**(8), pp. 802–809.

CHIARELLI-A. M., CROCE-P., MERLA-A., AND ZAPPASODI-F. (2018). Deep learning for hybrid EEG-fNIRS brain–computer interface: application to motor imagery classification, *Journal of neural engineering*, **15**(3), p. 036028.

CLARKE-C., AND JANDAY-B. (1989). The solution of the biomagnetic inverse problem by maximum statistical entropy, *Inverse Problems*, **5**(4), p. 483.

CLARKE-D. D. (1999). Circulation and energy metabolism of the brain, *Basic neurochemistry: Molecular, cellular, and medical aspects*.

CONGEDO-M., LOTTE-F., AND LÉCUYER-A. (2006). Classification of movement intention by spatially filtered electromagnetic inverse solutions, *Physics in Medicine & Biology*, **51**(8), p. 1971.

COSANDIER-RIMÉLÉ-D., MERLET-I., BADIER-J.-M., CHAUVEL-P., AND WENDLING-F. (2008). The neuronal sources of EEG: modeling of simultaneous scalp and intracerebral recordings in epilepsy, *NeuroImage*, **42**(1), pp. 135–146.

DARVISHI-S., GHARABAGHI-A., BOULAY-C. B., RIDDING-M. C., ABBOTT-D., AND BAUMERT-M. (2017). Proprioceptive feedback facilitates motor imagery-related operant learning of sensorimotor β-band modulation, *Frontiers in neuroscience*, **11**, p. 60.

DARVISHI-S., GHARABAGHI-A., RIDDING-M. C., ABBOTT-D., AND BAUMERT-M. (2018). Reaction time predicts brain–computer interface aptitude, *IEEE journal of translational engineering in health and medicine*, **6**, pp. 1–11.

DECO-G., JIRSA-V. K., AND MCINTOSH-A. R. (2011). Emerging concepts for the dynamical organization of resting-state activity in the brain, *Nature Reviews Neuroscience*, **12**(1), p. 43.

DENO-D. C., BALACHANDRAN-R., MORGAN-D., AHMAD-F., MASSÉ-S., AND NANTHAKUMAR-K. (2016). Orientation-independent catheter-based characterization of myocardial activation, *IEEE Transactions on Biomedical Engineering*, **64**(5), pp. 1067–1077.

DIMITRI-H., NG-M., BROOKS-A. G., KUKLIK-P., STILES-M. K., LAU-D. H., ANTIC-N., THORNTON-A., SAINT-D. A., MCEVOY-D ETXXXXX AL.. (2012). Atrial remodeling in obstructive sleep apnea: implications for atrial fibrillation, *Heart rhythm*, **9**(3), pp. 321–327.

DOBKIN-B. H. (2007). Brain–computer interface technology as a tool to augment plasticity and outcomes for neurological rehabilitation, *The Journal of physiology*, **579**(3), pp. 637–642.

DUARTE-J. E., AND REINKENSMEYER-D. J. (2015). Effects of robotically modulating kinematic variability on motor skill learning and motivation, *Journal of neurophysiology*, **113**(7), pp. 2682–2691.

ECKSTEIN-J., MAESEN-B., LINZ-D., ZEEMERING-S., VAN HUNNIK-A., VERHEULE-S., ALLESSIE-M., AND SCHOTTEN-U. (2010). Time course and mechanisms of endo-epicardial electrical dissociation during atrial fibrillation in the goat, *Cardiovascular research*, **89**(4), pp. 816–824.

EDELMAN-B. J., BAXTER-B., AND HE-B. (2016). EEG source imaging enhances the decoding of complex right-hand motor imagery tasks, *IEEE Transactions on Biomedical Engineering*, **63**(1), pp. 4–14.

EDELMAN-B., MENG-J., SUMA-D., ZURN-C., NAGARAJAN-E., BAXTER-B., CLINE-C., AND HE-B. (2019). Noninvasive neuroimaging enhances continuous neural tracking for robotic device control, *Science Robotics*, **4**(31), p. eaaw6844.

FAHIMI-F., ZHANG-Z., GOH-W. B., LEE-T.-S., ANG-K. K., AND GUAN-C. (2018). Inter-subject transfer learning with end-to-end deep convolutional neural network for EEG-based BCI, *Journal of neural engineering*.

FALLER-J., CUMMINGS-J., SAPROO-S., AND SAJDA-P. (2019). Regulation of arousal via online neurofeedback improves human performance in a demanding sensory-motor task, *Proceedings of the National Academy of Sciences*, **116**(13), pp. 6482–6490.

FAZLI-S., DÄHNE-S., SAMEK-W., BIESSMANN-F., AND MUELLER-K.-R. (2015). Learning from more than one data source: data fusion techniques for sensorimotor rhythm-based brain–computer interfaces, *Proceedings of the IEEE*, **103**(6), pp. 891–906.

FAZLI-S., POPESCU-F., DANÓCZY-M., BLANKERTZ-B., MÜLLER-K.-R., AND GROZEA-C. (2009). Subject-independent mental state classification in single trials, *Neural networks*, **22**(9), pp. 1305–1312.

FONOV-V., EVANS-A. C., BOTTERON-K., ALMLI-C. R., MCKINSTRY-R. C., COLLINS-D. L., AND GROUP-B. D. C. (2011). Unbiased average age-appropriate atlases for pediatric studies, *Neuroimage*, **54**(1), pp. 313–327.

FOX-K. C., SPRENG-R. N., ELLAMIL-M., ANDREWS-HANNA-J. R., AND CHRISTOFF-K. (2015). The wandering brain: Meta-analysis of functional neuroimaging studies of mind-wandering and related spontaneous thought processes, *Neuroimage*, **111**, pp. 611–621.

GANESAN-A. N., KUKLIK-P., GHARAVIRI-A., BROOKS-A., CHAPMAN-D., LAU-D. H., ROBERTS-THOMSON-K. C., AND SANDERS-P. (2014). Origin and characteristics of high shannon entropy at the pivot of locally stable rotors: insights from computational simulation, *PloS one*, **9**(11), p. e110662.

GANESAN-A. N., KUKLIK-P., LAU-D. H., BROOKS-A. G., BAUMERT-M., LIM-W. W., THANIGAIMANI-S., NAYYAR-S., MAHAJAN-R., KALMAN-J. M ETXXXXX AL.. (2013). Bipolar electrogram shannon entropy at sites of rotational activation: implications for ablation of atrial fibrillation, *Circulation: Arrhythmia and Electrophysiology*, **6**(1), pp. 48–57.

GERARDIN-E., SIRIGU-A., LEHÉRICY-S., POLINE-J.-B., GAYMARD-B., MARSAULT-C., AGID-Y., AND LE BIHAN-D. (2000). Partially overlapping neural networks for real and imagined hand movements, *Cerebral cortex*, **10**(11), pp. 1093–1104.

GONCALVES-S., DE MUNCK-J., POUWELS-P., SCHOONHOVEN-R., KUIJER-J., MAURITS-N., HOOGDUIN-J., VAN SOMEREN-E., HEETHAAR-R., AND DA SILVA-F. L. (2006). Correlating the alpha rhythm to BOLD using simultaneous EEG/fMRI: inter-subject variability, *Neuroimage*, **30**(1), pp. 203–213.

GRAMFORT-A., PAPADOPOULO-T., OLIVI-E., AND CLERC-M. (2010). OpenMEEG: opensource software for quasistatic bioelectromagnetics, *Biomedical engineering online*, **9**(1), p. 45.

GRECH-R., CASSAR-T., MUSCAT-J., CAMILLERI-K. P., FABRI-S. G., ZERVAKIS-M., XANTHOPOULOS-P., SAKKALIS-V., AND VANRUMSTE-B. (2008). Review on solving the inverse problem in EEG source analysis, *Journal of neuroengineering and rehabilitation*, **5**(1), p. 25.

HAMMER-E. M., HALDER-S., BLANKERTZ-B., SANNELLI-C., DICKHAUS-T., KLEIH-S., MÜLLER-K.-R., AND KÜBLER-A. (2012). Psychological predictors of SMR-BCI performance, *Biological psychology*, **89**(1), pp. 80–86.

HARTMANN-S., AND BAUMERT-M. (2019). Automatic A-phase detection of cyclic alternating patterns in sleep using dynamic temporal information, *IEEE Transactions on Neural Systems and Rehabilitation Engineering*, **27**(9), pp. 1695–1703.

HASSON-U., NIR-Y., LEVY-I., FUHRMANN-G., AND MALACH-R. (2004). Intersubject synchronization of cortical activity during natural vision, *science*, **303**(5664), pp. 1634–1640.

HE-B., BAXTER-B., EDELMAN-B. J., CLINE-C. C., AND WENJING-W. Y. (2015). Noninvasive brain-computer interfaces based on sensorimotor rhythms, *Proceedings of the IEEE*, **103**(6), pp. 907–925.

HE-H., AND WU-D. (2019). Transfer learning for brain–computer interfaces: A Euclidean space data alignment approach, *IEEE Transactions on Biomedical Engineering*, **67**(2), pp. 399–410.

HERZFELD-D. J., AND SHADMEHR-R. (2014). Motor variability is not noise, but grist for the learning mill, *nature neuroscience*, **17**(2), p. 149.

HÉTU-S., GRÉGOIRE-M., SAIMPONT-A., COLL-M.-P., EUGÈNE-F., MICHON-P.-E., AND JACKSON-P. L. (2013). The neural network of motor imagery: an ALE meta-analysis, *Neuroscience & Biobehavioral Reviews*, **37**(5), pp. 930–949.

HONEY-C. J., THIVIERGE-J.-P., AND SPORNS-O. (2010). Can structure predict function in the human brain?, *Neuroimage*, **52**(3), pp. 766–776.

HONEY-C., SPORNS-O., CAMMOUN-L., GIGANDET-X., THIRAN-J.-P., MEULI-R., AND HAGMANN-P. (2009). Predicting human resting-state functional connectivity from structural connectivity, *Proceedings of the National Academy of Sciences*, **106**(6), pp. 2035–2040.

HONG-X., LU-Z. K., TEH-I., NASRALLAH-F. A., TEO-W. P., ANG-K. K., PHUA-K. S., GUAN-C., CHEW-E., AND CHUANG-K.-H. (2017). Brain plasticity following MI-BCI training combined with tDCS in a randomized trial in chronic subcortical stroke subjects: a preliminary study, *Scientific reports*, **7**(1), p. 9222.

HOSSAIN-M. S., SAHA-S., HABIB-M. A., AL NOMAN-A., SHARFUDDIN-T., AND AHMED-K. I. (2016). Application of wavelet-based maximum entropy on the mean in channel optimization for BCI, *Medical Engineering, Health Informatics and Technology (MediTec), 2016 International Conference on*, IEEE, pp. 1–5.

HYVÄRINEN-A., AND OJA-E. (1997). A fast fixed-point algorithm for independent component analysis, *Neural computation*, **9**(7), pp. 1483–1492.

HYVÄRINEN-A., AND OJA-E. (2000). Independent component analysis: algorithms and applications, *Neural networks*, **13**(4-5), pp. 411–430.

JACKSON-P. L., LAFLEUR-M. F., MALOUIN-F., RICHARDS-C., AND DOYON-J. (2001). Potential role of mental practice using motor imagery in neurologic rehabilitation, *Archives of physical medicine and rehabilitation*, **82**(8), pp. 1133–1141.

JAYARAM-V., ALAMGIR-M., ALTUN-Y., SCHOLKOPF-B., AND GROSSE-WENTRUP-M. (2016). Transfer learning in brain-computer interfaces, *IEEE Computational Intelligence Magazine*, **11**(1), pp. 20–31.

JEANNEROD-M. (1995). Mental imagery in the motor context, *Neuropsychologia*, **33**(11), pp. 1419–1432.

JENSEN-O., BAHRAMISHARIF-A., OOSTENVELD-R., KLANKE-S., HADJIPAPAS-A., OKAZAKI-Y. O., AND VAN GERVEN-M. A. (2011). Using brain–computer interfaces and brain-state dependent stimulation as tools in cognitive neuroscience, *Frontiers in psychology*, **2**, p. 100.

JEONG-C., PARK-J., AND YU-H. (2015). Random access in millimeter-wave beamforming cellular networks: issues and approaches, *IEEE Communications Magazine*, **53**(1), pp. 180–185.

JEUNET-C., N'KAOUA-B., SUBRAMANIAN-S., HACHET-M., AND LOTTE-F. (2015). Predicting mental imagery-based BCI performance from personality, cognitive profile and neurophysiological patterns, *PloS one*, **10**(12), p. e0143962.

JOCHUMSEN-M., ROVSING-C., ROVSING-H., CREMOUX-S., SIGNAL-N., ALLEN-K., TAYLOR-D., AND NIAZI-I. K. (2017). Quantification of movement-related EEG correlates associated with motor training: a study on movement-related cortical potentials and sensorimotor rhythms, *Frontiers in human neuroscience*, **11**, p. 604.

JOHN-B., STILES-M. K., KUKLIK-P., BROOKS-A. G., CHANDY-S. T., KALMAN-J. M., AND SANDERS-P. (2010). Reverse remodeling of the atria after treatment of chronic stretch in humans: implications for the atrial fibrillation substrate, *Journal of the American College of Cardiology*, **55**(12), pp. 1217–1226.

JOHNSON-N., CAREY-J., EDELMAN-B., DOUD-A., GRANDE-A., LAKSHMINARAYAN-K., AND HE-B. (2018). Combined rTMS and virtual reality brain–computer interface training for motor recovery after stroke, *Journal of neural engineering*, **15**(1), p. 016009.

KAMOUSI-B., AMINI-A. N., AND HE-B. (2007). Classification of motor imagery by means of cortical current density estimation and Von Neumann entropy, *Journal of Neural Engineering*, **4**(2), p. 17.

KANG-H., AND CHOI-S. (2014). Bayesian common spatial patterns for multi-subject EEG classification, *Neural Networks*, **57**, pp. 39–50.

KANG-H., NAM-Y., AND CHOI-S. (2009). Composite common spatial pattern for subject-to-subject transfer, *IEEE Signal Processing Letters*, **16**(8), pp. 683–686.

KASAHARA-K., DASALLA-C. S., HONDA-M., AND HANAKAWA-T. (2015). Neuroanatomical correlates of brain–computer interface performance, *Neuroimage*, **110**, pp. 95–100.

KRAKAUER-J. W. (2006). Motor learning: its relevance to stroke recovery and neurorehabilitation, *Current opinion in neurology*, **19**(1), pp. 84–90.

KRUSIENSKI-D. J., GROSSE-WENTRUP-M., GALÁN-F., COYLE-D., MILLER-K. J., FORNEY-E., AND ANDERSON-C. W. (2011). Critical issues in state-of-the-art brain–computer interface signal processing, *Journal of neural engineering*, **8**(2), p. 025002.

LAHNAKOSKI-J. M., GLEREAN-E., JÄÄSKELÄINEN-I. P., HYÖNÄ-J., HARI-R., SAMS-M., AND NUMMENMAA-L. (2014). Synchronous brain activity across individuals underlies shared psychological perspectives, *NeuroImage*, **100**, pp. 316–324.

LAU-D. H., LINZ-D., SCHOTTEN-U., MAHAJAN-R., SANDERS-P., AND KALMAN-J. M. (2017). Pathophysiology of paroxysmal and persistent atrial fibrillation: rotors, foci and fibrosis, *Heart, Lung and Circulation*, **26**(9), pp. 887–893.

LEAMY-D. J., KOCIJAN-J., DOMIJAN-K., DUFFIN-J., ROCHE-R. A., COMMINS-S., COLLINS-R., AND WARD-T. E. (2014). An exploration of EEG features during recovery following stroke–implications for BCI-mediated neurorehabilitation therapy, *Journal of neuroengineering and rehabilitation*, **11**(1), p. 9.

LINA-J.-M., CHOWDHURY-R., LEMAY-E., KOBAYASHI-E., AND GROVA-C. (2014). Wavelet-based localization of oscillatory sources from magnetoencephalography data, *IEEE Transactions on Biomedical Engineering*, **61**(8), pp. 2350–2364.

LIP-G. Y. H., FAUCHIER-L., FREEDMAN-S. B., VAN GELDER-I., NATALE-A., GIANNI-C., NATTEL-S., POTPARA-T., RIENSTRA-M., TSE-H.-F., AND LANE-D. A. (2016). Atrial fibrillation, *Nature Reviews Disease Primers*, **2**, p. 16016.

LI-Q., LU-Z., GAO-N., AND YANG-J. (2019). Optimizing the performance of the visual P300-speller through active mental tasks based on color distinction and modulation of task difficulty, *Frontiers in human neuroscience*, **13**, p. 130.

LI-Y., KAMBARA-H., KOIKE-Y., AND SUGIYAMA-M. (2010). Application of covariate shift adaptation techniques in brain–computer interfaces, *IEEE Transactions on Biomedical Engineering*, **57**(6), pp. 1318–1324.

LOTTE-F. (2015). Signal processing approaches to minimize or suppress calibration time in oscillatory activity-based brain–computer interfaces, *Proceedings of the IEEE*, **103**(6), pp. 871–890.

LOTTE-F., AND GUAN-C. (2011). Regularizing common spatial patterns to improve BCI designs: unified theory and new algorithms, *IEEE Transactions on biomedical Engineering*, **58**(2), pp. 355–362.

LOTZE-M., AND HALSBAND-U. (2006). Motor imagery, *Journal of Physiology-paris*, **99**(4-6), pp. 386–395.

LOTZE-M., FLOR-H., GRODD-W., LARBIG-W., AND BIRBAUMER-N. (2001). Phantom movements and pain: an fMRI study in upper limb amputees, *Brain*, **124**(11), pp. 2268–2277.

LU-H., ENG-H.-L., GUAN-C., PLATANIOTIS-K. N., AND VENETSANOPOULOS-A. N. (2010). Regularized common spatial pattern with aggregation for EEG classification in small-sample setting, *IEEE transactions on Biomedical Engineering*, **57**(12), pp. 2936–2946.

MEYER-M. C., VAN OORT-E. S., AND BARTH-M. (2013). Electrophysiological correlation patterns of resting state networks in single subjects: a combined EEG–fMRI study, *Brain topography*, **26**(1), pp. 98–109.

MIJOVIC-B., DE VOS-M., GLIGORIJEVIC-I., TAELMAN-J., AND VAN HUFFEL-S. (2010). Source separation from single-channel recordings by combining empirical-mode decomposition and independent component analysis, *IEEE transactions on biomedical engineering*, **57**(9), pp. 2188–2196.

MORI-H., KATO-R., IKEDA-Y., GOTO-K., TANAKA-S., ASANO-S., SHIKI-Y., NAGASE-T., TAHARA-M., IWANAGA-S ETXXXXX AL.. (2018). The influence of the electrodes spacing of a mapping catheter on the atrial voltage substrate map, *Journal of cardiology*, **72**(5), pp. 434–442.

MORIOKA-H., KANEMURA-A., HIRAYAMA-J.-I., SHIKAUCHI-M., OGAWA-T., IKEDA-S., KAWANABE-M., AND ISHII-S. (2015). Learning a common dictionary for subject-transfer decoding with resting calibration, *NeuroImage*, **111**, pp. 167–178.

MÜLLER-PUTZ-G. R., DALY-I., AND KAISER-V. (2014). Motor imagery-induced EEG patterns in individuals with spinal cord injury and their impact on brain–computer interface accuracy, *Journal of neural engineering*, **11**(3), p. 035011.

NATTEL-S. (2002). New ideas about atrial fibrillation 50 years on, *Nature*, **415**(6868), p. 219.

NGUYEN-D. T., AND TUMOLO-A. Z. (2019). Narrowing the field: Closely spaced bipoles for enhanced detection of low voltage EGM, *JACC: Clinical Electrophysiology*, **5**(1), pp. 78 – 80.

NIAZI-I. K., JIANG-N., JOCHUMSEN-M., NIELSEN-J. F., DREMSTRUP-K., AND FARINA-D. (2013). Detection of movement-related cortical potentials based on subject-independent training, *Medical & biological engineering & computing*, **51**(5), pp. 507–512.

NORTHOFF-G., DUNCAN-N. W., AND HAYES-D. J. (2010). The brain and its resting state activity—experimental and methodological implications, *Progress in neurobiology*, **92**(4), pp. 593–600.

OAKES-R. S., BADGER-T. J., KHOLMOVSKI-E. G., AKOUM-N., BURGON-N. S., FISH-E. N., BLAUER-J. J., RAO-S. N., DIBELLA-E. V., SEGERSON-N. M ETXXXXX AL.. (2009). Detection and quantification of left atrial structural remodeling using delayed enhancement MRI in patients with atrial fibrillation, *Circulation*, **119**(13), p. 1758.

ORSBORN-A. L., MOORMAN-H. G., OVERDUIN-S. A., SHANECHI-M. M., DIMITROV-D. F., AND CARMENA-J. M. (2014). Closed-loop decoder adaptation shapes neural plasticity for skillful neuroprosthetic control, *Neuron*, **82**(6), pp. 1380–1393.

OSTRY-D. J., AND GRIBBLE-P. L. (2016). Sensory plasticity in human motor learning, *Trends in neurosciences*, **39**(2), pp. 114–123.

PAN-S. J., AND YANG-Q. (2010). A survey on transfer learning, *IEEE Transactions on knowledge and data engineering*, **22**(10), pp. 1345–1359.

PERDIKIS-S., TONIN-L., SAEEDI-S., SCHNEIDER-C., AND MILLÁN-J. D. R. (2018). The cybathlon BCI race: successful longitudinal mutual learning with two tetraplegic users, *PLoS biology*, **16**(5), p. e2003787.

RAICHLE-M. E. (2009). A paradigm shift in functional brain imaging, *Journal of Neuroscience*, **29**(41), pp. 12729–12734.

RAICHLE-M. E. (2010). Two views of brain function, *Trends in cognitive sciences*, **14**(4), pp. 180–190.

RAMOSER-H., MULLER-GERKING-J., AND PFURTSCHELLER-G. (2000). Optimal spatial filtering of single trial EEG during imagined hand movement, *IEEE transactions on rehabilitation engineering*, **8**(4), pp. 441–446.

RAMOS-MURGUIALDAY-A., BROETZ-D., REA-M., LÄER-L., YILMAZ-Ö., BRASIL-F. L., LIBERATI-G., CURADO-M. R., GARCIA-COSSIO-E., VYZIOTIS-A ETXXXXX AL.. (2013). Brain–machine interface in chronic stroke rehabilitation: a controlled study, *Annals of neurology*, **74**(1), pp. 100–108.

REICHERT-J. L., KOBER-S. E., NEUPER-C., AND WOOD-G. (2015). Resting-state sensorimotor rhythm (SMR) power predicts the ability to up-regulate SMR in an EEG-instrumental conditioning paradigm, *Clinical Neurophysiology*, **126**(11), pp. 2068–2077.

RICE-D. M. (1990). If realistic neurophysiological constraints are imposed, then maximum statistical entropy is the most probable solution to the EEG inverse problem, *Inverse problems*, **6**(6), p. L55.

RIETA-J. J., AND HORNERO-F. (2007). Comparative study of methods for ventricular activity cancellation in atrial electrograms of atrial fibrillation, *Physiological measurement*, **28**(8), p. 925.

RIETA-J. J., CASTELLS-F., SÁNCHEZ-C., ZARZOSO-V., AND MILLET-J. (2004). Atrial activity extraction for atrial fibrillation analysis using blind source separation, *IEEE Transactions on Biomedical Engineering*, **51**(7), pp. 1176–1186.

RODRÍGUEZ-MAÑERO-M., VALDERRÁBANO-M., BALUJA-A., KREIDIEH-O., MARTÍNEZ-SANDE-J. L., GARCÍA-SEARA-J., SAENEN-J., IGLESIAS-ÁLVAREZ-D., BORIES-W., VILLAMAYOR-BLANCO-L. M ETXXXXX AL.. (2018). Validating left atrial low voltage areas during atrial fibrillation and atrial flutter using multielectrode automated electroanatomic mapping, *JACC: Clinical Electrophysiology*, **4**(12), pp. 1541–1552.

ROLF-S., KIRCHER-S., ARYA-A., EITEL-C., SOMMER-P., RICHTER-S., GASPAR-T., BOLLMANN-A., ALTMANN-D., PIEDRA-C ETXXXXX AL.. (2014). Tailored atrial substrate modification based on low-voltage areas in catheter ablation of atrial fibrillation, *Circulation: Arrhythmia and Electrophysiology*, **7**(5), pp. 825–833.

RUFFINO-C., PAPAXANTHIS-C., AND LEBON-F. (2017). Neural plasticity during motor learning with motor imagery practice: review and perspectives, *Neuroscience*, **341**, pp. 61–78.

SAHA-S., AHMED-K. I., MOSTAFA-R., KHANDOKER-A. H., AND HADJILEONTIADIS-L. (2017a). Enhanced inter-subject brain computer interface with associative sensorimotor oscillations, *Healthcare technology letters*, **4**(1), pp. 39–43.

SAHA-S., AHMED-K. I. U., MOSTAFA-R., HADJILEONTIADIS-L., AND KHANDOKER-A. (2017b). Evidence of variabilities in EEG dynamics during motor imagery-based multiclass brain–computer interface, *IEEE Transactions on Neural Systems and Rehabilitation Engineering*, **26**(2), pp. 371–382.

SAHA-S., HOSSAIN-M., AHMED-K. I. U., MOSTAFA-R., HADJILEONTIADIS-L. J., KHANDOKER-A. H., AND BAUMERT-M. (2019a). Wavelet entropy-based inter-subject associative cortical source localization for sensorimotor BCI, *Frontiers in neuroinformatics*, **13**, p. 47.

SAHA-S., LINZ-D., SANDERS-P., AND BAUMERT-M. (2019b). Beamforming-inspired spatial filtering technique for intracardiac electrograms, *2019 41st Annual International Conference of the IEEE Engineering in Medicine and Biology Society (EMBC)*, pp. 4254–4257.

SAMEK-W., KAWANABE-M., AND MULLER-K.-R. (2014). Divergence-based framework for common spatial patterns algorithms, *IEEE Reviews in Biomedical Engineering*, **7**, pp. 50–72.

SAMEK-W., MEINECKE-F. C., AND MÜLLER-K.-R. (2013). Transferring subspaces between subjects in brain–computer interfacing, *IEEE Transactions on Biomedical Engineering*, **60**(8), pp. 2289–2298.

SANDERS-P., BERENFELD-O., HOCINI-M., JAÏS-P., VAIDYANATHAN-R., HSU-L.-F., GARRIGUE-S., TAKAHASHI-Y., ROTTER-M., SACHER-F ETXXXXX AL.. (2005). Spectral analysis identifies sites of high-frequency activity maintaining atrial fibrillation in humans, *Circulation*, **112**(6), pp. 789–797.

SANDERS-P., MORTON-J. B., DAVIDSON-N. C., SPENCE-S. J., VOHRA-J. K., SPARKS-P. B., AND KALMAN-J. M. (2003). Electrical remodeling of the atria in congestive heart failure: electrophysiological and electroanatomic mapping in humans, *Circulation*, **108**(12), pp. 1461–1468.

SANNELLI-C., VIDAURRE-C., MÜLLER-K.-R., AND BLANKERTZ-B. (2016). Ensembles of adaptive spatial filters increase BCI performance: an online evaluation, *Journal of neural engineering*, **13**(4), p. 046003.

SANNELLI-C., VIDAURRE-C., MÜLLER-K.-R., AND BLANKERTZ-B. (2019). A large scale screening study with a SMR-based BCI: Categorization of BCI users and differences in their SMR activity, *PloS one*, **14**(1), p. e0207351.

SCHREIBER-D., RIEGER-A., MOSER-F., AND KOTTKAMP-H. (2017). Catheter ablation of atrial fibrillation with box isolation of fibrotic areas: Lessons on fibrosis distribution and extent, clinical characteristics, and their impact on long-term outcome, *Journal of cardiovascular electrophysiology*, **28**(9), pp. 971–983.

SEGHIER-M. L., AND PRICE-C. J. (2018). Interpreting and utilising intersubject variability in brain function, *Trends in cognitive sciences*, **22**(6), pp. 517–530.

SELFSLAGH-A., SHOKUR-S., CAMPOS-D. S., DONATI-A. R., ALMEIDA-S., YAMAUTI-S. Y., COELHO-D. B., BOURI-M., AND NICOLELIS-M. A. (2019). Non-invasive, brain-controlled functional electrical stimulation for locomotion rehabilitation in individuals with paraplegia, *Scientific reports*, **9**(1), p. 6782.

SHANNON-C. E. (1948). A mathematical theory of communication, *Bell system technical journal*, **27**(3), pp. 379–423.

SINGH-P., JANA-S., GHOSAL-A., AND MURTHY-A. (2016). Exploration of joint redundancy but not task space variability facilitates supervised motor learning, *Proceedings of the National Academy of Sciences*, **113**(50), pp. 14414–14419.

SMITH-S., DUFF-E., GROVES-A., NICHOLS-T. E., JBABDI-S., WESTLYE-L. T., TAMNES-C. K., ENGVIG-A., WALHOVD-K. B., FJELL-A. M ETXXXXX AL.. (2019). Structural variability in the human brain reflects fine-grained functional architecture at the population level, *Journal of Neuroscience*, **39**(31), pp. 6136–6149.

STILES-M. K., JOHN-B., WONG-C. X., KUKLIK-P., BROOKS-A. G., LAU-D. H., DIMITRI-H., ROBERTS-THOMSON-K. C., WILSON-L., DE SCISCIO-P ETXXXXX AL.. (2009). Paroxysmal lone atrial fibrillation is associated with an abnormal atrial substrate: characterizing the "second factor", *Journal of the American College of Cardiology*, **53**(14), pp. 1182–1191.

SUGIYAMA-M., KRAULEDAT-M., AND MÃŽLLER-K.-R. (2007). Covariate shift adaptation by importance weighted cross validation, *Journal of Machine Learning Research*, **8**(May), pp. 985–1005.

SUK-H.-I., FAZLI-S., MEHNERT-J., MÜLLER-K.-R., AND LEE-S.-W. (2014). Predicting BCI subject performance using probabilistic spatio-temporal filters, *PloS one*, **9**(2), p. e87056.

SVOZIL-D., KVASNICKA-V., AND POSPICHAL-J. (1997). Introduction to multi-layer feed-forward neural networks, *Chemometrics and intelligent laboratory systems*, **39**(1), pp. 43–62.

TADEL-F., BAILLET-S., MOSHER-J. C., PANTAZIS-D., AND LEAHY-R. M. (2011). Brainstorm: a user-friendly application for MEG/EEG analysis, *Computational intelligence and neuroscience*, **2011**, p. 8.

TAKIGAWA-M., RELAN-J., MARTIN-R., KIM-S., KITAMURA-T., FRONTERA-A., CHENITI-G., VLACHOS-K., MASSOULLIÉ-G., MARTIN-C. A ETXXXXX AL.. (2018). Effect of bipolar electrode orientation on local electrogram properties, *Heart rhythm*, **15**(12), pp. 1853–1861.

THANIGAIMANI-S., MCLENNAN-E., LINZ-D., MAHAJAN-R., AGBAEDENG-T. A., LEE-G., KALMAN-J. M., SANDERS-P., AND LAU-D. H. (2017). Progression and reversibility of stretch induced atrial remodeling: characterization and clinical implications, *Progress in biophysics and molecular biology*, **130**, pp. 376–386.

TOMASSINI-V., JBABDI-S., KINCSES-Z. T., BOSNELL-R., DOUAUD-G., POZZILLI-C., MATTHEWS-P. M., AND JOHANSEN-BERG-H. (2011). Structural and functional bases for individual differences in motor learning, *Human brain mapping*, **32**(3), pp. 494–508.

TSAI-A. C., JUNG-T.-P., CHIEN-V. S., SAVOSTYANOV-A. N., AND MAKEIG-S. (2014). Cortical surface alignment in multi-subject spatiotemporal independent EEG source imaging, *NeuroImage*, **87**, pp. 297–310.

TUNG-R., KIM-S., YAGISHITA-D., VASEGHI-M., ENNIS-D. B., OUADAH-S., AJIJOLA-O. A., BRADFIELD-J. S., MAHAPATRA-S., FINN-P ETXXXXX AL.. (2016). Scar voltage threshold determination using ex vivo magnetic resonance imaging integration in a porcine infarct model: influence of interelectrode distances and three-dimensional spatial effects of scar, *Heart Rhythm*, **13**(10), pp. 1993–2002.

ÚBEDA-A., HORTAL-E., IÁÑEZ-E., PEREZ-VIDAL-C., AND AZORÍN-J. M. (2015). Assessing movement factors in upper limb kinematics decoding from EEG signals, *PloS one*, **10**(5), p. e0128456.

VALLENCE-A.-M., GOLDSWORTHY-M. R., HODYL-N. A., SEMMLER-J. G., PITCHER-J. B., AND RIDDING-M. C. (2015). Inter-and intra-subject variability of motor cortex plasticity following continuous theta-burst stimulation, *Neuroscience*, **304**, pp. 266–278.

VAN DE LAAR-B., GÜRKÖK-H., BOS-D. P.-O., POEL-M., AND NIJHOLT-A. (2013). Experiencing BCI control in a popular computer game, *IEEE transactions on computational intelligence and AI in games*, **5**(2), pp. 176–184.

VASILYEV-A., LIBURKINA-S., YAKOVLEV-L., PEREPELKINA-O., AND KAPLAN-A. (2017). Assessing motor imagery in brain-computer interface training: psychological and neurophysiological correlates, *Neuropsychologia*, **97**, pp. 56–65.

VERHEULE-S., ECKSTEIN-J., LINZ-D., MAESEN-B., BIDAR-E., GHARAVIRI-A., AND SCHOTTEN-U. (2014). Role of endo-epicardial dissociation of electrical activity and transmural conduction in the development of persistent atrial fibrillation, *Progress in biophysics and molecular biology*, **115**(2-3), pp. 173–185.

VERMA-A., WAZNI-O. M., MARROUCHE-N. F., MARTIN-D. O., KILICASLAN-F., MINOR-S., SCHWEIKERT-R. A., SALIBA-W., CUMMINGS-J., BURKHARDT-J. D ETXXXXX AL.. (2005). Pre-existent left atrial scarring in patients undergoing pulmonary vein antrum isolation: an independent predictor of procedural failure, *Journal of the American College of Cardiology*, **45**(2), pp. 285–292.

VIDAURRE-C., AND BLANKERTZ-B. (2010). Towards a cure for BCI illiteracy, *Brain topography*, **23**(2), pp. 194–198.

VYAS-S., EVEN-CHEN-N., STAVISKY-S. D., RYU-S. I., NUYUJUKIAN-P., AND SHENOY-K. V. (2018). Neural population dynamics underlying motor learning transfer, *Neuron*, **97**(5), pp. 1177–1186.

WANG-H., CHANG-W., AND ZHANG-C. (2016). Functional brain network and multichannel analysis for the P300-based brain computer interface system of lying detection, *Expert Systems with Applications*, **53**, pp. 117–128.

WANG-W., COLLINGER-J. L., PEREZ-M. A., TYLER-KABARA-E. C., COHEN-L. G., BIRBAUMER-N., BROSE-S. W., SCHWARTZ-A. B., BONINGER-M. L., AND WEBER-D. J. (2010a). Neural interface technology for rehabilitation: exploiting and promoting neuroplasticity, *Physical Medicine and Rehabilitation Clinics*, **21**(1), pp. 157–178.

WANG-W., SUDRE-G. P., XU-Y., KASS-R. E., COLLINGER-J. L., DEGENHART-A. D., BAGIC-A. I., AND WEBER-D. J. (2010b). Decoding and cortical source localization for intended movement direction with MEG, *Journal of neurophysiology*, **104**(5), pp. 2451–2461.

WANG-Y., AND JUNG-T.-P. (2011). A collaborative brain-computer interface for improving human performance, *PloS one*, **6**(5), p. e20422.

WANG-Y., GAO-S., AND GAO-X. (2006). Common spatial pattern method for channel selelction in motor imagery based brain-computer interface, *2005 IEEE Engineering in Medicine and Biology 27th Annual Conference*, IEEE, pp. 5392–5395.

WAYTOWICH-N. R., LAWHERN-V. J., BOHANNON-A. W., BALL-K. R., AND LANCE-B. J. (2016). Spectral transfer learning using information geometry for a user-independent brain-computer interface, *Frontiers in Neuroscience*.

WEI-C.-S., LIN-Y.-P., WANG-Y.-T., LIN-C.-T., AND JUNG-T.-P. (2018). A subject-transfer framework for obviating inter-and intra-subject variability in EEG-based drowsiness detection, *NeuroImage*.

WENS-V., BOURGUIGNON-M., GOLDMAN-S., MARTY-B., DE BEECK-M. O., CLUMECK-C., MARY-A., PEIGNEUX-P., VAN BOGAERT-P., BROOKES-M. J ETXXXXX AL.. (2014). Inter-and intra-subject variability of neuromagnetic resting state networks, *Brain topography*, **27**(5), pp. 620–634.

WOLPAW-J. R., AND MCFARLAND-D. J. (1994). Multichannel EEG-based brain-computer communication, *Electroencephalography and clinical Neurophysiology*, **90**(6), pp. 444–449.

WOLPAW-J. R., MCFARLAND-D. J., NEAT-G. W., AND FORNERIS-C. A. (1991). An EEG-based brain-computer interface for cursor control, *Electroencephalography and clinical neurophysiology*, **78**(3), pp. 252–259.

WONGCHAMPA-P., AND UTHANSAKUL-M. (2017). Orthogonal beamforming for multiuser wireless communications: achieving higher received signal strength and throughput than with conventional beamforming., *IEEE Antennas and Propagation Magazine*, **59**(4), pp. 38–49.

WRONKIEWICZ-M., LARSON-E., AND LEE-A. K. (2015). Leveraging anatomical information to improve transfer learning in brain–computer interfaces, *Journal of neural engineering*, **12**(4), p. 046027.

WU-H. G., MIYAMOTO-Y. R., CASTRO-L. N. G., ÖLVECZKY-B. P., AND SMITH-M. A. (2014). Temporal structure of motor variability is dynamically regulated and predicts motor learning ability, *Nature neuroscience*, **17**(2), p. 312.

ZEROUALI-Y., HERRY-C. L., JEMEL-B., AND LINA-J.-M. (2013). Localization of synchronous cortical neural sources, *IEEE Transactions on Biomedical Engineering*, **60**(3), pp. 770–780.

ZHANG-R., XU-P., CHEN-R., LI-F., GUO-L., LI-P., ZHANG-T., AND YAO-D. (2015a). Predicting inter-session performance of smr-based brain–computer interface using the spectral entropy of resting-state EEG, *Brain topography*, **28**(5), pp. 680–690.

ZHANG-R., YAO-D., VALDÉS-SOSA-P. A., LI-F., LI-P., ZHANG-T., MA-T., LI-Y., AND XU-P. (2015b). Efficient resting-state EEG network facilitates motor imagery performance, *Journal of neural engineering*, **12**(6), p. 066024.

ZHAO-X., CHU-Y., HAN-J., AND ZHANG-Z. (2016). SSVEP-based brain–computer interface controlled functional electrical stimulation system for upper extremity rehabilitation, *IEEE Transactions on Systems, Man, and Cybernetics: Systems*, **46**(7), pp. 947–956.

ZICH-C., DEBENER-S., KRANCZIOCH-C., BLEICHNER-M. G., GUTBERLET-I., AND DE VOS-M. (2015). Real-time EEG feedback during simultaneous EEG–fMRI identifies the cortical signature of motor imagery, *Neuroimage*, **114**, pp. 438–447.